Generation of multi-photon states by climbing the Fock ladder

–Quantum Feedback and Fock-State Generation–

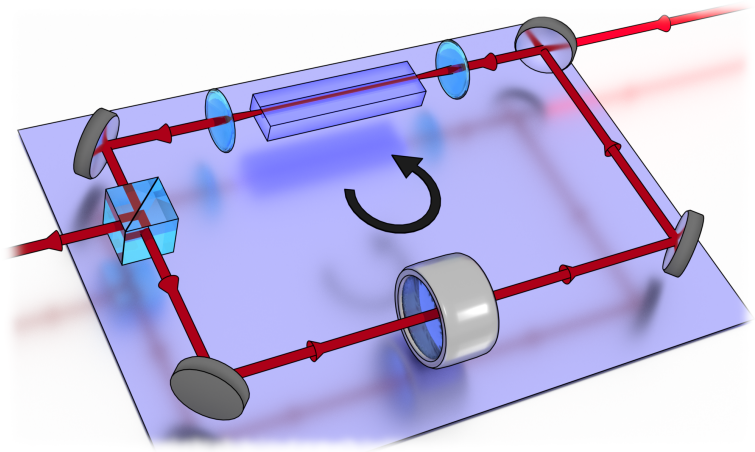

Der Naturwissenschaftlichen Fakultät
der Universität Paderborn
zur
Erlangung des Doktorgrades Dr. rer. nat.
vorgelegt von

Melanie Engelkemeier

aus Paderborn

2021

Contents

Chapter 1

Abstract and Kurzfassung

1.1 Abstract

The generation of complex quantum states become more important in current research, e.g. for the field of quantum information. Fock states are the building blocks for the generation of more complex quantum states such as Holland-Burnett states. One common process for generating Fock states can be found in a parametric down-conversion (PDC) process, which is limited in generation probabilities imposed by the process itself. In this thesis, the experimental realization of a quantum feedback into a special dispersion-engineered PDC source for the generation of Fock states is introduced for mitigating these limitations. Quantum feedback means that we seed the PDC process with a photon previously generated within the process itself. This leads to a ladder-like climbing of the photon number in the feedback mode, leading to the desired Fock state. We introduce this novel scheme by comparing it to the common approach and discuss the improvements achieved by this experimental configuration. In experiment, we could show, for example, up to a 17-fold higher generation probability for a four-photon Fock state compared to the common approach of using a single PDC source without feedback. The effect of quantum feedback is expected to be even stronger the higher the desired photon-number. In addition, we analyze the feedback-mediated long-range quantum correlations up to a distance of the generated photons of three times the repetition rate of our pump.

1.2 Kurzfassung

Die Erzeugung komplexer Quantenzustände wird in der aktuellen Forschung immer wichtiger, z.B. für das Gebiet der Quanteninformation. Fockzustände sind die Bausteine zur Erzeugung von komplexeren Quantenzuständen, wie Holland-Burnett Zustände. Fockzustände werden üblicherweise durch einen parametrischen Abwärtskonvertierungsprozess (PDC) erzeugt, welcher eine Begrenzung in seinen Erzeugungswahrscheinlichkeiten hat. In dieser Arbeit zeigen wir die experimentelle Realisierung einer Quantenrückkopplung in eine spezielle dispersionsentwickelte PDC-Quelle um diese Einschränkungen zu mildern. Quantenrückkopplung bedeutet, dass wir den PDC Prozess mit einem zuvor im Prozess erzeugtem Photon stimulieren. Dies führt zu einem leiterartigen Klettern der Photonenzahl in der Rückkopplungsmode, was zum gewünschten Fock-Zustand führt. Wir zeigen die Neuheit dieses Schemas indem wir es mit dem gängigen Ansatz vergleichen und diskutieren die Verbesserungen durch diese experimentelle Konfiguration. Im Experiment konnten wir z.B. bis zu einer 17-fach höheren Erzeugungswahrscheinlichkeit für einen Vier-Photonen-Fockzustand im Vergleich zum üblichen Ansatz mit einer einzelnen PDC-Quelle zeigen. Wir erwarten, dass dieser Effekt durch die Quantenrückkopplung umso stärker ist, je höher die gewünschte Photonenzahl ist. Zusätzlich konnten wir eine durch die rückkopplungsinduzierte Quantenkorrelation zwischen Photonen mit einem Abstand vom dreifachen der Wiederholungsrate des Pumpmediums zeigen.

Chapter

2 Introduction

Quantum optics, the study of optical phenomena of light and their interaction with matter on the single- and multi-photon level, has become a field of ever growing interest over the past decades. Understanding the behavior of and interactions between photons are central to today's research and are key to their controlled generation and manipulation for upcoming quantum technologies. This especially includes the study of photons, which have been utilized to implement different quantum information processing applications [1–3].

Taking one step back, the long history of the study of photons started in 1901 with Planck's theory of black-body radiation, in which he postulated that this radiation is emitted in discrete energy packets, named quanta [4]. In 1905, Einstein used the theory by Planck to explain the photoelectric effect [5] and was followed by Taylor's interference fringes of single quanta [6], Einstein's radiation fluctuations [7] and Dirac's quantum theory of radiation [8]. Based on these seminal findings, the field of quantum theory matured. The term "photons" with its commonly used symbol γ to describe a quanta of light was introduced by Lewis in 1926 [9] and is derived from the Greek word for light.

One of the earliest experiment in quantum optics was then performed by Hanbury Brown and Twiss in 1954 [10] where they used the correlation of photons from a star that enter two separate telescopes to measure the size of astronomical objects. In 1956, they performed their experiment with a thermal light source, which is split up by a 50:50 beam splitter [11] for showing that the correlation of two optical intensities is expressed by the degree of second-order of coherence. Consequently, in 1963, Glauber introduced the notion of coherent light, which is an essential state of the quantized light field since it describes light with a maximal degree of coherence, and these states are the closest approximation of classical electromagnetic waves [12]. In 1977, Kimble, Dagenais and Mandel performed a pioneering experimental demonstration of the quantization of light by showing a behavior that corresponds to the expected behavior of photon anti-bunching, which is a entirely quantum mechanical effect that only occurs with non-classical light [13, 14].

Sources of photons not only provide insights into fundamental physics of elementary

quantum particles but also satisfy a practical demand in quantum technologies. That is, a photon is a basic carrier of quantum information in many quantum communication protocols [15–17]. Most features and properties become stronger the more photons are in the system or the higher the coherent amplitude of a state is. The fields of quantum metrology, quantum computation and communication rely on the efficient generation of single and multi-photon states [18–20]. Accordingly, the generation of single and multiple photons is one of the most intensively studied topics at present and has attracted the attention of many researchers in the field of physics [21, 22].
The commonly known Fock states are specific single and multi-photon states as they are the energy eigenstates of electromagnetic field modes. Furthermore, Fock states are used for the generation of more complex quantum states, such as Bell states [23, 24], EPR states [25], tensor network states [26–28] and Holland-Burnett states [29, 30].

Different attempts for the generation of single- and multi-photon Fock states have already been established. In general, a ideal single-photon source should emit exactly one photon when triggered by a initial pulse. The most prominent sources for their generation are single emitters, such as atoms and ions [31–34] and quantum dots [35–37], as well as color centers [38] and parametric down-conversion (PDC) [39–41]. Color center are defects in the crystal lattice of a molecule. The optical pumping of these centers lead to the optical transition to a excited level, which emits a photon during its return to the ground state. Thus, the electro-luminescence of these defects under optical pumping emit single photons. In general, the generation of single photons with atoms and ions are performed via excitation of the atom or ion from the ground state to an upper exited state. While the atom relaxes back to the ground state, it emits a cascade of photons and the single photon is selected by filtering. Quantum dots are semiconductor structures in the nanometer regime, and thus, the generation of single photons is performed in a similar way as with atoms and ions. Unfortunately, these sources have a low generation probabilities, and they typically can not generate photons on demand [42]. In general, they produce a photon for each trigger, which is not always collected, meaning these sources are deterministic. There are already first attempts on possibilities using these sources more non-deterministically, but this is still in the process of development.

Within this thesis, we focus on a dispersion-engineered PDC source as presented in Refs. [43, 44]. PDC processes can be used as heralded single-photon sources as they probabilistically generate a photon pair with one photon serving as a herald (i.e., indicator) for the existence of the other photon. This behavior is shown in Refs. [43, 44], as the designed PDC processes in KTP (Potassium titanyl phosphate) have the properties to ensure the usage as a heralded single-photon source. As they are non-deterministic sources, they are more suitable for the generation of single- and multi-photon states compared to the already presented sources. Especially, we will see that because of dispersion engineering of these sources, the optimal process for our experiment can be created.

Firstly, PDC was introduced in 1961 by Louisell, Yariv and Siegman [45] and further investigated by other groups [46–48]. More importantly, Zeldovich and Klychko proposed in 1969 an experiment for the detection of the photon pairs generated within a PDC source [49], which was demonstrated by Burnham and Weinberg in 1970 [39]. PDC

sources form a major source for the generation of single photons and multi-photon states of light [50–54].

Even if the Fock-state generation via PDC sources is one of the most commonly used methods, PDC processes have limitations regarding the generation probabilities of multiple photon pairs that are imposed by the properties of the process itself. PDC processes generate a photon pair with a certain probability, referred to as generation probability in the following. Simultaneously, due to the process itself, further photon pairs are generated with lower generation probabilities. In general, a PDC process has a fundamental limit for the maximal generation probability of one photon pair. Therefore, approaches for increasing generation probabilities for multi-photon Fock states are required, whilst taking the current available components in standard optic labs.

Inspired by a proposal from Paul Kwiat from 2009 [55] in which they showed the reuse of a PDC source several times, and a proposal by Alan Migdall [56] introducing a cavity-based PDC process, we demonstrate one possible way of mitigating the limitations in the generation probabilities of multi-photon Fock states. We perform the Fock state generation via a feedback-based optical network containing a PDC source, which leads to a seeding of the nonlinear process with a recently generated photon because of an overlap of generated photon pairs and subsequent pump pulses. As a result, a coherent addition of photons into a cycling mode is possible, and therefore, we perform a successive build-up of the multi-photon Fock states. Furthermore, by making use of the feedback in the PDC process, we are able to generate long-range quantum correlations between subsequently generated idler photons. Because of the photon-pair correlation of signal and idler, we induce correlations between independently generated idler photons by the feedback. The generation of these long-range correlations is generally difficult to achieve, but they are an important quantum feature needed for quantum-information technology [16, 30].

It is important to mention that these measurements were only possible by a specially designed and engineered PDC source, being decorrelated, single mode and having a high single-photon purity. We showed that this approach renders it possible to generate complex tensor network states [28] and that a theoretical framework can be devised to explain our unique Fock-state generation mechanism [57]. Furthermore, we have submitted the results of the Fock-state generation in Ref. [58].

The theoretical background that pertains to the experimental methodology in this thesis is discussed in Chap. 3. There, we introduce nonlinear optics and the resulting processes from nonlinear materials, the field quantization and the PDC process for generating Fock states. The description of multi-photon Fock states is given by combining the concepts of three-wave-mixing processes in nonlinear materials and field quantization. Moreover, we discuss quantum correlation functions as a tool for characterizing PDC processes. In particular, we show the nonclassical behavior of the Fock state generation, as well as cross-correlations between two or more modes. Furthermore, we give insight into the current state of the art regarding multi-photon Fock-state generation as well as other approaches to increasing generation probabilities of these states and possible

applications of Fock states.

Chapter 4 contains the experimental results of our approach for overcoming the limitations of a PDC process for generating multi-photon Fock states. In the first part, we describe the experimental setup we use, focusing on the properties of the PDC source itself. Within this part, the description of the complete setup is given, where we elaborate on the novelty of our approach. Furthermore, a theoretical framework for the description, simulation and analysis of the Fock state generation is discussed in Sec. 4.2, in which we introduce the formalism regarding the generation, propagation and measurement of states within a feedback-based optical network which contains a nonlinear element and specify this formalism for our setup. Afterwards, we show the first measurement, which investigates the enhancement in the generation probabilities in a easily accessible manner in Sec. 4.3.

The main results of this work, i.e. the generation of multi-photon Fock states and the long-range nonclassical quantum-correlations achieved within the setup between subsequently generated photon pairs, follow in Sec. 4.4 and Sec. 4.5. We further analyze the measured data and compare our approach with the standard generation of Fock states. Within these sections, we will show that our approach generates Fock states up to four photons with a higher probability compared to the standardized approach. Furthermore, we depict the generation of arbitrary photon numbers with this novel approach. Moreover, we were able to show non-classical quantum correlations between generated photons up to a distance of three laser repetition rates between them.

Finally, we conclude the work in Chap. 5 and give an outlook on follow-up projects.

In summary, the main novelty of this thesis is the innovative experimental realization of an advance scheme for quantum state generation and the implementation of an engineered PDC source in a feedback-based system. Moreover, the optimization of the quantum feedback with this nonlinear component is another key finding of this work, shown to improve the Fock state generation. The measurement and direct analysis of photon-number correlations, as well as the characterization of states and feedback correlations given in this thesis show the improvement of already existing methods via the addition of active elements in experimental setups. Finally, we explore the applications of this new setup for quantum information protocols via tensor network states are discussed.

Chapter

3 Fundamentals

Contents

The aim of this thesis is the efficient generation of Fock states within a new approach to using parametric down-conversion (PDC) sources. In general, Fock states are special single- and multi-photon states with a well-defined number of particles n, and they represent the n-th excitation of a field mode. Fock states allow for several applications and serve as a building block for even more complex quantum states. Especially, single- and multi-photon Fock states are the basis for generating, for example, states corresponding to the family of tensor network states, N00N states and Holland Burnett states [26–29]. Quantum photonics can be used to implement applications in all fields of quantum technologies, such as quantum computation and simulation [1, 16], quantum communication protocols [2, 59], quantum metrology [30], and quantum sensing [60]. In contrast to other platforms, photons are the most common way to transmit quantum information [3, 17]. Hence, photons are indispensable for any future quantum network. Consequently, the efficient generation of Fock states are of general interest for several fields of quantum physics.

Within this section, we want to formulate the solid foundation for the description of these states as well as for the generation of them. We have mentioned already that we want to generate these states by making use of a PDC source. For the efficient description of PDC processes, we have to give an introduction to nonlinear optics.

As a brief recapitulation, we will talk about optics in general to classify the field of nonlinear optics. Optics addresses the behavior and the properties of light and its interaction with matter. Some phenomena can be described within a purely classical

framework. There are also some phenomena that can only be described in the quantum mechanical framework. In general, all optical phenomena are describable through quantum mechanics. Planck's theory of black-body radiation [4] and the explanation of the photoelectric effect by Albert Einstein [5] are well-known examples that cannot be explained by classical physics alone. Another example is the effect of photon antibunching [13, 14]. Classical optics can be divided into the fields of geometrical optics and wave optics. Geometrical optics is the simplest but commonly best known, form of describing light as it assumes that light propagates in straight lines, which only bend at optical elements. This approach is sufficient for applications in technical optics, but it does only apply to a small group of physical phenomena. Therefore, a more accurate approach can be found in the classical electromagnetic description of light, wave optics, being described by Maxwell's equations. This description gives insight into the characteristics of light as a electromagnetic wave and therefore also includes wave effects, such as interference, diffraction, polarization and scattering [61–63]. Yet, some optical phenomena cannot be described by the wave formalism since the wave-particle dualism must be considered for quantum light. This optical behavior is described within quantum optics, which investigates the interaction and propagation of light. In general, quantized fields are the central element of quantum optics with photons being the excitations of these fields, defining the notion of the quantum particle of light: the photon. In addition, quantum photonics is mostly focusing on photons. In quantum optics, the application of the quantum mechanical description to optical systems is considered and the interaction of light and matter is described. Furthermore, nonlinear optics, being part of the classical and quantum optics, describes the phenomena that occur while light is propagating through a nonlinear medium [42, 64]. In Sec. 3.1, the classical description for the nonlinear response of a medium, that is the polarization within the medium, is discussed in further detail.

The description of the nonlinear response of the medium through the propagation of light is determined via the electromagnetic fields, as well as the polarization of these fields. We will find that several three-wave mixing processes can appear if the second-order electrical susceptibility of a material is non-zero. One of the processes is the classical counterpart of the PDC process, namely the difference frequency conversion (DFG). Consequently, we have to quantize the fields in order to achieve a description of the PDC process itself. The field quantization is discussed in Sec. 3.1.2 and enables us to give an introduction to Fock states and their characteristics. With the basics we gain from the non-linear optics and the quantization of the fields, we can describe the PDC process and derive the PDC Hamiltonian for the state generation in Sec. 3.1.3.

As mentioned, Fock states are of great interest for several applications. In Sec. 3.2, we will discuss the generation of single- and multi-photon Fock states via a PDC process. In general, within a PDC process, a polarization-entangled photon pair is generated, enabling us to herald the state we want to generate. We will discuss the standard approach for the generation of Fock states with these sources. Unfortunately, a PDC process has a fundamental limit for the maximal generation probability of n photon pairs. In Sec. 3.2.1, we investigate these limitations, which, in principle, is the reason for the necessity

of a more efficient generation of photon pairs. The common approach for the generation of multi-photon Fock states via PDC sources is restricted to this limitations. We want to overcome these limitations with our novel approach. We will give some exemplary works for the generation of Fock states in Sec. 3.2.2, and we also discuss the two works that served as inspiration for our experiment. Moreover, we will discuss the applications of Fock states in greater detail in Sec. 3.2.3, focusing on the generation of Holland-Burnett (HB) states, cat states, W states, cluster states and Greenberger–Horne–Zeilinger (GHZ) state.

Furthermore, we discuss the quantum correlations defining the properties of our system regarding the quantum or classical behavior in Sec. 3.3. We can find the quantum properties of our photon pair generated within the PDC process via two parameters derived from the quantum correlation function defined by Glauber in 1963 [65]. We will introduce a method for calculating nonclassicalities of a generated state as well as cross-correlations between multiple-modes.

3.1 Parametric down-conversion

Parametric down-conversion (PDC) is a three-wave mixing process that occurs due to the nonlinear behavior of a material when light propagates through and interacts with it. This process and its theoretical description has been established over the past decades for generating single- and multi-photon states. Specifically, the PDC process is well-understood for the photon pair generation. As mentioned, we will use these photon pairs generated via the PDC process for the generation of Fock states. In the following, we introduce a classical description for nonlinear processes and furthermore, materials, which are the basis for generating PDC photons. For a more generalized quantum description of these processes, we introduce the quantization of the electromagnetic field and describe the characteristics of Fock states. Especially, we derive the main process of our system, the parametric down-conversion for generating photon pairs, from its classical counterpart via the quantization of the fields.

3.1.1 Nonlinear optics

When a light wave is propagating through a dielectric medium, the electrons or more general charge carriers are displaced from their original position and a polarization of the medium is introduced, leading to internal electric fields. Due to this displacement, a oscillating dipole moment is induced, and consequently, electromagnetic radiation is emitted. The dipole moment per unit volume can be related to the polarization $\tilde{P}$ of the dielectric material. The interference of the emitted electromagnetic fields with the incident light wave leads to the dielectric displacement density

$$\tilde{D}(t) = \varepsilon_0 \tilde{E}(t) + \tilde{P}(t) \tag{3.1}$$

within the matter. $\tilde{E}(t)$ describes the electrical field, $\tilde{P}(t)$ the polarization and ε_0 is the vacuum permittivity. The general description of light in matter is given by Maxwell's

equations, which gives the formalism for the description of light as an electromagnetic wave. In general, the polarization of the medium depends on the field strength of the light wave propagating through the matter. The potential of the charge carriers is, in approximation, harmonic for small displacements, so for applying a weak electric field and small intensities. Hence, for low intensities of the light waves, the polarization increases linearly with the electric field

$$\tilde{P}(t) = \varepsilon_0 \chi^{(1)} \tilde{E}(t), \tag{3.2}$$

where $\chi^{(1)}$ describes the electric susceptibility. Contrary to that, the dipole oscillations are anharmonic for high intensities; this behavior does not longer hold and higher-order contributions become important.

Traveling of light through a nonlinear medium leads then to a nonlinear response of the polarization density $\tilde{P}$ to the electric field $\tilde{E}$ of the light. To show this behavior, the polarization is expanded in terms of the electric field

$$\tilde{P}(t) = \varepsilon_0 \sum_n \chi^{(n)} \tilde{E}^n(t) = \varepsilon_0 \chi^{(1)} \tilde{E}(t) + \varepsilon_0 \sum_{n>1} \chi^{(n)} \tilde{E}^n(t), \tag{3.3}$$

where $\chi^{(n)}$ describes the n-th-order non-linear susceptibility and is an $(n+1)$-rank tensor. We can then divide the polarization into a linear and nonlinear part $\tilde{P}(t) = \tilde{P}^L(t) + \tilde{P}^{NL}(t)$. The rank-three tensor $\chi^{(2)}$ describes the second-order nonlinearity, enabling the kinds of frequency conversion processes we will use within this work [66, 67].

Assuming the simplest case of an initial field, that is a harmonic oscillating field, propagating through a second order nonlinear material with

$$\tilde{E}(t) = E e^{-i\omega t} + c.c., \tag{3.4}$$

with *c.c.* denoting the complex conjugate and ω the frequency of the wave, the second-order polarization turn to

$$\tilde{P}^{(2)}(t) = 2\varepsilon_0 \chi^{(2)} E E^* + \left(\varepsilon_0 \chi^{(2)} E^2 e^{-2i\omega t} + c.c. \right). \tag{3.5}$$

The first term leads to a static electric field in the nonlinear material, known as optical rectification, since the term has no frequency-dependent contribution. Furthermore, the second time derivative vanishes for the first term leading, to no electromagnetic radiation. The nonlinear response of the polarization, as it is given in the second term, leads to an oscillation at twice the frequency of the incident wave. Since the process leads to the second harmonic of the initial field, this three-wave-mixing process is called second harmonic generation (SHG). This process only appears efficiently under the condition that the propagating and generated radiation are phase-matched, otherwise the intensity of the process is not building up. In general, phase matching is a technique to achieve the most efficient nonlinear interaction in the medium by matching the phase between the interacting waves. Thus, phase-matching is needed for a process to occur and for achieving a coherent build up of the second harmonic. A phase matching condition arise from

the momentum conservation within the process, which requires $\vec{k}(\omega) + \vec{k}(\omega) = \vec{k}(2\omega)$. Thus, the phase matching for the given process is fulfilled under the condition

$$\Delta\vec{k} = \vec{k}(2\omega) - 2\vec{k}(\omega) = 0. \tag{3.6}$$

Further information about deriving this phase-matching condition can be found in Ref. [67]. Here, we will only briefly discuss the methods for the phase matching.

In general, the choice of the dielectric medium determines the phase-matched frequency, but there are a few possibilities to engineer this to the desired process. A beam propagating through the given material can either experience the ordinary or the extraordinary index. Thus, these beams are named accordingly, ordinary and extraordinary rays. This technique leads to two different types of processes: the critical and non-critical phase-matching. In the non-critical phase matching, the refractive index is adapted, e.g. by the temperature of the crystal. In contrast, the critical phase matching depends on the crystal orientation. Thus, an angular adjustment of the crystal is needed for achieving a phase matching condition. One can find two different SHG processes: type-0 and type-I. Type-0 phase matching means for the SHG process that both fields, that is the fundamental and the second harmonic field, have the same polarization. Contrary to that, in a type-I process, the two fields have orthogonal polarizations [61, 67, 68]. We would like to mention another frequently used way for achieving phase matching of the interacting beams in the nonlinear material, called quasi-phase-matching. Due to a periodic inversion of the sign of the $\chi^{(2)}$ nonlinearity in the material with a period of Λ, an additional term appears in the phase-matching condition, dependent on the poling period. For example, we can add this additional term to the phase-matching condition of the SFG and DFG, leading to $\vec{k}_{\pm} = \vec{k}_1 \pm \vec{k}_2 \pm \vec{k}_\Lambda$. Thus, one can tune the process to the desired wavelength conversion [61, 67, 68].

We can consider a more general approach, in which the incident field contains of two monochromatic plain waves oscillating at different frequencies,

$$\tilde{E}(t) = E_1 e^{-i\omega_1 t} + E_2 e^{-i\omega_2 t} + c.c., \tag{3.7}$$

which leads to two additional terms in the nonlinear polarization,

$$\begin{aligned}\tilde{P}(t) =& \varepsilon_0\chi^{(2)}\left(E_1^2 e^{-2i\omega_1 t} + E_2^2 e^{-2i\omega_2 t} + 2E_1E_2 e^{-i\omega_+ t} + 2E_1E_2^* e^{-i\omega_- t} + c.c.\right) \\ &+ 2\varepsilon_0\chi^{(2)}\left(E_1E_1^* + E_2E_2^*\right),\end{aligned} \tag{3.8}$$

with $\omega_\pm = \omega_1 \pm \omega_2$. The last term is again leading to no electromagnetic radiation, since there is no time-dependence left. We find, in addition to the two second harmonic terms, one term with the sum and one with the difference of the initial frequencies. The ω_+ term is assigned to a process called sum frequency generation (SFG), and ω_- to a process called difference frequency generation (DFG). Similar to SHG, the coherent build-up of the output wave for SFG and DFG has to fulfil a phase-matching condition (for further information, see Ref. [67]). Usually, the phase-matching condition can only be fulfilled for one process at the same time. Spoken on an photon basis for the SFG process, two

incident photons generate a single photon at the sum of their frequencies whereas for the DFG process, one photon with the difference of their frequencies is generated [67]. We will not further discuss the SFG process here, but we will have a closer look at the DFG process itself since this is the classical counterpart to the parametric down-conversion process we want to introduce.

In Fig. 3.1, the DFG process and the corresponding energy conservation is illustrated. The process contains of one photon being stimulated by a lower energy photon and thus, distributes its energy between a photon at its energy difference (here $\omega_3 = \omega_1 - \omega_2$) and the stimulated photon. We find for the energy conservation that one photon with ω_1 has to be annihilated during the process whereas another one with a lower frequency ω_2 has to be created. Here, we only show the classical nonlinear optics interpretation, in which the DFG process is a seeded process. Thus, the pump field has the highest frequency and the process is seeded with a weak input field, enhancing the conversion of the pump photon. One can find this behavior by solving the coupled-amplitude equations, as done in Ref. [67]. Consequently, without a seed of the process, the amplitudes of the fields do not change.

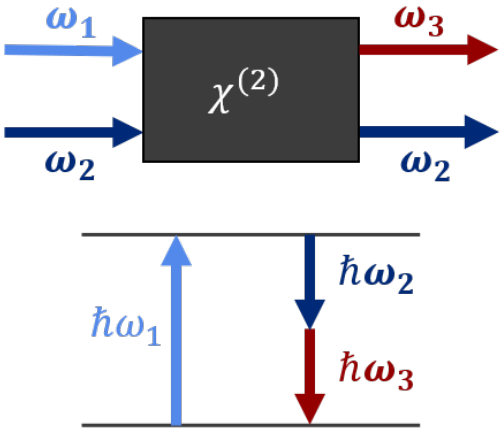

Figure 3.1.: DFG process.

We will find later that a quantum extension of the DFG process exists, called a parametric down-conversion, which is a sort of spontaneous DFG process. Thus, we will introduce the field quantization in the following chapter for introducing the quantum description of light.

Several materials are suited for making use of their nonlinear properties. The discussed nonlinear optical effects occur only in a medium if the second-order susceptibilities $\chi^{(2)}$ do not vanish. Typically, these effects occur in crystals that also exhibit the piezoelectric effect [67]. A few of materials that have been established in the community are BBO (β-barium borate), BiBO (bismuth borate), KDP (potassium dihydrogen phosphate), KTP (potassium titanyl phosphate) and LN (lithium niobate). The first purest decorrelated source with a PDC process at near-infrared wavelengths was demonstrated in bulk KDP [69]. Within our group, we focus on the development and fabrication of periodically poled KTP and LN waveguides for numerous applications in quantum optics (e.g. [43, 70–73]).

3.1.2 Field quantization and Fock states

In this section, we discuss the field quantization and provide a general introduction to Fock states [64]. Fock states are the n-th excitation of a field mode and states with a well-defined number of particles n, according to the excitation. In the following, we will start with a classical description of a harmonic oscillator and then introduce the quantization of the fields to translate to a quantum description.

We consider a one-dimensional cavity with standing waves arising within the cavity, as depicted in Fig. 3.2. A electromagnetic field along the x-axis is then

$$\vec{E}_x(\vec{r},t) = \vec{e}_x \cdot E_x(z,t). \tag{3.9}$$

Using Maxwell's equations,

$$\begin{aligned} \nabla \cdot B &= 0, \\ \nabla \cdot D &= 0, \\ \nabla \times E &= -\frac{\partial B}{\partial t}, \\ \nabla \times H &= \frac{\partial D}{\partial t}, \end{aligned} \tag{3.10}$$

with the magnetizing field H and with the electromagnetic field fulfilling the boundary conditions of $E_x(z=0,t) = 0 = E_x(z=L,t)$, we find

$$E_x(z,t) = \sqrt{\frac{2\omega^2}{V\varepsilon_0}} q(t) \cdot \sin(kz), \tag{3.11}$$

with the optical frequency ω, which is discretized as $\omega_m = m \cdot c\pi/L$, the wave number $k = \omega/c$, the effective cavity length L and the time-dependent generalized position $q(t)$. Consequently, the magnetic field is then given by

$$B_y(z,t) = \left(\frac{\mu_0\varepsilon_0}{k}\right) \sqrt{\frac{2\omega}{V\varepsilon_0}} \dot{q}(t) \cos(kz), \tag{3.12}$$

with the canonical momentum $\dot{q}(t) = p(t)$.

The energy of the field in the medium, commonly known as the Hamiltonian H, is calculated as

$$\begin{aligned} H &= \frac{1}{2} \int dV \left(\varepsilon_0 \vec{E}^2(\vec{r},t) + \frac{1}{\mu_0} \vec{B}^2(\vec{r},t) \right) \\ &= \frac{1}{2}(p^2 + \omega^2 q^2). \end{aligned} \tag{3.13}$$

In this particular case, comparing the first and the second equation above, shows that the electric and magnetic field can be interpreted as the position and momentum, respectively. We only assumed classical fields so far. For the description of the Fock states

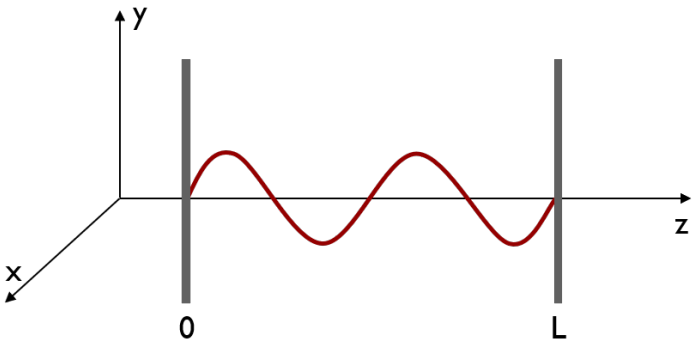

Figure 3.2.: One-dimensional cavity with a standing wave inside. The boundaries are at $z = 0$ and $z = L$

and their generation, we have to quantize the fields. Following the correspondence rule, we replace the canonical position p and momentum q with their operator equivalents, $\hat{p}$ and $\hat{q}$, which fulfill the canonical commutation relation $[\hat{q}, \hat{p}] = i\hbar\hat{\mathbb{1}}$.

For convenience, we introduce the non-Hermitian creation and annihilation operators as

$$\begin{aligned} \hat{a} &= \frac{1}{\sqrt{2\hbar\omega}}(\omega\hat{q} + i\hat{p}), \\ \hat{a}^\dagger &= \frac{1}{\sqrt{2\hbar\omega}}(\omega\hat{q} - i\hat{p}), \end{aligned} \tag{3.14}$$

with $[\hat{a}, \hat{a}^\dagger] = \hat{\mathbb{1}}$. The Hamiltonian can then be written as $\hat{H} = \hbar\omega(\hat{a}^\dagger\hat{a} + 1/2)$ and we can define $|n\rangle$ as an eigenstate of the harmonic oscillator,

$$\hat{H}\,|n\rangle = E_n\,|n\rangle\,, \tag{3.15}$$

with $E_n = \hbar\omega(n + 1/2)$ and the number operator $\hat{n} = \hat{a}^\dagger\hat{a}$. Now, the energy eigenstates can be identified with the photon number n, and furthermore, the minimal occupied state $|0\rangle$ has the lowest energy of $E_0 = \hbar\omega/2 > 0$.

Additionally, we find that $|n\rangle$ is an eigenstate of the number operator $\hat{n}$ with the eigenvalue n. The eigenvalues of the number operator are only non-negative. Moreover, since $\hat{n}$ is Hermitian, the eigenvalues are real numbers. Accordingly, $\hat{a}$ decreases the eigenvalue by one (annihilation operator) and $\hat{a}^\dagger$ increases the eigenvalue by one (creation operator). This leads to the definition of the annihilation and creation operator as a transition between the photon-number or Fock states,

$$\begin{aligned} \hat{a}\,|n\rangle &= \sqrt{n}\,|n-1\rangle\,, \\ \hat{a}^\dagger\,|n\rangle &= \sqrt{n+1}\,|n+1\rangle\,. \end{aligned} \tag{3.16}$$

For the minimal occupied state $|0\rangle$ or vacuum state, $\hat{a}\,|0\rangle = 0$ holds true. Applying the creation operator and normalization give the photon-number or Fock state

$$|n\rangle = \frac{1}{\sqrt{n!}}\left(\hat{a}^\dagger\right)^n|0\rangle \tag{3.17}$$

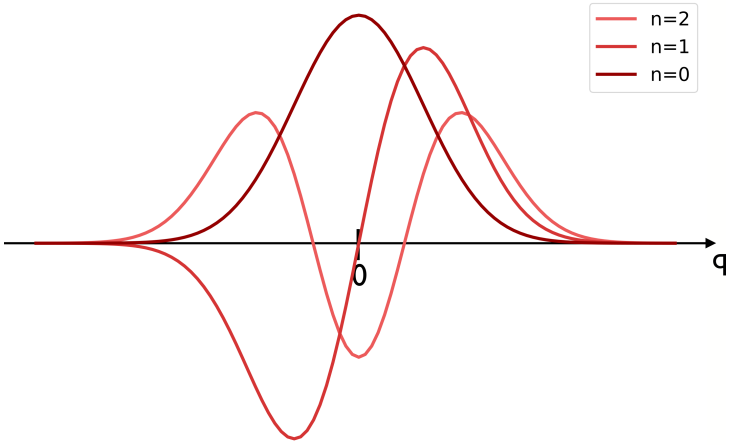

Figure 3.3.: Fock-state representation as a wave function $\psi_n(q)$ up to two photons.

as the eigenstate of the number operator. Since Fock-states are a complete set with $\sum |n\rangle \langle n| = 1$, they serve as a valid basis. Every state can be written as a superposition of number states as

$$|\psi\rangle = \sum_{n=0}^{\infty} c_n |n\rangle . \tag{3.18}$$

Furthermore, we can introduce wave functions for the number state as

$$\psi_n(q) = \langle q|n\rangle , \tag{3.19}$$

with q as the eigenvalue of the quadrature eigenstate $\hat{q}|q\rangle = q|q\rangle$ and the quadrature $\hat{q} = \sqrt{\hbar/2\omega}(\hat{a}^\dagger + \hat{a})$. Thus, the wave function of a Fock-state can be written as

$$\psi_n(q) = \frac{1}{2^n n!}\left(\frac{\omega}{\pi\hbar}\right)^{1/4} e^{-\zeta^2/2} H_n(\zeta), \tag{3.20}$$

with $\zeta = q\sqrt{\omega/\hbar}$ and the Hermite polynomials $H_n(\zeta)$. The shape of the wave functions up to two photons can be found in Fig. 3.3.

In order to allow a more generalized approach to describe states via the Fock-state representation, we describe further states utilizing the density operator description,

$$\hat{\rho} = \sum p_i |\psi_i\rangle \langle\psi_i| , \tag{3.21}$$

with the different quantum states $|\psi_i\rangle$ and their probabilities p_i. For pure states, the trace of the squared density operator is $\mathrm{Tr}(\hat{\rho}_\psi^2) = 1$, and for mixed states, the trace is less than one. More generally, we can define a Fock-state representation in form of

$$\hat{\rho} = \sum_{m=0}^{\infty}\sum_{n=0}^{\infty} c_{m,n} |m\rangle \langle n| . \tag{3.22}$$

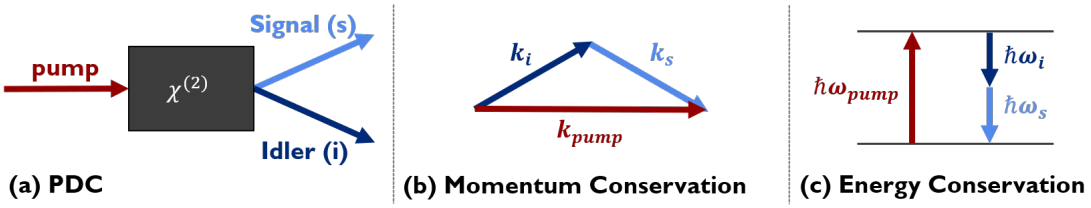

Figure 3.4.: Parametric down-conversion process: A pump photon enters the nonlinear material $\chi^{(2)}$ and decays into two polarization non-degenerate photons, called signal (s) and idler (i). According to momentum (b) and energy conservation (c), the combined momenta and energies of signal ($\vec{k}_s$ and $\hbar\omega_s$) and idler ($\vec{k}_i$ and $\hbar\omega_i$) are equal to the energy and momentum of the pump photon ($\vec{k}_{pump}$ and $\hbar\omega_{pump}$).

3.1.3 Parametric down-conversion Hamiltonian

We start with combining the characteristics of a nonlinear photon-matter interaction and the quantization discussed in the previous chapters so that we can describe the process known-as parametric down-conversion (PDC).

Previously, we have briefly discussed the DFG process, being a seeded process for generating a photon with the difference frequency of two incident photons. Another process can appear in the quantum domain if the amplitude of the seeding wave $\vec{E}_2$ is zero, which is called parametric down conversion (PDC), which is the main process studied within this work. Even if the amplitude of the electric field is zero, the quantum field has non-zero vacuum fluctuations appearing as a seeding mode. Hence, this fluctuations lead to an excitation of the decay of the incident electromagnetic wave with ω_1 into two waves at ω_2 and $\omega_3 = \omega_1 - \omega_2$. This is commonly described as a pump photon decaying into two daughter photons, for historical reasons called signal and idler photon, which is schematically presented in Fig. 3.4(a). Because vacuum fluctuations exist for any frequency ω, this process fulfills the energy and momentum conservation as depicted in Fig. 3.4 (b) and (c). Furthermore, dependent on the intensity of the pump field, not only one photon pair can be generated, but also n-photon pairs can be generated, which leads to a superposition of the photon pairs [67].

We have mentioned already several possible nonlinear materials in which these processes can appear. In this work, we will make use of a dispersion-engineered periodically poled KTP waveguide source, specially designed for an efficient type-II process for the conversion of a photon at 775 nm to signal and idler photons at 1550 nm as it is presented in Refs. [43, 44]. Further details about this source will be given in Sec. 4.1.1. As we have discussed, the type of the process for SHG, type-0 and type-I PDC show the same characteristics for the polarization of the fields. In a type-0 process, the pump photon, signal and idler have the same polarization, whereas in type-I signal and idler have a orthogonal polarization to the pump photon. Thus, in a type-II process, signal and idler have perpendicular polarizations.

For the generation of the previously mentioned Fock states, we have to find the Hamiltonian of the PDC process for generating photon pairs. In general, the unitary operator of a system is defined by its Hamiltonian as $\hat{U} = \exp(-i\hat{H}t/\hbar)$. Since the PDC Hamiltonian is time dependent, we have to derive it differently. We do not write down the complete derivation of the Hamiltonian for the PDC generation here, since it would not be expedient in this context. The complete derivation of the PDC Hamiltonian and its unitary transformation can be found, for example, in Ref. [74]. For the sake of completeness, we restrict ourselves on presenting the unitary operator of the PDC-Hamiltonian $\hat{H}_{\mathrm{PDC}}$ [75] for the state generation $|\Psi_{\mathrm{out}}\rangle = \hat{U}_{\mathrm{PDC}}|\Psi_{\mathrm{in}}\rangle$ within a nonlinear waveguide, given as

$$\begin{aligned}\hat{U}_{\mathrm{PDC}} &= \exp\left[-\frac{i}{\hbar}\int dt \hat{H}_{\mathrm{PDC}}(t)\right] \\ &= \exp\left[-\frac{i}{\hbar}\epsilon\left(\int d\omega_s \int d\omega_i \alpha(\omega_s+\omega_i)\Phi(\omega_s,\omega_i)\hat{a}^\dagger(\omega_s)\hat{a}^\dagger(\omega_i) + h.c.\right)\right],\end{aligned} \tag{3.23}$$

with the pump function α and the phase-matching function Φ, each depending on the frequency ω of signal (s) and idler (i) and with a given constant ϵ denoting the overall efficiency of the process. It could be possible that if many photons decay into photon pairs, these photon pairs recombine into a pump photon. This additional process is called time-ordering effect. Here, we have neglected the effect of time-ordering since it is rather small for a PDC process. Further information about this effects can be found in Refs. [76, 77]. The product of the pump function and the phase-matching function gives us the joint spectral amplitude (JSA) of the generated PDC state, which defines the spectral properties of the produced light.

In general, the resulting photon-number statistics of a PDC process is a convolution of many states, meaning the PDC process is spectrally multi-mode. In the following, we will focus on these spectral properties and analyze this convolution by performing a Schmidt decomposition of the JSA $f(\omega_s,\omega_i)$ [78]. This decomposition is performed by rewriting the JSA into a tensor product of two orthonormal states

$$f(\omega_s,\omega_i) = A\sum_k \lambda_k \phi_k(\omega_s)\psi_k(\omega_i), \tag{3.24}$$

with a constant factor A, the so called Schmidt coefficients λ_k with $\lambda_k \geq \lambda_{k+1}$ and the Schmidt modes defined as $|\phi\rangle_k \otimes |\psi\rangle_k$. The resulting decomposition can be referred to the effective Schmidt number

$$K = \frac{1}{\sum_k \lambda_k^4}. \tag{3.25}$$

This number quantifies the measured spectral correlations between the generated signal and idler photons, where $K = 1$ is equivalent to no correlation. In case of no correlations, a heralding of a photon in the other mode is not possible. Here, B defines a general optical gain defined by the pump intensity, which can be referred to a squeezing parameter per mode, $r_k = B\lambda_k$. Thus, the squeezing value for every mode generated in a PDC process differs from every other mode. Finally, we can rewrite the PDC state as a product of

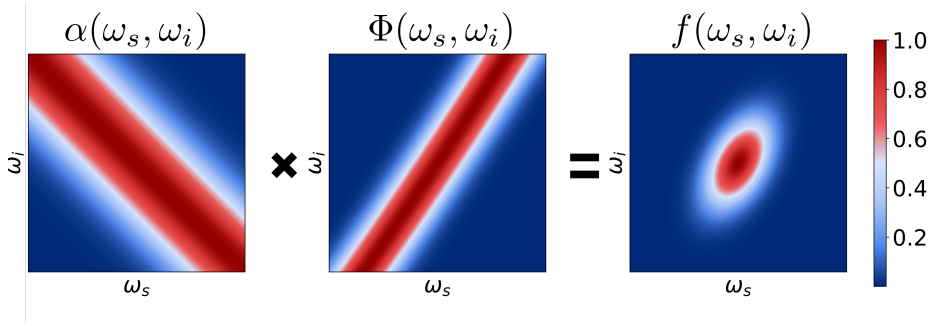

Figure 3.5.: Joint spectral amplitude $f(\omega_s, \omega_i)$ as a product of the Gaussian pump $\alpha(\omega_s, \omega_i)$ and the phase-matching function $\Phi(\omega_s, \omega_i)$.

two-mode squeezers

$$\begin{aligned} |\Psi_{\mathrm{PDC}}\rangle &= \hat{U}_{\mathrm{PDC}} |0,0\rangle \\ &= \bigotimes_k |\Psi_{\mathrm{PDC,two\text{-}mode}}\rangle \,. \end{aligned} \tag{3.26}$$

In Fig. 3.5, a graphic interpretation of the output state, that is the JSA $f(\omega_s, \omega_i)$, is depicted. The exemplified JSA of a state (right plot) is given as the the product of the Gaussian pump $\alpha(\omega_s, \omega_i)$ (left plot) and the phase-matching function $\Phi(\omega_s, \omega_i)$ (center plot). The pump function contains the spectral shape of the pump field and the energy conservation of signal and idler whereas the phase-matching function represents the momentum conservation. Thus, in the resulting state, both energy and momentum conservation are fulfilled. KTP sources show decorrelated states as their phase-matching function is between 0° and 90°, which is a reason for these sources to be chosen for our experiment. We will see these properties of our chosen KTP source in Sec. 4.1.1.

Within the Schmidt decomposition, we found the general description of a PDC state, which we can further write as

$$|\Psi_{\mathrm{PDC}}\rangle = \bigotimes_{k=1}^{\infty} \sqrt{1 - |\lambda_k|^2} \sum n = 0^{\infty} \tanh(r_k)^n \, |n,n\rangle_k \,. \tag{3.27}$$

In this work, we make use of a single-mode PDC source, and thus, we will continue to use the single-mode representation of the process. This step is highly non-trivial and only possible since we have developed a special PDC source in our group as it is described in Refs. [43, 44]. Consequently, we consider only cases with $\tanh(r_k) = 0$ for $k > 1$, and therefore, we discuss the generation of photon pairs via applying the single-mode PDC unitary operator to a two-mode vacuum state $|0_a, 0_b\rangle$ for mode a and mode b. Assuming a type-II PDC source, one photon is generated with vertical and the other one with horizontal polarization. Thus, we can identify the two modes with the two polarizations. Applying the single-mode PDC unitary operator to a two-mode vacuum gives

$$|\Psi_{\mathrm{PDC}}\rangle = \hat{U}_{\mathrm{PDC}} |0,0\rangle = \frac{1}{\cosh(r)} \sum_{n=0}^{\infty} (-1)^n e^{in\theta} (\tanh(r))^n \, |n,n\rangle \,, \tag{3.28}$$

with r as the squeezing parameter containing the amplitude of the optical pump, coupling parameters and interaction times, and with θ as the phase.[1] The resulting state already indicates the pairwise generation of signal and idler photons and furthermore, the two modes exhibit pair- or more general photon-number correlations. The photon-number distribution is given as

$$p_{(n,n)} = |\langle n, n|\zeta\rangle|^2 = \frac{\tanh^{2n}(\zeta)}{\cosh^2(\zeta)}, \tag{3.29}$$

showing that for each independent mode, that is the marginal photon-number distribution, all photon numbers n can be generated. The joint photon-number distribution of both modes will comprise only even components.

In general, for the PDC process itself, i.e. only the generation of one photon pair, we use the Taylor expansion of the PDC unitary which is truncated after the first order. We will see in Sec. 4.2 that we need further terms of the Taylor expansion or more precise the complete single-mode PDC unitary operator for describing the generation of the Fock states in the experiment.

3.2 Fock-state generation via parametric down-conversion

The most common sources for the Fock-state generation are PDC sources. As they provide non-degenerate photon pairs (for historical reasons called signal and idler), they can serve as a heralded photon source [39–41]. We have discussed PDC and the three-wave-mixing processes for the conversion of one pump photon into two daughter photons, as well as the state generation within a PDC process in Sec. 3.1. Here we will introduce the generation of single- and multi-photon Fock states with PDC.

For the Fock-state generation with a PDC source, one needs three steps: the probabilistic generation of photon pairs in a nonlinear material by a pump pulse, the splitting of signal and idler photon with the detection of the idler photon as a herald and further usage of the signal photon. The first step of the probabilistic generation is already described in Sec. 3.1. For instance, the PDC source described within this work is a type-II process, which means that the signal is horizontally polarized and the idler is vertically polarized. Hence, the photon pair is splitted while propagating through a polarizing beam splitter (PBS). After the split-up of the photon pair, the idler is detected with a single-photon detector, which serves as a heralding. Due to the photon-pair or, more general, photon-number correlation between the two photons, the detection of a click in the heralding detector indicates at least one photon in the other arm. For a low gain regime, that is low pump powers, we can make a photon-pair approximation, so the restriction to the first order of the Taylor expansion of the PDC unitary operator. Then we find exactly one photon in the other arm.

The generation of multi-photon Fock states works in a similar way as the single-photon generation with differences only in the heralding detection. Since the aim is to generate

[1] This state is commonly known as two-mode squeezed vacuum state. Typically the PDC unitary operator is referred to the squeezing operator. In the continuous-variable (CV) quantum-optical picture, this is a very important state since it shows Einstein-Podolsky-Rosen correlations between its quadratures. Further information about these states can be found in Refs. [42, 64, 74, 79].

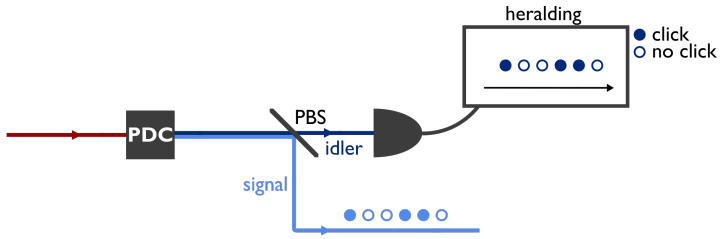

(a) heralded single-photon generation

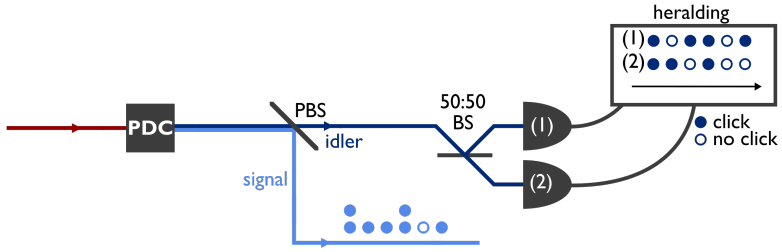

(b) heralded two-photon Fock-state generation

Figure 3.6.: Single- (a) and two-photon (b) Fock-state generation via PDC sources. PBS: polarizing beam splitter; BS: beams splitter; PDC: parametric down-conversion. For further details, see text.

multiple photon pairs at once, detecting n idler photons heralds a n-photon Fock state in the signal mode. Therefore, a photon-number-resolved detection in the heralding is inevitable.

In Fig. 3.6, we show a sketch of the experimental implementation for the single-photon (a) and for the two-photon Fock-state generation (b). In both cases, the PDC source is optically pumped and generates photon pairs, where the single-photon case is shown for the photon-pair approximation described earlier. Single photons are heralded by the detection of the idler photons. The information about one click (filled circle) or no click (blank circle) heralds the existence of a photon in the signal arm. Again, for the heralding of a Fock state with two or even more photons, a photon-number-resolved detection is needed. Here, a quasi-photon-number-resolved detection [80–84] is shown, which makes use of the splitting of the idler beam with a 50 : 50 beam splitter (BS). Due to the splitting, two simultaneously generated idler photons are split up, and a click is detected in both detectors. Therefore, detecting two clicks at the same time, heralds a two-photon Fock state in the signal arm. One has to mention that a splitting only happens in 50% of the cases so that there might be cases of two-pair events that are missed. For the low pump-power regime, we can only be sure that we have generated two photons in the signal arm if we detect a click in each heralding arm. Consequently, for a better resolution for the single- and multi-photon generation, a quasi-photon-number-resolved measurement with splitting of the signal into more detectors is necessary. Hence, for heralding an n-photon Fock state, one needs a resolution of the detector for more than n photons.

The generation of photons with a PDC source exhibits some fundamental limitations given by the probabilistic characteristics of PDC sources, which we discuss in Sec. 3.2.1. Experimental examples for the generation of Fock states via PDC sources, as well as some approaches to overcome limitations in PDC will be discussed in Sec. 3.2.2. Finally, we give a short introduction to possible applications of Fock states in Sec. 3.2.3.

3.2.1 Generation probabilities and limitations

The generation of single- and multi-photon states as mentioned exhibit some limitations regarding the generation probabilities. The first, very naive assumption to obtain reasonable generation probabilities within the fundamental limit is to increase the intensity of the pump pulse since the probability to generate n photons increases with the squeezing parameter, which is proportional to the square root of the pump intensity. Previously, we defined the squeeze parameters r and ζ, both being connected via $\zeta = re^{i\theta}$. But two main problems occur with increasing pump intensities: one has to reach an unreasonable power demands [85] and unwanted higher photon-number components are generated, leading to a reduced fidelity with the target state [86]. One has to mention that the statement of the reduced fidelity is not true for perfect photon-number-resolved heralding, which we typically not have in experiments, however. We further discuss the effects of unwanted higher photon-number components, while analyzing the generation probabilities and state fidelities.

The state generated by the two-mode squeezing is given in Eq. (3.28) and the photon-number distribution (PND) in Eq. (3.29). The PND in general gives the probability of heralding an n-photon Fock state. As we have already discussed, the PDC process shows a fundamental limit of the generation probability depending on the photon number. Thus, from Eq. (3.29), we can calculate the maximum generation probability leading to[2]

$$p_{\max}(n) = \frac{n^n}{(n+1)^{(n+1)}}. \tag{3.31}$$

In Fig. 3.7, the generation probability $p(n)$ (left) dependent on the squeezing parameter $|\zeta|$ and the maximal generation probability for a given photon number $p_{max}(n)$ (right) is shown. First, we see in the generation probabilities that the maximal probability is decreasing with increasing photon number and the required squeezing increases with increasing photon number. The maximal generation probability (right plot) follows a geometric distribution. As mentioned, for a high pumping strength, the photon-pair approximation does not longer apply. Thus, for experimental measurements, one stays

[2] This is done by calculating the partial derivative according to ζ leading to

$$\frac{\partial p_{(n,n)}}{\partial \zeta} = 2\,\mathrm{csch}(2\zeta)\,\mathrm{sech}^2(\zeta)(2n - \cosh(2\zeta) + 1)\tanh^{2n}(\zeta). \tag{3.30}$$

For finding the maximum, one set the derivative equal to zero, yielding the position of the maximum as $\zeta = 1/2\,\mathrm{arccosh}(2n+1)$. Calculating now the generation probability at this position leads to the given maximal generation probability.

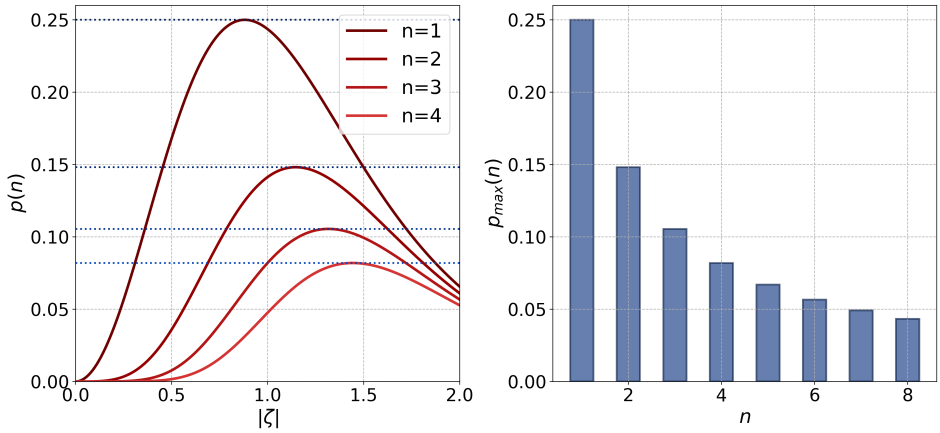

Figure 3.7.: Generation probability for a given photon number n: Dependence of the photon-number distribution $p(n)$ on the squeezing parameter $|\zeta|$ (left) and maximal generation probability $p_{\max}(n)$ (right).

below a value of $|\zeta| = 0.5$. In general, this maximal generation probability is a fundamental limit for generating Fock states.

The analysis of the limitations in the generation probability we show here is already fully described in Refs. [86–88]. First of all, we have to consider detection losses in the heralding arm, where we perform a photon-number-resolved measurement given by operators of the form

$$\begin{aligned}\hat{\Pi}(n) &= \sum_{n=0}^{\infty} c_n \left|n\right\rangle \left\langle n\right| \\ &= \sum_{N=n}^{\infty} \binom{N}{n} (1-\eta)^{N-n} \eta^n \left|n\right\rangle \left\langle n\right|,\end{aligned} \tag{3.32}$$

with the detection efficiency η, the photon number n, the number of detectors N and c_n depends on the used detector. Here, we use a photon-number-resolving detection that leads to $c_n = \binom{N}{n}(1-\eta)^{N-n}\eta^n$. We can then calculate the detection or generation probability for a PDC state given in Eq. (3.28) as a function of the squeezing parameter and the desired photon number n by

$$\begin{aligned}p_n &= \left\langle \psi \right| \hat{\Pi}(n) \left| \psi \right\rangle \\ &= \operatorname{sech}^2(\zeta) \sum_{n=0}^{N} c_n \tanh^{2n}(\zeta).\end{aligned} \tag{3.33}$$

In Fig. 3.8, the dependence of the generation probability for one photon on the detection loss is depicted. Having a closer look into this, one can find that the maximal generation probability is moving to higher squeezing values if you add loss in the detection.

This means the higher the losses within the experiment, the higher the squeezing is needed to achieve the maximal generation probability. The reason for a non-decreasing maximal value can be found in the characteristics of the photons generated within a PDC process as they exhibit thermal statistics. Thus, the state in the signal we analyze here is thermal, and a thermal state remains thermal under loss.

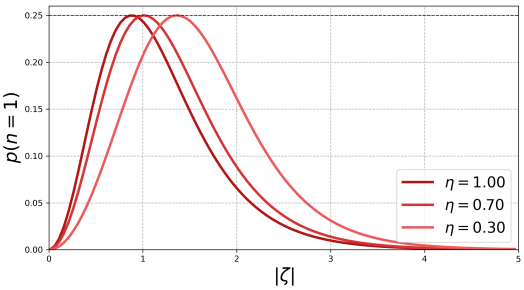

Figure 3.8.: Generation probability dependent on detection loss.

Moreover, one has to consider in parallel to the generation probability also the fidelity of the generated state with the target state. The heralded signal state can be expressed by

$$\begin{aligned}\rho_{\mathrm{s}} &= \frac{\mathrm{Tr_i}(\hat{\Pi}(n)\,|\psi\rangle\,\langle\psi|)}{\langle\psi|\,\hat{\Pi}(n)\,|\psi\rangle} \\ &= \frac{\sum_{n=0}^{\infty} c_n \tanh^{2n}(\zeta)\,|n_{\mathrm{s}}\rangle\,\langle n_{\mathrm{s}}|}{\sum_{n=0}^{\infty} c_n \tanh^{2n}(\zeta)},\end{aligned} \tag{3.34}$$

with the number of photons in the signal mode n_{s}. The fidelity of the heralded state with n photons is defined as

$$\begin{aligned}F(\zeta) &= \langle n|\,\rho_{\mathrm{s}}\,|n\rangle \\ &= \frac{c_n \tanh^2(\zeta)}{\sum_{k=0}^{\infty} c_k \tanh^{2k}(\zeta)}.\end{aligned} \tag{3.35}$$

Thus, the fidelity of a pure single-photon state is then calculated by $F(\zeta) = \langle 1|\,\rho_{\mathrm{s}}\,|1\rangle$. In Fig. 3.9, we show a joint analysis of the fidelity $\mathcal{F}$ and the generation probability $p(n)$ for single photons (left) and two photons (right) with different detection efficiencies η. One can see that the fidelity is decreasing with increasing detection loss and with increasing squeezing values since the higher photon contributions play a bigger role for high squeezing values. For an ideal case of no loss in the heralding detection, the fidelity stays at $\mathcal{F} = 1$. But with decreasing detection efficiency, the the average fidelity decreases. Moreover, the fidelity at maximal generation probability is reduced to $\mathcal{F} = 0.67$ for single photons and $\mathcal{F} = 0.46$ for two photons at a detection efficiency of $\eta = 0.70$ and is reduced even more for lower detection efficiencies. Accordingly, one must find a sweet spot between generation probability and state fidelity. The fundamental limit of $p(n = 1) = 0.25$ for single photons and $p(n = 2) = 0.1482$ for two photons can not be exceeded, even for ideal detection.

In other analysis, it has been already shown that the fundamental limits of the generation probability can only be exceeded by combining multiple PDC sources [89–94].

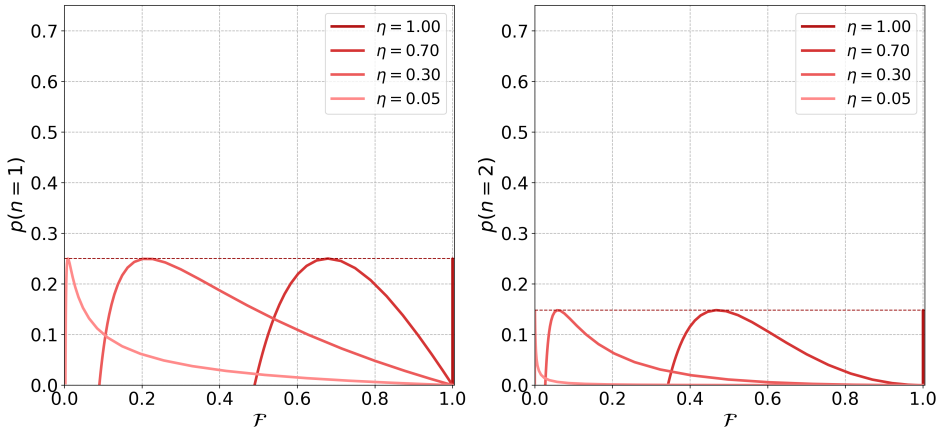

Figure 3.9.: Generation probability versus fidelity for a single photon (left) and a two-photon Fock state (right) generation for different detection efficiencies η. Figure reproduced from Ref. [88].

Source multiplexing can be done by time, space and frequency multiplexing of sources to parallelize the photon-pair generation. Thus, for example, one can use several sources and optically pump them simultaneously to achieve a higher overall generation probability.

In Fig. 3.10 (left), we show the overall areas of generation probability versus state fidelity for three different approaches: binary heralding, with one on-off detector that gives only a click or no click, photon-number-resolved (PNR) detection and with source multiplexing. A binary heralding shows increasing fidelity for decreasing generation probability where the maximum for a lossless case is given by a direct connection of $p(n) = 1 - \mathcal{F}$. The maximal generation probability for the case of the PNR heralding is, as we discussed previously, at $p(n) = 0.25$. A pure deterministic single-photon source would be in the top right, which we can only be obtained with multiplexing. The generation probability of multiplexed PDC sources is calculated via

$$p(n, N) = 1 - (1 - \nu(n))^N, \tag{3.36}$$

for a given number of sources N and with the heralding probability of only one source $\nu(n)$. This behavior is shown in Fig. 3.10 (right) where we see that, with increasing number of PDC sources, the generation probability approaches to $p(n = 1, N) = 1$. This would mean that, for an ideal deterministic single-photon source, one needs a multiplexing of 17 PDC sources to reach a generation probability of $p(n = 1, N) > 0.99$. Having in mind the costs of these sources, as well as the the time-intense alignment of every source, this is a unreasonable number of sources within one optical experiment if one uses spatial multiplexing of these sources. Another attempt could be to integrate several sources into one nonlinear material as it is performed in the field of integrated optics. One would have to split the available pump powers then into 17 parts, leading to unreasonable power demands even for optically pumping these sources with a reasonable power demand in the low gain regime.

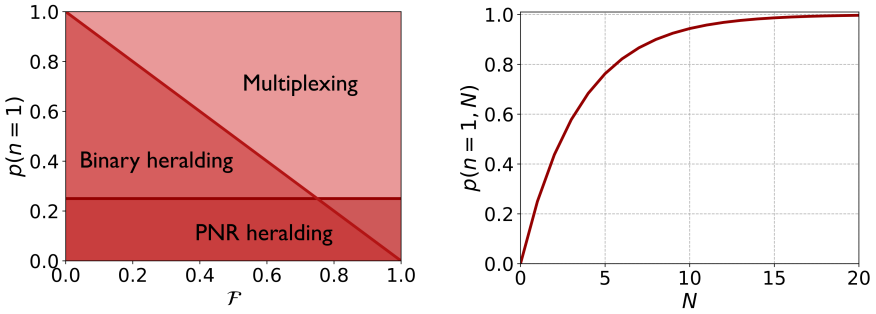

Figure 3.10.: Left: Heralding probabilities versus the state fidelity for binary heralding, photon-number-resolved (PNR) heralding and for multiplexing of the sources. Right: Generation probability for single photons for N multiplexed sources. Figure reproduced from Ref. [88].

Having a look at a two-photon Fock state, more than 28 sources are needed to reach a generation probability above 0.99; for three photons more, than 41 sources are needed. But the amount of pump power one would have to invest to generate a two-photon Fock state (or higher) with high probability is even higher compared to the single-photon case. With adding another photon to the desired state, the number of sources is increasing to an even more unrealistic number of sources for the maximized efficient generation probability, which, in turn, means that one find other solutions for increasing generation probabilities without decreasing the state fidelity. In general, source multiplexing can be easily performed via time-multiplexing. But also in this case, the power demands become unreasonable.

3.2.2 State of the art

Here, we discuss a few already existing experiments for the single- and multi-photon Fock state generation and first approaches for a more efficient state generation. Finally, we will discuss the works which inspired us for our approach to implement a feedback-based PDC source.

First of all, we discuss the approach by Kaoru Sanaka, in which he proposed the extraction of Fock states from coherent states by using only linear optics methods and projection measurements [95]. He uses an coherent state and a single ancillary photon as inputs each for one port of a beam splitter with a reflection probability R, which undergo a unitary transformation into two output modes. There are two possible outcomes, either both the coherent state and the ancillary photon are reflected at the beam splitter or the ancillary photon is transmitted as well as one photon from the coherent state. The coherent state transforms into the desired photon-number state during the propagation trough the beam splitter. For generating an n-photon Fock state, $(n-1)$ beam splitters are needed, where the heralding is performed by detecting a single photon in one arm at each step. He showed a theoretical analysis of a five-photon Fock state resulting from an

initial state with a amplitude $|\alpha| = \sqrt{2}$. He calculates the initial generation probability of five photons as $p_5 = 0.042$ and gives $p_5 = 0.792$ as the final probability with his approach.

This is an interesting method for the more efficient generation of multi-photon Fock states with a very unconventional approach. It would be interesting to see what the fidelity and generation rates might look like in his approach. Still, the amount of required alignment work and material is increasing with the photon number, which is similar to source multiplexing.

Furthermore, we want to present the work by the group of Yoshihisa Yamamoto from Stanford University [52]. They used the fourth harmonic from a Nd:YAG laser source at 266 nm with a repetition rate of 45 KHz to pump a BBO crytal to generate photon pairs at 532 nm. The second harmonic of the laser together with the detection of the signal photon are used as a trigger signal for the detection of the generated state. The signal and idler photons are detected by a visible light photon counter (VLPC), with detection efficiencies of $\eta_1 = 0.68$ and $\eta_2 = 0.58$. They observed up to four photons, where they calculate the fidelity as the probability that n photons are generated. They present fidelities of $F_1 = 1$ and a rate of 11800 Hz for the single photons, $F_2 = 0.94$ and 1100 Hz for the two-photon state, $F_3 = 0.95$ and 160 Hz for the three-photon Fock state and finally $F_4 = 0.60$ and 84 Hz. The given fidelities are already corrected for detection efficiencies. It is worth pointing out that they claim their fidelities as probability of the generation. Another approach could be to show the similarity of the experimental achieved state to the target state. Having a look at the rates, one can say that they are already quite impressive values for this work.

As a third work, we want to discuss the implementation by the group of Brian J. Smith at the University of Oxford [53] in which they demonstrate the generation of Fock states up to three photons. They start with a titanium sapphire (Ti:Sa) laser at 830 nm with a repetition rate of 80 MHz, pumping a BBO crystal and generating pulses at 415 nm via SHG. These generated pulses optically pump a potassium dihydrogen phosphate (KDP) crystal for performing PDC and generating photon pairs. These photon pairs were split up at a polarizing beam splitter (PBS) and the horizontally polarized light is detected via spatially multiplexed detector with a cascade of two $50:50$ beam splitter (BS) and three avalanche photodiodes (APDs). This detection serves as a herald for the generated state, where the detection of $n \in \{1, 2, 3\}$ clicks herald an n-photon Fock state. The state is then characterized via balanced homodyne detection (HD) with a small fraction of the laser pulses serving as local oscillator (LO). The rate they achieve for the single photon generation is 180 kHz, whereas it drops to 200 Hz for the two-photon Fock state and 1 Hz for the three-photon Fock state. Unfortunately, they only mention a fidelity for the three-photon Fock state of about 99.7% but give no fidelity for the other generated states. The fidelity is here calculated between the predicted and reconstructed three-photon state. Comparing the rates with the previous presented work, one can see that this implementation exhibits an improvement in the rates by a factor of more than 15 between the two approaches.

The last work we want to discuss is the implementation by the group of Rosa Tualle-Brouri at the University Paris-Saclay for the one- and two-photon Fock state generation given in Ref. [54]. Their setup is divided into three parts: SHG, PDC in an optical parametric amplification (OPO) configuration and a quantum state tomography via HD. A titanium sapphire laser with a repetition rate of 76 MHz at a central wavelength of 850 nm is optically pumps a type-I BBO crystal for performing SHG with output pulses at 425 nm. Here, the conversion efficiency is increased by a cavity around the source matching, the repetition rate of the laser. The generated pulses at 425 nm optically pump again a type-I BBO crystal for performing a PDC process, and the OPO configuration enhances the peak power of the generated pulses. Finally, the pulses are differently used after the PDC process. One pulse is sent to two single-photon counting modules, separated by a 50 : 50 beam splitter for heralding a one- or two-photon Fock state, whereas the heralded state is then characterized by quantum state tomography using a HD. Hence, parts of the laser pulses with a reduced repetition rate–the reduction is performed by a Pockels cell–are used as local oscillator for the HD. The overall efficiency of their setup is 6% and the detection efficiency of the HD is $(76 \pm 6)\%$. It is worth mentioning that all given fidelities are corrected for these detection losses. The generated single-photon Fock states have a fidelity of $88^{+4}_{-3}\%$ at a generation rate of 250 kHz, and the two-photon Fock states have a fidelity of $(82 \pm 6)\%$ with a generation rate of 800 Hz.

They also showed an improvement of the setup by adding a optical delay line and triggering the Pockels cell with the photon heralding events, which could increase the repetition rate of the LO needed for the HD since it was reduced to 1 MHz in order not to saturate the HD. With these improvements, they observed higher fidelities but slightly lower generation rates within their setup. Thy observe a fidelity of $(91 \pm 4)\%$ and a generation rate of 200 kHz for the single-photon Fock state and $(88 \pm 4)\%$ and again a lower generation rate of 250 Hz for the two-photon Fock state.

The most interesting point of this work is the OPO configuration around the PDC source, which is similar to our approach, and therefore, the reason for presenting their work in this context. Comparing these rates with the previously presented paper, we see that the rates for the single-photon generation are slightly lower, but the ones for the two-photon Fock states are four times higher.

Further experimental and theoretical works, which we do not discuss in this framework in detail, but which are worth to mention, are:

- The ultra-fast generation of heralded single photons by the group of Sébastien Tanzilli, where they generate single photons with a heralding rate of 2.1 MHz [96].
- A work from our own group, where the authors show the efficient preparation of high-fidelity single-photon states via fiber-optic quantum networks [70]. They achieved a heralding rate up to 105 kHz.
- The work from the group of Massimiliano F. Sacchi on an optical device for synthesizing Fock states via a coherent source [97].

- The group of Katherine B. Whaley showed a scheme for the deterministic generation of n-photon Fock states from atoms in an optical cavity [98].
- Several other interesting works on Fock-state generation can be found in Refs. [94, 99–104]

So far, we only showed general methods for generating single- and multi-photon Fock states, but we also want to discuss approaches for overcoming the fundamental limitations in their generation probabilities.

There are three main works we will present in this context since they were part of our inspiration for an approach to generate Fock states more efficiently: making use of large-scale time multiplexing for the highly efficient single-photon generation [93], recycling of the PDC sources several times for efficient optical state engineering [55] and employing a cavity-based PDC process with ancillary photon-number measurement [56].

We start with an experimental implementation of source multiplexing, carried out by the group of Paul Kwiat [93]. We have briefly discussed multiplexing of PDC sources on a theoretical basis in Sec. 3.2.1, and the increase of generation probabilities regarding n photons. In their experimental implementation, they demonstrate a multiplexed PDC source for the generation of single photons. Here, they use a combination of a laser with a repetition rate τ and an SHG process to pump a periodically poled KTP PDC source for generating photon pairs.

The signal photon is stored in an adjustable delay line, where the detection of the idler photon triggers the delay. The effect they use is that because of the storing of the photon, the conversion of any initial time-bin state of the heralded photon into a fixed output time-bin. With this method, they showed an enhancement by a factor of 9.7 in generation efficiency. Here, the group considers a pump pulse train as multiplexing of the source. In general, the result regarding an enhancement in generation efficiencies in single-photon generation is impressive as they get $p(n) \approx 0.6$, being larger than the fundamental limit of $p(n) = 0.25$ in a single PDC process.

Furthermore, we want to discuss two very similar theoretical proposals by the groups of Paul Kwiat [55] and Alan Migdall [56]. In their theoretical proposals, they discuss the effects of using a PDC source several times to pseudo-deterministically add photons to a mode. Both use a laser source to optically pump a PDC source, where one mode is stored in a cavity, matching the repetition rates of their laser, and the other mode is used as herald. The stored mode is then amplified in the cavity by the subsequent pump pulse, where the desired photon number is indicated by the heralding, and after reaching this photon number, the state in the cavity is released. The group of Alan Migdall demonstrates with their simulations that they could achieve an enhancement of the generation probability by a factor of four to ten for their desired four- to twelve-photon Fock states.

Even if both are only theoretical proposals, the idea and the enhancements are very impressive. Therefore, an experimental implementation of this proposal will be of great interest.

Consequently, this theoretical approaches have led us to our experimental implementation of a PDC source utilization that adapts the cavity-based approach to enhancing generation probabilities. Later, we will see the exact implementation of the feedback into the source, being more like a time-multiplexing instead of a mirror-based cavity as put forward in both proposals.

3.2.3 Fock-state applications

Single photons and multi-photon Fock states are of broad interest in the community, especially, since they allow for several applications. Single photons and multi-photon Fock states are the building blocks for more complex quantum states, being used in many different fields of quantum physics. One very important field to be mentioned here is the field of quantum information [1–3], with its subfields quantum computation [105, 106] and quantum communication [16, 17, 59]. Furthermore, they are also very important from the perspective of fundamental physics [2].

In the field of optical quantum computing, for example, the photon is the most interesting physical particle for the usage as a quantum bit (qubit). The main requirements of qubits is that they can be prepared in a distinct initial state, can reliably encode quantum information, can interact for applying quantum gates and can be measured. A photon fulfills all these requirements and is, therefore, an excellent choice as a qubit, and the encoding of the two values of a bit can be performed in several ways, whose most prominent ones are the encoding in polarization and the path degree of freedom [105–107].

In the following, we will discuss four types of states and the generation of those based on Fock states: Holland-Burnett states, Schrödinger cat states, W states and two examples of tensor-network states. We will see that each state corresponds to a relevant application in one of the previously mentioned fields of quantum physics.

Holland-Burnett (HB) states are the experimental approximation of NOON states $|\psi\rangle = \frac{1}{\sqrt{2}}(|N,0\rangle + |0,N\rangle)$, which are experimentally hard to generate. As NOON states are a important tool for improving phase-sensing measurements, HB states find their application in this field as well [29, 108]. Furthermore, phase sensing is a useful tool for quantum metrology [30, 109] and error correction [110]. HB states are generated via n photon pairs, generated in PDC processes, utilizing only one photon component of the overall state as it is given in Eq. (3.28). The initial state in the form of $|N/2, N/2\rangle$ is passed through a beam splitter, introducing a phase shift ϕ. The resulting state is in the form of

$$|\psi\rangle = \sum_{n=0}^{N/2} \frac{\sqrt{(2n)!(N-2n)!}}{2^{N/2} n!(N/2-n)!} e^{2in\phi} |2n, N-2n\rangle \,. \tag{3.37}$$

There are already several experiments showing the generation of HB states with two, four and six photons [108, 111–114].

A cat state, named by the famous gedankenexperiment by Schrödinger [115], is a superposition of two coherent states with opposite phases as

$$|\psi\rangle = A \cdot \left(|\alpha\rangle + e^{i\theta}\,|-\alpha\rangle\right), \tag{3.38}$$

with a given constant $A = \left[2\left(1+\cos(\theta)e^{-2|\alpha|^2}\right)\right]^{-1/2}$. These states find applications in fundamental quantum theory, quantum computation, quantum information and quantum teleportation [3, 116–119]. Furthermore, the generation of cat states is performed by n photon pairs simultaneously generated via PDCs or OPAs (optical parametric amplifier). The Fock states are propagating through a beam splitter and cat states are generated [120, 121].

The two aforementioned states are two state superpositions. W states are a three-state superposition and defined as

$$|\mathrm{W}\rangle = \frac{1}{\sqrt{3}}\left(|1,0,0\rangle + |0,1,0\rangle + |0,0,1\rangle\right), \tag{3.39}$$

and due to the form of the state, they represent a form of tripartite entanglement, which is important for quantum information theory. Generalizing this kind of state for N modes, so a superposition in form of

$$|W\rangle = \frac{1}{\sqrt{n}}\left(|1,0,0,\ldots,0\rangle + |0,1,0,\ldots,0\rangle + \cdots + |0,\ldots,0,0,1\rangle\right) \tag{3.40}$$

enables multi-partite entanglement [122]. W states are, for example, used for quantum-secure communication in form of quantum key distribution [123, 124]. Furthermore, they find application as states for the optimal universal quantum cloning machine [125–127]. W states can be generated via PDC sources, where n-photon Fock states are traveling through beam splitter cascades such that in each output port only one photon is left [128].

Furthermore, one can use Fock states for the generation of several states belonging to the group of tensor-network states (TNS). In general, TNS enable complex quantum correlations, which, in turn, means they provide multi-partite entanglement. Their wave function describes a network of interconnected tensors that captures the relevant entanglement properties. One of the most important states in the family of TNSs are matrix product states (MPSs), describing one dimensional systems, such as Greenberger–Horne–Zeilinger (GHZ) state and cluster states. Moreover, a tensor-product state describes multidimensional systems, and a multiscale entanglement renormalization ansatz describes any-d scale invariant system since they are the ground state of certain many-body models [129, 130].

As an example, a four-photon polarization-entangled cluster state is defined as

$$\begin{aligned}|\mathrm{Cluster}\rangle =& \frac{1}{2}(|H\rangle_1|H\rangle_2|H\rangle_3|H\rangle_4 + |H\rangle_1|H\rangle_2|V\rangle_3|V\rangle_4 \\ &+ |V\rangle_1|V\rangle_2|H\rangle_3|H\rangle_4 - |V\rangle_1|V\rangle_2|V\rangle_3|V\rangle_4).\end{aligned} \tag{3.41}$$

One can generate this states as it is shown in the theoretical proposal in Ref. [27]. They propose to have two single-photon states, generated via type-I PDC process, and one two-photon polarization-entangled state, generated via type-II PDC process, as input modes for their experimental setup. Thus, the input state consists of various Fock states, leading to an input state $\frac{1}{\sqrt{2}}(|H\rangle_a |H\rangle_2 + |V\rangle_1 |V\rangle_2) |H\rangle_3 |H\rangle_4$. Three modes are then transformed via a half-wave-plate into diagonal and anti-diagonal polarization for the initial horizontal and vertical polarizations, respectively. Afterwards, the resulting modes one and three, as well as modes two and four, are mixed at a polarizing beam splitter. Finally, all four modes are detected and by post selecting on a four-photon coincidence in the detection, they achieve the desired cluster state. They mainly require single-photon Fock states and two-photon polarization-entangled states.

Another quite prominent example of a TNS is the GHZ state. They are defined as

$$|\mathrm{GHZ}\rangle = \frac{1}{\sqrt{2}} \left(|0,0,0,0,\ldots\rangle + |1,1,1,1,\ldots\rangle\right). \tag{3.42}$$

We can find one approach for generating these states in a theoretical proposal given in Ref. [131] where the author shows the generation of a three-photon GHZ state. He proposes to generate in total four photons via two non-linear processes, which can be refereed, for example, to a type-II PDC process. Three of these photons, namely one at a given polarization (say V for the sake of exposition) and two at the orthogonal polarization (H), are used as input for the main experimental configuration. The first two photons are send through a beam splitter and one of the resulting photons is rotated by a wave-plate, leading to a swapping of the polarizations from $|V\rangle \rightarrow -|H\rangle$ and $|H\rangle \rightarrow |V\rangle$. The third photon is rotated via a wave-plate, as well before mixing with the other resulting photon at a polarizing beam splitter. All resulting photons are then detected and because of post-selecting on a three-photon coincidence they achieve the three-mode GHZ state. One can see that this approach for the generation GHZ state is quite similar to the previous shown generation of a cluster state.

Furthermore, we proposed the generation of W states and GHZ states within our approach, discussed in Ref. [28]. Further information about this proposal can be found in Appendix B.

In general, the quantitative and qualitative efficient generation of multi-photon Fock states is essential for generating all aforementioned states and allow for the application of those states in various protocols.

3.3 Quantum correlations

In this section, we want to discuss quantum correlations that describe the properties of the generated states and more general the properties of light. We won't describe classical correlations here, but one can find a description of the first- and second- order classical correlations in Appendix C. According to these classical correlations, in 1963, Roy Glauber defined quantum correlation functions for describing quantum light [65]. While

it is not our intent to present the full derivation of said functions here, we are still going to provide the most general form of such quantum correlations. The full derivation can be found in Ref. [132].

In general, the cross-correlation functions of two modes are derived via the electric field operators. We can give the correlation function in a dependence of the creation and annihilation operators. Thus, they are given in form of

$$g^{(n,m)}(t_1^{(a)},\dots,t_n^{(a)},t_1^{(b)},\dots,t_m^{(b)}) = \frac{\left\langle \hat{a}^\dagger(t_1^{(a)})\dots\hat{a}^\dagger(t_n^{(a)})\hat{a}(t_1^{(a)})\dots\hat{a}(t_n^{(a)})\hat{b}(t_1^{(b)})\dots\hat{b}^\dagger(t_m^{(b)})\hat{b}^\dagger(t_1^{(b)})\dots\hat{b}(t_m^{(b)})\right\rangle}{\left\langle \hat{a}^\dagger(t_1^{(a)})\hat{a}(t_1^{(a)})\right\rangle\dots\left\langle \hat{a}^\dagger(t_n^{(a)})\hat{a}(t_n^{(a)})\right\rangle\left\langle \hat{b}^\dagger(t_1^{(b)})\hat{b}(t_1^{(b)})\right\rangle\dots\left\langle \hat{b}^\dagger(t_m^{(b)})\hat{b}(t_m^{(b)})\right\rangle} \tag{3.43}$$

with $\hat{a}^\dagger$ and $\hat{b}^\dagger$ describing the creation operator for the two modes a and b. Thus, $\hat{a}$ and $\hat{b}$ describe the corresponding annihilation operators. For a PDC process the associated modes represent the signal and idler fields. For the states we generate, we are only looking at a vanishing time difference between both modes of $\tau = t_1 - t_2$. We can find two values from this equation, namely $g^{(2)}$ (so the reduction to one mode) and $g^{(1,1)}$, being relevant for the characterization of the state generated within a PDC process. The correlation function $g^{(1,1)}$ can be interpreted as the probability of measuring one photon in one mode conditioned on the probability of measuring one photon in the other mode. The $g^{(2)}$ value then gives the probability of measuring two photons in one mode, normalized to the square of the probability of measuring one photon in that mode. Thus, it can be interpreted as the conditional probability that if we detect a photon at time t_1, there is another one detected at $t_2 = t_1 + \tau$. The value of the measured $g^{(2)}$ can give us information about the states behavior, meaning a separation of states with and states without a classical analog. In general, the transition between classical and quantum light can be found at a value of $g^{(2)} = 1$, where a lower value corresponds to quantum light. For example, coherent states, as introduced by Schroedinger in 1926 [133], have a classical analog as a perfect classically coherent wave, resulting in $g^{(2)} = 1$. Glauber has introduced them in a context of quantum light [12] and thus, they describe quantum light with a maximal degree of coherence. In contrast, states with $g^{(2)} < 1$ have no analog in the classical wave theory of light, thus being referred to as nonclassical states. It is noteworthy that, the inverse $g^{(2)} \geq 1$ does not imply classical light. States with $g^{(2)} < 1$ show photon-number distributions with a variance being smaller as the variance of a Poissonian photon-number distributions. This can not be achieved with classical light. Accordingly, the measurements of these values give us information about the quantum properties of our photon-pair generation with a PDC source. Moreover, the $g^{(2)}$ value gives us insight into the photon statistics, e.g. a thermal photon statistics results in $g^{(2)} = 2$. The marginal photon-number distribution of the state generated within a PDC process is thermal, thus leading to $g^{(2)} = 2$ [134]. Furthermore, the achieved $g^{(2)}$ value allows for a statement about whether the state is single mode [87]. In some approximation, we can find a connection between the Schmidt number or the effective mode number K as $g^{(2)} \approx 1 + 1/K$ following from the previous shown Schmidt decomposition.

Thus, a value of $g^{(2)} = 2$ leads to a effective mode number of $K = 1$, saying that the state is single-mode.

In our experiments, we want to generate Fock states with higher photon numbers. Thus, we are able to measure correlation functions with a higher photon number within the generated states, which can be derived from the click-counting statistics we will focus on in the following.

We can generalize the quantum correlation functions of a state as introduced previously by expanding the detection of these states to higher photon numbers. Previously, we have shown $g^{(2)}$ as a parameter that gives us information about the quantum behavior of light. The quantum correlations within a state measured with a multiplexed detection scheme gives us further insights into the nonclassical properties of the state. Again, a $g^{(n)}$ relates the probability on detecting n photons, normalized on n times the detection of one photon. Standard approaches for analyzing the quantum correlations refer to the photon-number statistics whereas only click statistics are achievable in today's quantum optics labs. The calculation of the photon number statistics from the click statistics is a hard task and usually it is prone to errors. Consequently, we want to motivate the usage of click-counting statistics.

Typically, the photoelectric detection of quantum light can be described by a quantum version of the Poisson distribution in form of

$$p_n = \left\langle : \frac{\eta \hat{n}^k}{n!} \exp\left(-\eta \hat{n}\right) : \right\rangle \tag{3.44}$$

with the detection efficiency η and $: \cdots :$ denoting normal ordering. The Mandel Parameter [135], defined as

$$Q_M = \frac{\langle (\Delta n)^2 \rangle}{\langle n \rangle} - 1, \tag{3.45}$$

measures the deviation of the photon number distribution from Poisson statistics according to the mean value $\langle n \rangle$ and the variance $\langle (\Delta n)^2 \rangle$. However, common detection system give the information of detecting at most a click or no click. We can expand this information via using a multiplexed detection scheme. Generally, a multiplexing detection scheme means that the signal is split by several 50:50 BS into many bins (spatial or time bins), where each bin is then detected separately, which gives a quasi-photon-number-resolved detection [80, 81]. The click-counting distribution of states detected with these systems rather follow a binomial statistics, given as

$$c_k = \left\langle : \binom{N}{k} \left(\exp\left(\frac{-\eta \hat{n}}{N}\right)\right)^{N-k} \left(\hat{1} - \exp\left(\frac{-\eta \hat{n}}{N}\right)\right)^{k} : \right\rangle, \tag{3.46}$$

than a Poisson statistics [136]. The number of detectors in the multiplexed scheme is denoted by N and the binomial coefficient is defined as $\binom{N}{k} = \frac{N!}{k!(N-k)!}$. Similarly to the Mandel parameter, we can define

$$Q_B = N \frac{\langle (\Delta c)^2 \rangle}{\langle c \rangle \left(N - \langle c \rangle\right)} - 1 \tag{3.47}$$

with the corresponding mean value and variance of the given click-counting statistics. If this value is negative, we find that the state has nonclassical properties. Consequently, the click-counting statistics are truly measurable in laboratories, including ours. Thus, we will use the click-counting statistics for analyzing quantum correlations [82–84].

In the following, we will introduce the methods for analyzing the nonclassical behavior of the generated states. This method is introduced in Ref. [84] and uses the matrix of nonclassical moments of the click counting statistics for the calculation of the nonclassical behavior of a state. The click-counting statistics are given according to Eq. (3.46). For any classical light field, the matrix of click moments is positive semi-definite with $0 \leq M$. Hence, a violation of this relation shows nonclassical quantum correlations. The matrix of moments is defined as

$$M = \begin{pmatrix} 1 & \langle{:}\hat{\pi}{:}\rangle & \langle{:}\hat{\pi}^2{:}\rangle & \dots & \langle{:}\hat{\pi}^N{:}\rangle \\ \langle{:}\hat{\pi}{:}\rangle & \langle{:}\hat{\pi}^2{:}\rangle & \ddots & \ddots & \vdots \\ \langle{:}\hat{\pi}^2{:}\rangle & \ddots & \langle{:}\hat{\pi}^4{:}\rangle & \ddots & \vdots \\ \vdots & \ddots & \ddots & \ddots & \vdots \\ \langle{:}\hat{\pi}^N{:}\rangle & \dots & \dots & \dots & \langle{:}\hat{\pi}^{2N}{:}\rangle \end{pmatrix}, \tag{3.48}$$

where $\langle{:}\,\hat{\pi}^l\,{:}\rangle$ denotes the l-th factorial moment of the click-counting statistics, which can be calculated via

$$\langle{:}\,\hat{\pi}^l\,{:}\rangle = \sum_{k=0}^{N} \frac{\binom{k}{l}}{\binom{N}{k}} c_k. \tag{3.49}$$

Thus, they are directly derived from the measured click statistics c_k.

To prove the semi-definiteness of the matrix, we calculate the smallest eigenvalue e via

$$e = \vec{v}^{\dagger} M \vec{v}, \tag{3.50}$$

where $\vec{v}$ is the normalized eigenvector to the smallest eigenvalue. If all eigenvalues of the matrix are non-negative, the matrix is positive semi-definite; but if the smallest eigenvalue is a negative value, we violate the classical characteristics. Consequently, the smallest eigenvalue achievable for classical states is $e_{cl.} = 0$.

Experimentally, the click counting statistic is given by $c_k^{exp} = C_k/C$ with the number of total events C and C_k denoting the counts for k clicks. The random error is then given as

$$\sigma(\overline{\langle{:}\,\hat{\pi}^l\,{:}\rangle}) = \sigma(\langle{:}\,\hat{\pi}^l\,{:}\rangle) = \sqrt{\frac{1}{C(C-1)} \sum_{k=0}^{N-l} C_k \left(\frac{\binom{N-k}{l}}{\binom{N}{l}} - \overline{\langle{:}\,\hat{\pi}^l\,{:}\rangle} \right)^2} \tag{3.51}$$

with the mean value $\overline{\langle{:}\,\hat{\pi}^l\,{:}\rangle} = 1/C \sum_{k=0}^{N-l} c_k \binom{N-k}{l} / \binom{N}{l}$. The uncertainty of the smallest eigenvalue is then propagated as

$$\Delta e = |\vec{v}|^{\dagger} \Delta M |\vec{v}| \tag{3.52}$$

with ΔM as the matrix of the uncertainties with the elements $\sigma(\overline{\langle: \hat{\pi}^l :\rangle})$. The significance of the measured eigenvalue is then given as $\Sigma = e/\Delta e$. Hence, calculating the smallest eigenvalue of the matrix of moments with the measured click statistics, the nonclassical behavior of the state is shown, so it is the value for nonclassicality, henceforth denoted by $\mathcal{N}$.

In general, from a negative $\mathcal{N}$, we know that the state shows nonclassical properties, that is the amount of nonclassicality. A smaller eigenvalue inevitably does not give us information about a state being more nonclassical since it can only be nonclassical or classical. The statistical significance gives us only a information about the measurement that is the reliability of the measured nonclassicality.

In the following, we discuss a method for obtaining nonclassical quantum correlations between two detected modes or states, making again use of the matrix of moments as it is shown in Ref. [83]. This method can be referred to the previously discussed $g^{(1,1)}$ with an expansion to n photons in each mode. Again, the click-counting statistics of each mode is defined by Eq. (3.46). Consequently, we have to expand it to a multi-mode click-counting statistics as

$$c_{\vec{k}} = \left\langle : \frac{\vec{N}!}{\vec{k}!(\vec{N}-\vec{k})!} \vec{\hat{\pi}}^{\vec{k}} \left(\vec{\hat{1}} - \vec{\hat{\pi}}\right)^{\vec{N}-\vec{k}} : \right\rangle \tag{3.53}$$

with the multi-index notation of $\vec{k}! = k_1! \cdot \ldots \cdot k_D!$ for having D detection systems, with $\hat{\pi}_d = \hat{1} - \exp\left[-\frac{\eta_d \hat{n}_d}{Nd}\right]$ with the individual quantum efficiencies η_d and with N_d on-off detectors for each detection system. Deriving this for the detection of correlated light within two detection systems with $D = 2$, this simplifies to

$$c_{k_1 k_2} = \frac{N_1!}{k_1!(N_1-k_1)!} \frac{N_2!}{k_2!(N_2-k_2)!} \left\langle : \hat{\pi}_1^{k_1} (\hat{1} - \hat{\Pi}_1)^{N_1-k_1} \hat{\pi}_2^{k_2} (\hat{1} - \hat{\pi}_2)^{N_2-k_2} : \right\rangle . \tag{3.54}$$

The matrix of moments for two detection systems is given as

$$M = \begin{pmatrix} 1 & \langle:\hat{\pi}_1:\rangle & \langle:\hat{\pi}_2:\rangle & \langle:\hat{\pi}_1^2:\rangle & \langle:\hat{\pi}_1\hat{\pi}_2:\rangle & \langle:\hat{\pi}_2^2:\rangle & \ldots \\ \langle:\hat{\pi}_1:\rangle & \langle:\hat{\pi}_1^2:\rangle & \langle:\hat{\pi}_1\hat{\pi}_2:\rangle & \langle:\hat{\pi}_1^3:\rangle & \langle:\hat{\pi}_1^2\hat{\pi}_2:\rangle & \langle:\hat{\pi}_1\hat{\pi}_2^2:\rangle & \ldots \\ \langle:\hat{\pi}_1^2:\rangle & \langle:\hat{\pi}_1\hat{\pi}_2:\rangle & \langle:\hat{\pi}_2^2:\rangle & \langle:\hat{\pi}_1^2\hat{\pi}_2:\rangle & \langle:\hat{\pi}_1\hat{\pi}_2^2:\rangle & \langle:\hat{\pi}_2^2:\rangle & \ldots \\ \vdots & \vdots & \vdots & \vdots & \vdots & \vdots & \ddots \end{pmatrix}, \tag{3.55}$$

where we can calculate the moments by

$$\langle: \hat{\pi}_d :\rangle = \frac{1}{N_d} \sum_{k_1=0}^{N_1} \sum_{k_2=0}^{N_2} k_d c_{k_1,k_2} \tag{3.56}$$

$$\langle: \hat{\pi}_d^2 :\rangle = \frac{1}{N_d(N_d-1)} \sum_{k_1=0}^{N_1} \sum_{k_2=0}^{N_2} k_d(k_d-1) c_{k_1,k_2} \tag{3.57}$$

$$\langle: \hat{\pi}_1\hat{\pi}_2 :\rangle = \frac{1}{N_1 N_2} \sum_{k_1=0}^{N_1} \sum_{k_2=0}^{N_2} k_1 k_2 c_{k_1,k_2} \tag{3.58}$$

To show nonclassical-cross correlation between both modes, we calculate again the smallest eigenvalue of the matrix of moments, and if it is negative, we know that the matrix is not positive semi-definite. For classical light, the smallest eigenvalue is equal or greater than zero whereas nonclassical correlations are certified if a value less than zero is determined.

This approach is already used in several experimental works for analyzing the nonclassical character of quantum states, such as shown in Ref. [137], and for probing quantum correlations between different spatial modes [84]. Moreover, a recent work in our group benchmarks the measurement of complex quantum correlations making use of the given approach for analyzing these especially with unique detectors with high photon-number resolution [138].

Chapter

4

State generation with active feedback loops

Contents

In Chap. 3, we have seen that even though the photon generation via parametric down-conversion (PDC) has some limitations, they are the workhorse in nowadays experiments for the generation of single- and multi-photon Fock states. Moreover, we have presented several works that address the multi-photon state generation and some first approaches to mitigate the limitations given by the PDC process itself (see Sec. 3.2.1). In this chapter, we will describe another approach of using parametric down-conversion sources, as a seed for photon adding protocols. The inspiration for this approach was given by theoretical proposals from the groups of Paul Kwiat [55] and Alan Migdall [56]. They proposed the generation of multi-photon Fock states via a cavity-based PDC source (see Sec. 3.2.2 for a detailed description). In contrast, we have no cavity in the sense of a laser, but a time-multiplexed feedback of one generated photon. In fact, with introducing a frequency locking between the pump and the feedback mode, the system would be very similar to a laser cavity.

The focus of this work is on the creation of multi-photon Fock states generated with this novel setup scheme and the analysis of the state fidelity $\mathcal{F}$, the success probability

$\mathcal{P}$ of the state generation and the nonclassicality $\mathcal{N}$ of the generated state. These figures of merit characterize the state quality and generation quantity within our approach for the generation, which makes it comparable with the conventional approach of the state generation, meaning the generation of these states with one single PDC source we have shown previously (see. Sec. 3.2). The Fock state generation is performed via a time-multiplexed scheme in which the generated signal photon seeds the subsequent PDC process via a feedback-loop. Therefore, the state is generated by coherently adding photons to one mode of the PDC process. Every round trip of the state in the setup is heralded by exactly one click in each time bin of the other mode.

In general, we aim for the generation of only one photon pair per step. Keeping this and the discussed limitations in mind, we have seen in Sec. 3.2.1, we expect an enhancement in generation probabilities. First, generating only one photon pair within a PDC process is already enhanced compared to the n-photon case. On a very conceptual basis, we further benefit from the simple fact that we apply $\hat{a}^\dagger$ to a state $|n\rangle$ with $n > 0$ in each round trip. Thus, we increase the generation probability in each step by a theoretical factor of $\sqrt{n+1}$. For example, if we have a mode already containing one photon, we expect a gain factor of $\sqrt{2}$. Furthermore, we expect this behavior to increase with every added photon. We will analyze this on a theoretical basis, with a simple measurement scheme and finally with actually generated Fock states.

Moreover, we find long-range cross correlations between subsequently generated idler photons, which arise due to the quantum feedback in the system.

We introduce this advanced setup and point out the difference to a conventional approach in Sec. 4.1. Firstly, we focus on the properties of the used nonlinear source and then describe the main details of the setup itself. In Sec. 4.2, we will introduce a theoretical framework for our novel setup and describe the simulation and analysis of the setup. Moreover, we will show the theoretical model for ideal system parameters and the resulting fidelities, success probabilities and nonclassicalities. The first fundamental measurements performed within the setup are presented in Sec. 4.3, demonstrating the viability of our approach. The measurement schemes, the analysis and the experimental results for the generated multi-photon Fock states will be shown in Sec. 4.4. We will explain the main differences between the measurement schemes of the conventional approach of the PDC, namely the direct heralding (DH) and compare it to our unconventional approach with the feedback-based PDC source, the feedback heralding (FH). Furthermore, we investigate the correlations between different generated photons within this setup, mainly given between the subsequently generated idler photons in Sec. 4.5. This kind of long-range correlations between photons generated in subsequent PDC processes have not been shown yet. We explain the measurement and analysis schemes and furthermore, the experimental results.

4.1 Setup description

Our approach for generating multi-photon Fock states is a time-multiplexing architecture build around a PDC source (see Fig. 4.1), which renders a seeding of the PDC process

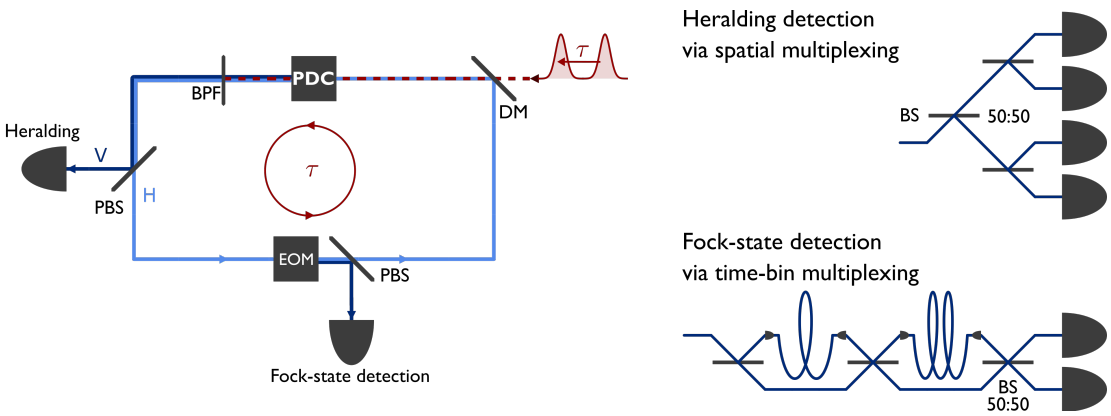

Figure 4.1.: Left: Setup description for the generation of multi-photon Fock states via a time-multiplexed PDC source (DM: dichroic mirror; PBF: bandpass-filter; H: horizontal polarization; V: vertical polarization; PBS: polarizing beam splitter; BS: beam splitter; EOM: electro-optic modulator; τ: repetition rate). Right: Quasi-photon-number-resolved detection schemes for the heralding and the Fock-state detection. For further details, see text. Adapted from [58].

with a previously generated photon. Pump pulses from a laser source at a wavelength of 775 nm enter the setup at a dichroic mirror (DM), which is transmitting light at 775 nm and reflecting light at 1550 nm. The light enters the PDC source and generates a polarization non-degenerate photon pair, called signal (horizontally polarized) and idler (vertically polarized). The pump is finally filtered out at a bandpass-filter (BPF).
Later, we will give a more detailed description of the setup, containing further explanations of the individual parts as well as information about the laser preparation, such as pulse picking, power control, and a 4-f line.

Signal and idler are split up upon propagating though a PBS, where the idler is directly detected via spatially multiplexing photon-number resolving detection scheme with four on-off detectors and serves as herald for the generated multi-photon Fock state. The signal photon propagates through the feedback structure and coincides with the subsequent pump pulse in the PDC source. The repetition rate τ of the laser matches the round-trip time of the signal, which leads to seeding of the second PDC process by the cycling mode. Consequently, detecting exactly one photon in two subsequent time bins in the herald indicates that another photon has been coherently added to the cycling mode. This scheme can be expanded to exactly one photon in each n subsequent time bins, which indicate n coherently added photons to the cycling mode. Therefore, one can imagine the state generation as climbing of a Fock state

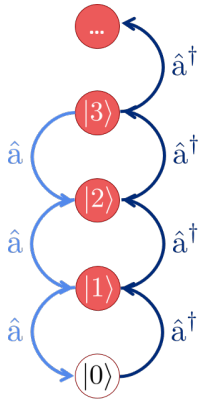

Figure 4.2.: Fock-state ladder.

ladder, where we add with every round trip one photon to the state as illustrated in Fig. 4.2. In each of n round trips, one creation operation $\hat{a}^\dagger$ is realized on the current state, which leads to an climbing of the state to an n-photon Fock state with n coherently added photons. The cycling mode can be detected after out-coupling by a combination of an electro-optic modulator (EOM) and a PBS. The state is then detected with a time-multiplexed, photon-number-resolving detector with eight-bin resolution.

In the following, we will show the characterization of the PDC source used for the photon-pair generation in Sec. 4.1.1 and analyze the linear and non-linear properties of the source. Afterwards, we explain in Sec. 4.1.2 the detailed optical setup and its components, as well as main parts of the alignment and the efficiencies within the setup.

4.1.1 Nonlinear source

The main resource we need for realizing the proposed Fock-state generation is a specially designed and engineered PDC process within the source that is suitable for our purpose. The source we choose has to satisfy certain criteria for our experiment. We want to have a decorrelated source, generating polarization non-degenerate photon pairs, which can be realized in KTP (potassium titanyl phosphate) as a material platform for our PDC process. For realizing the decorrelated source, the phase matching of the source, being dependent on the crystal length and pump bandwidth, must be obeyed. Thus, the length of the crystal should be approximately 8 mm long since the bandwidth of the pump can be adapted within a few nm to match the actual length of the crystal.

Furthermore, we want to generate photons at telecom wavelength, using a conversion process from 775 nm to the aimed wavelength at 1550 nm with a reasonable conversion efficiency. The reason for this wavelength is that 1550 nm is commonly used because of its very low losses in the transmission via optical fibres. This wavelength is also known as telecom wavelength and is inside the C-band (from 1530 nm ro 1565 nm). Accordingly, the lab components and all equipment is optimized for this wavelength to make our systems accessible for commercial application in the future. We want to generate spatially single-mode light for horizontal and vertical polarization and with the lowest possible transmission losses. Both can be realized with rubidium in-diffused waveguides in the KTP crystal.

Having these characteristics in mind, the source of choice is an KTP chip with periodically poled rubidium in-diffused waveguides from the company *AdvR*. The provided source is proposed to have a conversion from (775 ± 1) nm to (1550 ± 2) nm, a length of 8 mm, an expected internal SFG (sum frequency generation) efficiency above 2.5% and is expected to be single mode at 1550 nm. The source containing 30 waveguides, which are divided into five groups, each group contains six waveguides with waveguide width varying from 2 μm to 4 μm. For finding the best possible waveguide, we characterized the waveguides with linear methods, such as determining the spatial mode and waveguide-loss measurements, and non-linear methods, such as SHG, JSI (joint spectral amplitude) and correlation measurements. In the following, we will show the measured

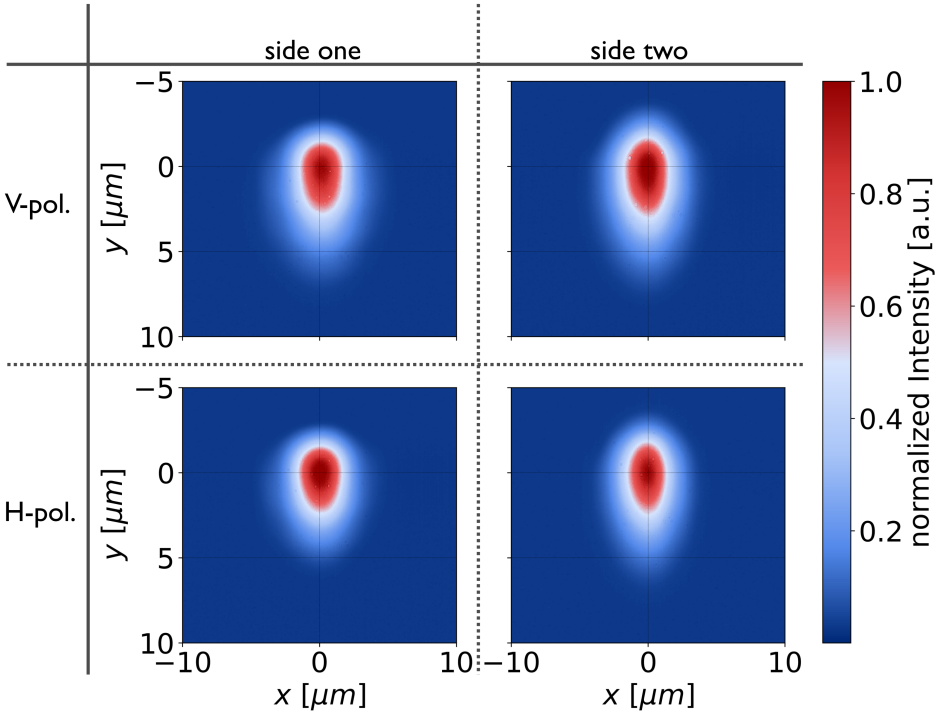

Figure 4.3.: Spectral mode measurements for vertically polarized (V, upper) and horizontal polarized (H, lower) light. The modes are measured for the in-coupling of light from both sides (left for side one and right for side two).

data for the waveguide used for our experiment.

First, we have performed the spatial mode measurement of the waveguides. A laser source at 1550 nm is propagating through the waveguide and the out-coupled mode is imaged using a CCD (charge-coupled device) camera. The polarization of the in-coupled light can be changed by a linear polarizer. This spatial mode measurement for the chosen waveguide is shown in Fig. 4.3, where we have imaged the modes for coupling light into the waveguide from both sides (left and right in Fig. 4.3), as well as with both polarizations (up and down in Fig. 4.3). This can be used to calculate the mode overlap for coupling the mode from one side of the waveguide back into it. The waveguides are

Table 4.1.: FWHM of the measured spatial modes for both sides and both polarizations

side	polarization	$x_{\mathrm{FWHM}}[\mu m]$	$y_{\mathrm{FWHM}}[\mu m]$
one	V	3.12	4.26
	H	3.03	3.88
two	V	3.26	4.45
	H	2.87	4.10

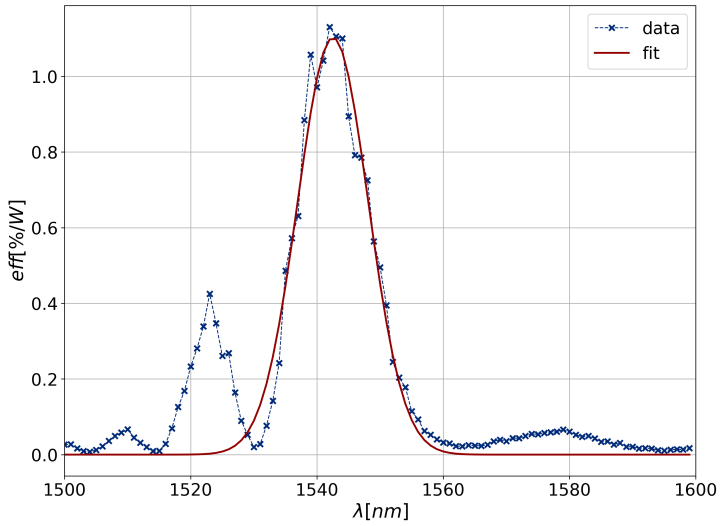

Figure 4.4.: Second harmonic generation measurement for the central wavelength of the conversion via PDC process. The fit refers to the central peak and the side peaks indicate a inhomogeneous poling and a inhomogeneous waveguide.

single mode at the given wavelength and the spatial mode is wider in y-direction (depth) than in x-direction (width). This is linked to the in-diffusion profile of rubidium into the KTP crystal, which is deeper than wide. Further information about this behavior can be found in Ref. [139]. The width of the modes from the first side (left plots) is larger, but less deep than the ones from side two. As we did not produce that particular source in our own group, we do not have any insight into the production. However, we can assume that this might be related to an inhomogeneous diffusion process.

The measured values for the full width at half maximum (FWHM) for the width and the depth can be found in Table 4.1, which proves the impression of the higher depth of the modes of side two. The mode overlap between the two modes from both sides can be calculated by spectral mode measurements, which is 96.7% for the vertical polarized and 96.8% for the horizontal polarized light.

The next linear characterization of the waveguide is the measurement of transmission losses while light is propagating through the waveguides. This measurement is performed by analyzing the contrast between the maxima and minima of the fringes in the Fabry-Perot resonance within the waveguide. The resonator conditions are changed by varying the wavelength of the light coupled in [140]. The propagation loss for horizontally polarized photons is 0.499 dB/cm and 0.399 dB/cm for vertically polarized photons. We can calculate the effective loss in percent by $\eta = 1 - 10^{-\varepsilon/10}$ with the propagation loss ε in dB. Thus, the loss is given as 10.85% for the horizontal and 8.78% for the vertical polarization.

The most important nonlinear characterization is a SHG measurement for estimating the central wavelength of the conversion within the waveguide by performing the counter process of the PDC conversion. We vary the wavelength of the in-coupled light from

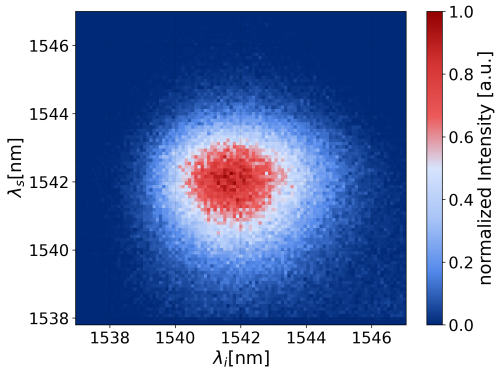

Figure 4.5.: Joint spectral amplitude measurement of the signal and idler photons.

1500 nm to 1600 nm and measure simultaneously the out-coupled power of the converted light at 775 nm and the unconverted light. The effective conversion is then calculated by the ratio of converted light and the square of unconverted light. Figure 4.4 shows the result of the SHG measurement (blue crosses) and the Gaussian fit of the main conversion peak (red). We find that the SHG conversion happens at 1542 nm with a conversion efficiency of 1.10%/W, which leads to pump pulses at a central wavelength of 771 nm. The side peaks are given by the $sinc^2$-term (*sinc* refers to the sine cardinal) in the intensities of the incident fields, which we do not elaborate within this work (see Ref. [67] for further information). It seems that, at 1525 nm, the sidepeaks of the *sinc*-function is even more pronounced than the other peaks, which indicates that the poling and/or the waveguide is inhomogeneous. However, this does not restrict the actual process at 1542 nm.

Another non-linear characterization is based on measuring of the JSI of the waveguide to investigate the filtering of the sidepeaks we see in the SHG measurement. This measurement is performed by sending both signal and idler into separate fiber spectrometers, consisting of dispersive fibers to introduce a temporal delay between the spectral components of the photons. The resulting clicks are recorded and post-selected to the coincident detection events between both fibers. Further details about the method can be found in Ref. [141]. Figure 4.5 shows the JSI being referred to the relative intensities of the coincidence clicks. In this measurement we make use of narrow-band dense wavelength-division-multiplexing (DWDM) filters with a pass bandwidth of 3 nm in both detection arms. Note that the wavelength given for the photons is not as accurate as the SHG measurement since the fiber spectrometers were not calibrated for these measurements. It can be seen that the JSI is nearly a circle, which means, that the two photons are spectral indistinguishable and the source is decorrelated. This is achieved through the property of the source in combination with the filtering. This behavior of signal and idler is required for an ideal heralding of the generated photon pair.

Furthermore, we measure the second-order correlation functions, as described in Chap. 3.3, to investigate the state's characteristics via $g^{(2)}$ and $g^{(1,1)}$. The experimental setup

for measuring these values within the photon-pair generation in a PDC source is depicted in Fig. 4.6. The generated signal and idler photons are split up at a polarizing beam splitter (PBS). The signal photons are then detected (detector label s) in one on-off detector whereas the idler photons are further split up at a BS and then detected in two on-off detectors (i_1 and i_2). The $g^{(2)}$ measurement is performed by coincidence clicks between both idler arms, giving us information about the state's properties (See Sec. 3.3). The second-order correlation function can be used to find the photon-number statistics of the given process. A thermal statistic leads to $g^{(2)} = 2$ and a Poissonian statistic leads to $g^{(2)} = 1$. The PDC process leads to thermal statistics for both modes' marginals [134]. Consequently, we expect to measure a value of two. For calculating this, we have to express Eq. (3.43) in terms of number of clicks, which yields

$$g^{(2)} = \frac{P(i_1 \cap i_2)}{P(i_1)P(i_2)}, \tag{4.1}$$

where $P(i_1 \cap i_2)$ is given by the coincidence clicks and $P(i_{1,2})$ by the clicks in both arms.

As mentioned in Sec. 3.3, the $g^{(1,1)}$ can be interpreted as the probability of generating one click in one mode normalized to the detection of one photon in the other arm. Since we have no photon-number-resolved detection, we cannot distinguish between the detection of exactly and at least one photon. Measuring $g^{(1,1)}$ without photon-number-resolved detection, one has to stay in the very low gain regime. Here, we used a slight different approach for measuring this value. We can detect triple coincidences between the signal and both idler photons. This gives us the probability of generating more than one photon pair since we expect no triple coincidences in a case of only one generated photon pair, so one signal and idler photon. If we generate more than one photon pair, we would likely detect a click in both idler arms. Hence, we would detect simultaneously a click in all three arms. We can refer to this as a heralded $g^{(2)}$, measuring conditional probabilities

$$g_h^{(2)} = \frac{P(i_1 \cap i_2|s)}{P(i_1 \cup i_2|s)^2} = \frac{P(i_1 \cap i_2 \cap s)P(s)}{[P(i_1 \cap s) + P(i_2 \cap s)]^2}, \tag{4.2}$$

with the three-fold coincidence $P(i_1 \cap i_2 \cap s)$ and the single clicks of the signal $P(s)$. Therefore, the smaller this value is, the higher the single photon purity. A source generating only one photon pair would show $g_h^{(2)} = 0$.

The measured values are given as $g^{(2)}$=1.941 $\pm$ 0.011 and $g_h^{(2)} = 0.027 \pm 0.001$ at a pulse energy of $0.5 \cdot 10^{-11}$J. It is noteworthy that both values are strongly dependent on the pump intensity (or the mean photon number) of the pump pulses. In general, the experiments are performed at intensities, which show the given values for the $g^{(2)}$ and $g_h^{(2)}$.

4.1.2 Feedback in parametric down-conversion

In this section, we describe important details of the setup, the alignment as well as efficiencies. Starting with a detailed description of the setup, as it is sketched in Fig. 4.7, we

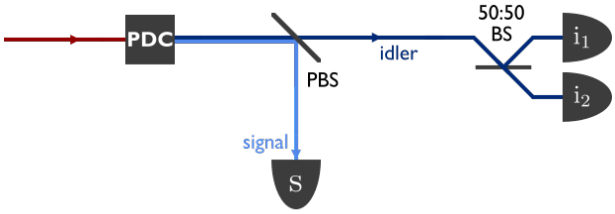

Figure 4.6.: Sketch of the measurement performed to calculate $g^{(2)}$ and heralded $g^{(2)}$ of the source.

see that it consists of five major parts: the pulse picking for the number of pump pulses entering the setup (red), the PDC source (orange), the delay stage to match the repetition rate and the round-trip time (grey), the detection (green), divided in the heralding and Fock-state detection, and the state out-coupling (purple). The pump light is shown by the red lines, the blue lines indicate the feedback path and the light blue lines the detection paths. Further parts of the setup not drawn in Fig. 4.7 are a laser power control and the pulse shaping. The power control for the measurements is performed by a HWP and a PBS. The transmitted light is send to the setup and the reflected light is sent to a beam block. By changing the polarization of the initial light different ratios of the total intensities are is transmitted and reflected, leading to a control of the power of the pump light. Furthermore, we try to match the bandwidth of the pump with the actual crystal length as best as possible to ensure maximal phase matching. The adaption of the bandwidth of the pump is performed via a 4f configuration to filter the pump to the required spectral bandwidth. The 4f-line consists of a mirrored arrangement of a grating and a lens with a slit in the center, where all elements are separated by the focal length of the lens.

The PDC source is already fully described in Sec. 4.1.1 since we characterized it before aligning it to the setup. Firstly, we started to align the PDC source and the feedback without the pulse picking and out-coupling stage. The pump pulses are in- and out-coupled through the waveguide in the KTP chip via two lenses. The anti-reflection coating on the end facets of the source, as well as on the lenses, is mainly optimized for 1550 nm since the in-coupling of the pump pulses is not as important as optimizing the feedback of the cycling mode. An optimization of both wavelengths simultaneously is a hard task, where one wavelength is usually preferred.

The feedback path is then aligned with mirrors such that the path length is matching the repetition rate of the laser. Thus, the photon cycling the feedback is matched with the subsequent pump pulse. The path is then approximately $L = \tau \cdot c = 3.944\,\mathrm{m}$ with $\tau = 76\,\mathrm{MHz}$. The fine tuning of the length is then achieved by adjusting the delay stage. But before fine tuning the length, we have to align the feedback into the source.

We match the feedback path to the pump path for ensuring that we match the in-coupling back into the source. Since we can not directly check if the feedback is coupled back because of blocking the beam while directly measuring, we have to perform two

different measurements to check the roundtrip and in-coupling efficiency. Initially, we use an alignment continuous-wave (cw) laser with a wavelength at 1550 nm, which is coupled into the setup at the free port of PBS-2, which we usually use for the out-coupling of the state. The light, which is vertically polarized, propagates through the waveguide and is then measured by a power meter after PBS-1 (reflected port), which serves as a reference value for the light traveling through the feedback. Subsequently, the light is transformed into horizontally polarized light by the HWP in front of PBS-1, which leads to a propagation through the feedback path (transmission through PBS-1 and PBS-2) and the source. At the halfwave-plate the light is transformed back into vertically polarized light, which leads to a reflection at PBS-1 and a measurement by the power meter. The ratio of this value with the reference leads to a loop propagation efficiency of 72%. We have performed a detailed efficiency assessment of all components of your setup, which comprises the losses of every individual component. We find

$$\begin{aligned}\eta_{\text{total}} &= \eta_{\text{mirrors}}^{n} \cdot \eta_{\text{EOM}} \cdot \eta_{\text{DM}} \cdot \eta_{\text{BPF}} \cdot \eta_{\text{PDC}} \cdot \eta_{\text{PBS}}^{2} \cdot \eta_{\text{HWP}}^{2} \\ &= 0.99^{7} \cdot 0.995 \cdot 0.99 \cdot 0.975 \cdot 0.85 \cdot 0.98^{2} \cdot 0.99^{2} \\ &= 0.7511,\end{aligned} \tag{4.3}$$

which fits quite well to the experimentally achieved efficiencies. Thus, the measured efficiency is only slightly below the theoretical value. This can be caused by differences in the efficiencies given by the companies providing the components and the actual efficiency.

As a next step, we have to make sure that the length of the feedback path matches the repetition rate of the laser since every component light is propagating through (e.g. EOM) changes the effective path length from the directly measurable path length. The most important point to mention here is that the repetition rate of our laser system, a MIRA 900D from *Coherent*, is synchrolocked to a fixed repetition rate of 76 MHz. Without this locking, the overlap between the cycling mode and the subsequent pump pulses would change during one measurement due to a mismatch between feedback path and repetition rate, decreasing the seeding of the subsequent PDC processes. A sychrolock system is provided by *Coherent* and makes it possible to lock the pulse repetition rate of the laser to an external radio-frequency source. Dampers within the laser cavity compensate for frequencies differing from the set frequency. They are monitored by a high-speed photodiode. The locking to the second harmonic of the photodiode signal is used to have a very low jitter of 55 fs in the repetition rate.

To investigate the matching of the laser repetition rate and the feedback path length, we perform a SHG measurement within the setup. We make use of the fact that the SHG process needs vertically and horizontally polarized light at 1550 nm to convert it into light pulses at 775 nm. Hence, one polarization is delayed within the feedback path, which means that we only measure SHG if the delayed path matches the next pump pulse. This is done by using a laser with pulses at 1550 nm wavelength, here a *OneFive* ORIGAMI laser with a repetition rate locked to the actual pump laser. The light enters the setup from the heralding detection part, where the vertically polarized pulses enter the source, travel through the loop and are then transformed into horizontal polarization

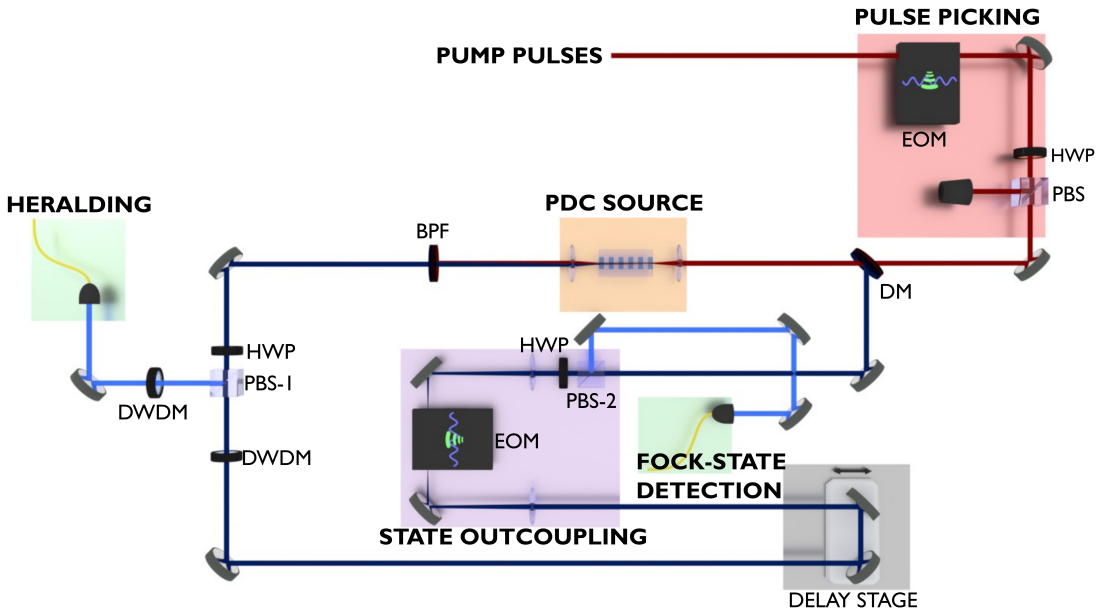

Figure 4.7.: Detailed sketch of the feedback PDC setup, which is close to the actual setup in the laboratory (DM: dichroic mirror; PBF: bandpass-filter; PBS: polarizing beam splitter; EOM: electro-optic modulator; τ: repetition rate; HWP: half-wave plate; DWDM: dense wavelength division multiplexing). For further details, see the text.

by a halfwave-plate (HWP). If then the next vertically polarized and the horizontally polarized pulse overlap in the source, an SHG conversion occurs. This is measured with a power meter after the dichroic mirror since we then see only the light at 775 nm. Moving the delay stage, we see a peak in the measured light, indicating the maximal overlap between the feedback path and the repetition rate.

Afterwards, we align the detection paths for the herald and the state detection, for which we use again the alignment laser. The light is coupled into low loss single-mode fibers, optimized for telecom wavelength, with a coupling efficiency of around 80%. The used detectors are superconducting nanowire single-photon detectors (SNSPDs) from *Photon Spot*. In Fig. 4.8, we show an exemplary time line for the pulses in the herald detection and the signal detection, and we know that every single measurement is started after 1 μs. We pump the source with a pulse train of n pulses which leads to the detection of up to n clicks in the n time bins of the herald. Thus, the herald pulses have a separation of 13.16 ns, being equivalent to the laser repetition rate. The cycling mode is sent to the detection via the EOM after a specified number of roundtrips; this happens at a rate of 1 μs. Consequently, the herald detection requires a very low deadtime, which are only accessible with a lower efficiency. We make use of detectors with a efficiency of 75% and a deadtime of 10 ns for the heralding. Since, we do not need a very low deadtime in the state detection, we make use of the more efficient detectors with a efficiency of 95%

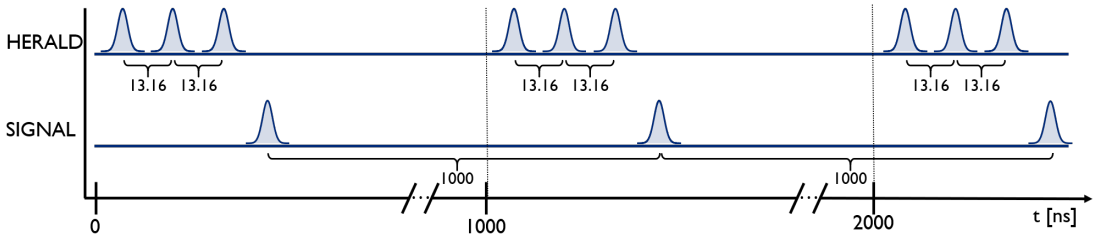

Figure 4.8.: Exemplary time graph for the pulses of the heralding and the signal detection for three initial pump pulses. Every measurement starts after 1 μs.

and a deadtime of 60 ns. As a parameter of the overall detection efficiencies, including all elements the photons pass through (e.g. PBS, fibers), we calculate the commonly known, so-called Klyshko efficiency, accounting also for the pairwise generation of the two photons and false clicks. For calculating this efficiency, we detect idler and signal (direct out-coupling at PBS-2), each with one of the fast detectors, and measure the single clicks in each arm, as well as the coincidence rate between both arms. The Klyshko efficiencies of signal η_s and idler η_i are then calculated as

$$\eta_s = \frac{P(s \cap i)}{P(i)} \quad \text{and} \quad \eta_i = \frac{P(s \cap i)}{P(s)}, \tag{4.4}$$

with the coincidence rate $P(s \cap i)$ between both and the single clicks $P(i)$ of the idler and $P(s)$ for the signal. We have measured an efficiency for idler $\eta_i = 0.39$ and for signal $\eta_s = 0.38$. Having a look at the components between the source and the detection one can calculate the theoretical value as

$$\begin{aligned} \eta_\mathrm{i} &= \eta_\mathrm{mirrors}^2 \cdot \eta_\mathrm{BPF} \cdot \eta_\mathrm{HWP} \cdot \eta_\mathrm{PBS} \cdot \eta_\mathrm{DWDM} \cdot \eta_\mathrm{fibre} \cdot \eta_\mathrm{det} \\ \eta_\mathrm{s} &= \eta_\mathrm{mirrors}^9 \cdot \eta_\mathrm{BPF} \cdot \eta_\mathrm{HWP}^2 \cdot \eta_\mathrm{PBS}^2 \cdot \eta_\mathrm{DWDM} \cdot \eta_\mathrm{EOM} \cdot \eta_\mathrm{fibre} \cdot \eta_\mathrm{det}, \end{aligned} \tag{4.5}$$

with the final result of $\eta_i = 0.4361$ and $\eta_s = 0.4015$. We see that the finally achieved Klyshko efficiencies and the theoretical calculations exhibit only slight differences.

In contrast to this efficiency bookkeeping, we have to perform a deterministic out-coupling out of the feedback path of the signal photons by an active switching of the polarization by the EOM for the actual measurement. This leads to the adjustment of the EOM switches for the pulse picking and the Fock-state detection. The electro-optic modulator contains a rubidium titanyl phosphate crystal, to which an electric field can be applied. Due to the electro-optical effect of the crystal, it switches the polarization of the light while traveling through the crystal if we apply an electric field. The picked pulses are transmitted at the PBS whereas the unpicked ones are reflected. The HWP is used to match the polarization axis of EOM and PBS for an optimized pulse picking. For the state out-coupling, the polarization is swapped from horizontal to vertical polarization so that the state out-coupling is performed by reflection at PBS-2. In general, the approach for the measurement is that, for an n-photon Fock state, we pump the source with n

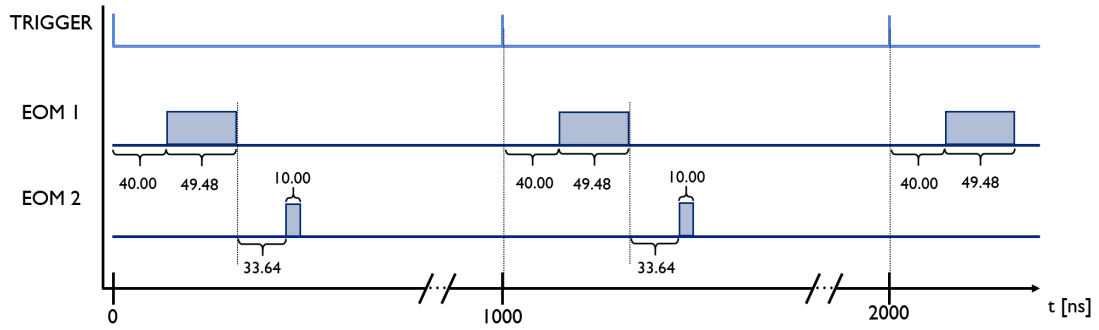

Figure 4.9.: Time graph for the EOM switching for a four-photon Fock state: Every 1 MHz the trigger sends a signal to the EOMs; after the given timings they switch on and off.

pump pulses and they travel $n-1$ times the feedback path before they are swapped out of the system into the Fock-state detection path.

Hence, we have to match the switching of the two EOMs such that we match these conditions for the measurement. The start of every measurement is given by a trigger from the laser, which is reduced to 1 MHz. The start of the switching of the first EOM is 40 ns after the trigger, which is caused by the path the light travels between laser and the EOM. The duration for applying the electric field to the first EOM is calculated by

$$\Delta t_{\mathrm{EOM1}} = (n-1) \cdot 1/\tau + 2 \cdot t_{\mathrm{safety}}, \tag{4.6}$$

where n is the number of pump pulses entering the setup, τ is the repetition rate of the laser and t_{safety}=5 ns is added to ensure that the pulses are picked completely. Hence, the sum of the delay between the trigger and the switch of the first EOM and the time for applying the field gives the time to switch of the field after the trigger signal. Accordingly, the electric field for the second EOM is switched on after

$$t_{\mathrm{EOM2\ start}} = 40\,ns + t_{\mathrm{EOM\ delay}} + n \cdot 1/\tau, \tag{4.7}$$

where $t_{\mathrm{EOM\ delay}}$ = 20 ns gives the delay between the switching of both EOMs. The switch ends after 10 ns since we only pick exactly the cycling mode after the given number of round trips. An example for the timings of the switching for a four-photon Fock state is given in Fig. 4.9, where we show the time graphs of the switching for the EOMs with respect to the trigger signal. The trigger is applied every 1 MHz, where the first EOM switches after 40 ns for 49.48 ns and the second EOM switches 33.64 ns after the first EOM for a duration of 10 ns.

Finally, we have to discuss the detection schemes used during the measurements. In general, the already mentioned detectors are on-off detectors, which have the characteristics that they only give a binary signal, a click for at least one detected photon and no click otherwise, which, in this case, is not sufficient for the heralding and state detection. For the heralding and state detection, we need the information of the number of

generated photons in every mode, so the click counting statistic, which makes a photon-number resolution necessary. Therefore, we make use of two different approaches for the quasi photon-number resolved detection: spatial multiplexing and time-multiplexing. In both detection schemes, we split the given signal with 50:50 beams splitter into in four bins or eight bins, respectively. In this context, "quasi" means that there is a residual, non-zero probability that two photons enter the same path but are only counted as one single click. Indeed, the more splitting the scheme performs with respect to the expected photon number, the higher is the resolution and the lower is the probability of detecting several photons in one arm. Spatial multiplexing means here that we split the signal with a cascade of 50:50 beam splitter into four on-off detectors, as it is already demonstrated in Fig. 4.1 right. The time-multiplexed detection scheme is performed by separating the signal first at a 50:50 beam splitters and then shift them in time with different fiber lengths. This is conducted two times and with three 50:50 beams splitter, which ends into four time bins for each of the two detectors (see also Fig. 4.1 right). For further information about the detection probabilities and the measurement schemes, see Refs. [80–84].

4.2 Theoretical framework for active feedback loops

The novelty of our proposed scheme for generating Fock states requires a unified theoretical framework for the description, simulation and analysis of the Fock-state generation, in particular, since most of the analysis schemes cannot directly be applied to the measured click statistics, but only to the photon statistics. The inversion of the click statistics into the photon statistics is always an ill-defined problem (no inversion from finite click numbers onto infinite photon numbers) and could lead to non-physical results. Therefore, our analysis is based on the click statistics, which are measurable in the laboratory. The content of this section was published in Ref. [57].

For the following studies of this particular theory framework, we need a set of operators. The main element of all considerations is the photon-number operator $\hat{n}{=}\hat{a}^\dagger\hat{a}$ with the annihilation operator $\hat{a}$. For our purposes, we use the exponential of the number operator in normal-ordering prescription

$$\hat{E}(x) = x^{\hat{n}} = :\exp([x-1]\hat{n}):, \tag{4.8}$$

where we get the identity $\hat{1}$ for $x = 1$, for $x = 0$ we have the vacuum projector $|0\rangle\langle 0|$ and for $x = -1$ the parity operator $(-1)^{\hat{n}}$. In the following, we restrict ourselves to a range from $0 \leq x \leq 1$ and rephrase this in terms of the photon-number expansion

$$\hat{E}(x) = \sum_{n\in N} x^n \, |n\rangle\langle n| \,, \tag{4.9}$$

which means, that the function $\hat{E}$ carries concurrently the information about all photon-number states.

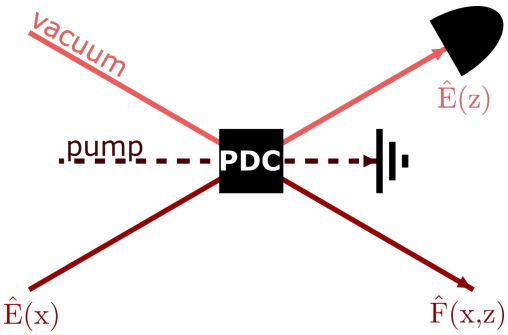

Figure 4.10.: Schematic description of the nonlinear process in a feedback loop. For further details, see text. Reprinted and adapted from [57].

The photon pair generation within a PDC process was defined in Eq. (3.28). The PDC unitary operator can be rewritten as [142]

$$\hat{S} = \frac{1}{\mu} e^{-\nu \hat{a}^\dagger \otimes \hat{a}^\dagger / \mu} \left(\frac{1}{\mu}\right)^{\hat{n}} \otimes \left(\frac{1}{\mu}\right)^{\hat{n}} e^{\nu^* \hat{a} \otimes \hat{a} / \mu} \tag{4.10}$$

with $\mu = \cosh|\zeta|$, $\nu = e^{i \arg \zeta} \sinh|\zeta|$ and the squeezing parameter ζ, which is proportional to the amplitude of the optical pump, coupling parameters and interaction times [1]. In the following, when we talk about the value of ζ, we will use the term squeezing. This is more common in the continuous-variable (CV) picture but will be used here for representing the pump intensity. The generated state can be further written as

$$\hat{S}(|0\rangle \otimes |0\rangle) = |\lambda\rangle = \sqrt{1 - |\lambda|^2} \sum_{n=0}^{\infty} \lambda^n |n\rangle \otimes |n\rangle \tag{4.11}$$

with $\lambda = -\nu/\mu$. Furthermore, we define the intensity gain factor as

$$\gamma = \mu^2 = \cosh^2|\zeta| = \frac{1}{1 - |\lambda|^2} \geq 1. \tag{4.12}$$

A sketch of the conceived process is depicted in Fig. 4.10. We consider one input mode for the PDC process to be a vacuum state ($\hat{E}(y)$ with $y = 0$ called vacuum in the figure), whereas the other mode is a seed with $\hat{E}(x)$. The pump field is pumping the source and filtered afterwards. The description of the process with two input modes is not discussed further in this context but can be found in Ref. [57].

One output mode $\hat{E}(z)$ is detected for a conditional measurement, in our case as a heralding of the second cycling mode $\hat{F}(x, z)$, which can be calculated by

$$\begin{aligned} \hat{F}(x,z) &= \mathrm{id} \otimes \mathrm{tr}\left(\left\{\hat{S}\left[\hat{E}(x) \otimes |0\rangle\langle 0|\right]\hat{S}^\dagger\right\}\left[\hat{1} \otimes \hat{E}(z)\right]\right) \\ &= \frac{1}{\gamma}\hat{E}\left(\frac{x}{\gamma} + \frac{[\gamma - 1]z}{\gamma}\right). \end{aligned} \tag{4.13}$$

[1] This operation is in the CV picture commonly known as squeezing operator.

Hence, the seeded nonlinear process leads to an input-output relation in form of $\hat{E}(x) \mapsto \hat{F}(x,z)$.

Assuming to have n photons in the cycling mode, a projection onto m photons in the output $\hat{E}(z)$ is performed. With the relation $|n\rangle\langle n| = (1/n!)\partial_x^n \hat{E}(x)|_{x=0}$ we find for the output mode

$$\begin{aligned}\hat{F}_{n,m}(x,z) &= \mathrm{id} \otimes \mathrm{tr}\left(\hat{S}\,|n\rangle\langle n| \otimes \hat{S}^\dagger \left[\hat{1} \otimes |m\rangle\langle m|\right]\right) \\ &= \frac{(\gamma-1)^m}{\gamma^{m+n+1}} \frac{(m+n)!}{m!n!}\,|m+n\rangle\langle m+n|\,.\end{aligned} \tag{4.14}$$

This shows, the coherent addition of m photons to the initial n photons in the cycling mode. The success probability corresponds then to the preceding factor of the output state $|m+n\rangle\langle m+n|$.

Accordingly, we still need an expression for the detection of both modes. A positive operator-valued measure of an on-off detector is given as

$$\begin{aligned}\hat{\Pi}_{\mathrm{off}} &= e^{-\delta}\hat{E}(1-\eta) \;\text{ and} \\ \hat{\Pi}_{\mathrm{on}} &= 1 - \hat{\Pi}_{\mathrm{off}}.\end{aligned} \tag{4.15}$$

The dark count contribution is given by δ and the detection efficiency is given by η. We formulate the detection scheme more general and introduce multiplexed detection with splitting of the signal via beam splitters into N detectors, each with a identical intensity. The measurement operator to obtain $K \in \{0,\ldots,N\}$ clicks is then

$$\hat{\Pi}_K = \sum_{J=0}^{K} \binom{N}{K}\binom{K}{J}(-1)^{K-J}\hat{E}(J/N), \tag{4.16}$$

with a vector type representation of $([\binom{N}{K}\binom{K}{J}(-1)^{K-J}, J/N])_{J\in[0,\ldots,N]}$ to account for the individual components in the sum.

In the following, we transfer the given expressions into a vector-type representation to make our framework more accessible from the experimental point of view. We make use of the density operator $\hat{\rho}$ representation since this representation gives phase-averaged states and diagonal in the photon-number basis, meaning that we do not have to perform phase-sensitive measurements. The density operator $\hat{\rho} = \sum_k P_k \hat{E}(x_k)$ is then identified with an array of pairs to represent every product in the sum like $\vec{\rho} = ([P_k, x_k])_k$.

For example, a thermal state given as

$$\hat{\rho}_{\mathrm{th}} = \frac{1}{\bar{n}+1}\hat{E}\left(\frac{\bar{n}}{\bar{n}+1}\right) \tag{4.17}$$

would be written by $\vec{\rho}_{\mathrm{th}} = [1/(\bar{n}+1), \bar{n}/(\bar{n}+1)]$.

Next, we need to define the measurement representation similar to the state representation. Starting with $\hat{\Pi} = \sum_l \pi_l \hat{E}(\omega_l)$, the vector type representation of the measurement

is given as $\vec{\Pi} = ([\pi_l, \omega_l])_l$. Consequently, we can calculate the expectation value by

$$\mathrm{tr}(\hat{\rho}\hat{\Pi}) = \sum_{k,l} \frac{P_k \pi_l}{1 - x_k \omega_l} = (\vec{\rho}, \vec{\Pi}). \tag{4.18}$$

Here, $(\vec{\rho}, \vec{\Pi})$ defines an inner-product-type functional of the state and measurement representation. The normalization of the state $\hat{\rho}$ can be calculated as $(\vec{\Pi}, \vec{\rho}) = \sum_k P_k/(1-x_k)$ with $\vec{\Pi} = \vec{1}$. Hence, if a state not is properly normalized, we find $(\vec{1}, \vec{\rho}) < 1$, also resembling the success probability for generating a certain state.

The last part we mention is the process representation, where each process is given by an input-output relation $\hat{\rho} \mapsto \Lambda(\hat{\rho})$ with a model of the evolution Λ. Furthermore, $\hat{\Pi} \mapsto \Lambda^\dagger(\hat{\Pi})$ defines how the process act on the measurement operator. In general, $\Lambda(\hat{\rho})$ relates to the state-based Schrödinger picture, whereas $\Lambda^\dagger(\hat{\Pi})$ relates to the measurement-based Heisenberg picture. The composition of two processes is combined to a overall process via $\Lambda(\hat{\rho}) = \Lambda''(\Lambda'(\hat{\rho}))$ and $\Lambda^\dagger(\hat{\Pi}) = \Lambda'^\dagger(\Lambda''^\dagger(\hat{\Pi}))$.

The loss within the detection of a state is typically modeled as

$$\Lambda^\dagger[\hat{E}(\omega)] = \hat{E}(\eta\omega + 1 - \eta), \tag{4.19}$$

again with the detection efficiency η. In turn, Λ acts on the measurement vectors as

$$\Lambda^\dagger(\hat{\Pi}) = ([\pi_l, \eta\omega_l + 1 - \eta]). \tag{4.20}$$

We find then for the adjoint operator

$$\begin{aligned} \Lambda(\hat{E}(x)) &= \frac{1}{1 - [1-\eta]x} \hat{E}\left(\frac{\eta x}{1 - [1-\eta]x}\right) \\ \Lambda(\vec{\rho}) &= \left(\left[\frac{P_k}{1 - [1-\eta]x_k}, \frac{\eta x_k}{1 - [1-\eta]x_k}\right]\right) \end{aligned} \tag{4.21}$$

describing the action of the loss channel Λ onto the state vector. Additionally, we find that the loss of two channels can be expressed by one loss channel with $\eta = \eta' \eta''$.

Starting again with our scheme shown in Fig. 4.10, we express our input-output relation as

$$\hat{F}(x, z) = \frac{1}{\gamma} \hat{E}\left(\frac{x + [\gamma - 1]z}{\gamma}\right) = \Lambda(\hat{E}(x)). \tag{4.22}$$

Hence, we can calculate the inner product with

$$\begin{aligned} \mathrm{tr}(\Lambda[\hat{E}(x)]\hat{E}(\omega)) &= \mathrm{tr}(\hat{E}(x)\Lambda^\dagger[\hat{E}(\omega)]) \\ &= \frac{1}{\gamma - [\gamma - 1]z\omega} \frac{1}{1 - x\frac{\omega}{\gamma - [\gamma-1]z\omega}} \end{aligned} \tag{4.23}$$

enabling us to obtain the impact of the process on the measurement. We find for the input-output relations of process and measurement for the special case of $z = 1$

$$\begin{aligned} \lambda(\vec{\rho}) &= \left(\left[\frac{P_k}{\gamma}, \frac{x_k + [\gamma - 1]}{\gamma}\right]\right)_k \\ \Lambda^\dagger(\vec{\Pi}) &= \left(\left[\frac{\pi_l}{\gamma - [\gamma - 1]\omega_l}, \frac{\omega_l}{\gamma - [\gamma - 1]\omega_l}\right]\right)_l, \end{aligned} \tag{4.24}$$

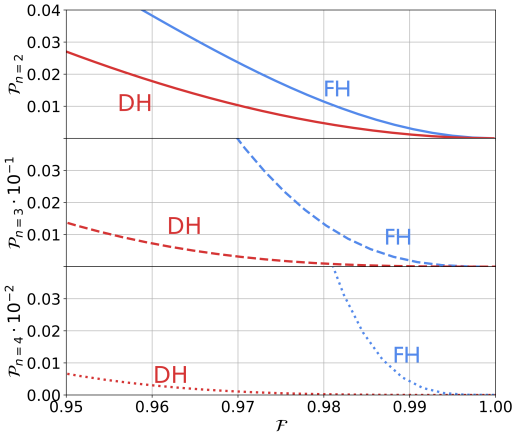

Figure 4.11.: The relation of state fidelity $\mathcal{F}$ and success probability $\mathcal{P}$ of the generated n-photon Fock states for the lossless case by varying the squeezing $|\zeta|$. We perform this analysis for $n = 2$ (top, solid), $n = 3$ (middle, dashed) and $n = 4$ (bottom, dotted) for the feedback heralding (FH, shades of blue) and as a comparison for the direct heralding (DH, shades of red).

corresponding to the tracing over the heralding in Fig. 4.10.

Hence, we have now a full theoretical framework for applying this to our proposed setup shown in Fig. 4.1 (left), leading to

$$\begin{aligned} \hat{\rho} \mapsto \hat{\rho}_{\hat{\Pi}} &= \sum_{k,l} P_k \pi_l \hat{F}(x_k, z_l) \\ \vec{\rho}_{\text{out}} = \Lambda(\vec{\rho}_{\text{in}}) &= \left(\left[\frac{P_k \pi_l}{\gamma}, \frac{x_k + [\gamma - 1] z_l}{\gamma} \right] \right)_{k,l} \end{aligned} \tag{4.25}$$

for the output state of the cycling mode.

Analyzing the quality of the generated state within this approach leads to three main figures of merit: the state fidelity with the target state, the success probability and the nonclassicality of the generated state. In general, we perform here a joint analysis of the success probability and the fidelity, similar to the analysis we have already seen in Sec. 3.2.1. Previously, we have talked about the generation probability but here introduce the success probability as a parameter for the generation quantity. As already mentioned, the generation probability is calculated from the photon statistics, which are hard to extract from the click statistics, whereas the success probability is calculated directly from the click statistics.

The fidelity of the generated state $\hat{\rho}$ with an n-photon state is calculated via

$$\mathcal{F}(\hat{\rho}, |n\rangle\langle n|) = \text{tr}(\hat{\rho}\,|n\rangle\langle n|) = \sum_k P_k x_k^n \tag{4.26}$$

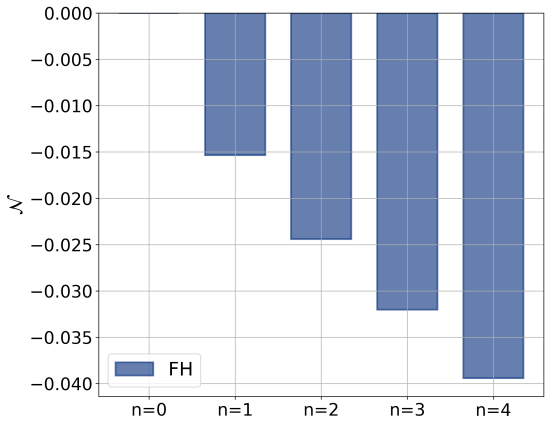

Figure 4.12.: Nonclassicality of FH for vacuum $n = 0$, a single photon $n = 1$ and multi-photon Fock states, $n = 2, 3, 4$, calculated for the lossless case for a squeezing of $|\zeta| = 0.3$.

and the success probability can be calculated via

$$\mathcal{P} = \frac{\mathrm{tr}(\hat{\rho}_{\hat{\Pi}})}{\mathrm{tr}(\hat{\rho})} = \frac{(\vec{\rho}_{\mathrm{out}}, \vec{1})}{(\vec{\rho}_{\mathrm{in}}, \vec{1})}. \tag{4.27}$$

The theoretical prediction of the joint analysis of fidelity and success probability is given in Fig. 4.11 for $n = 2, 3, 4$ photons (from top to bottom in solid, dashed, dotted). For comparison, we perform the analysis for all states for the feedback heralding (FH, blue) and for the direct heralding (DH, red). The calculations are performed for the detection schemes given in Fig. 4.1 (right). We can see for this lossless calculations a significantly enhanced performance, especially regarding success probability for the FH compared to the DH, which is even more pronounced, the higher the photon numbers. Let us have a deeper look into the enhancement for a fixed fidelity of $\mathcal{F} = 0.98$ for all photon numbers. We find that the success probability for $n = 2$ is approximately 2.3 times higher in the FH compared to the DH, increasing to a 17-fold higher probability for the three-photon case and to approximately 200-fold higher probability for $n = 4$. This enhancement of the success probability is dependent on the target fidelity as the difference decreases for higher fidelity and increases for lower fidelities. We expect this effect to be lower in the experimental data since the lower efficiencies play an important role in these calculations. Nevertheless, we see an advantage of our approach for generating multi-photon Fock states, aiming especially for the increase of success probability–and in this sense also generation probabilities–comparing it to the DH.

We analyze additionally to the state quality and generation quantity, also the non-classical character of the generated states by using a method based on the matrix of moments of the click-counting statistics, which is introduced in Sec. 3.3, and is mainly based on Ref. [84]. For classical light, the matrix of moments is positive semi-definite.

These constrains can be put into a form of

$$\mathcal{N} = \frac{(\mathrm{tr}[\hat{\rho}\hat{E}(1)])(\mathrm{tr}[\hat{\rho}\hat{E}(0)])}{(\mathrm{tr}[\hat{\rho}\hat{E}(1/2)])^2} - 1 \geq 0 \tag{4.28}$$

within our theoretical framework. Nonclassical quantum states violate the positive semi-definiteness of the matrix of moments given by a negative $\mathcal{N}$.

In Fig. 4.12, we have performed a analysis of the lossless case for a squeezing of $|\zeta| = 0.2$ with the detection schemes used in the latter measurement for vacuum ($n = 0$), for single photons (no loop, same as with D, $n = 1$) and for a multi-photon Fock state with $n = 2, 3, 4$ photons within the FH. All generated states exhibit a nonclassical behavior, which is even stronger, the higher the photon number is. As consistency check of our method, we show the nonclassicality of vacuum, which is expected to be equal to zero, which we see also in the data. For higher photon numbers we expect, the nonclassicality to converge because of detector saturation.

In summary, we have presented a theoretical framework for the realistic description of our experiment being fully described in terms of the measured quantities. This framework includes all higher photon-number contribution (no approximation, cutoffs), all efficiencies, a finite photon-number resolution and detector saturation effects. The analysis can be performed without a Taylor expansion of the unitary operator of the PDC-Hamiltonian, as used previously, leading to no restrictions to low squeezing parameters. We have defined parameters for analyzing our data, such as a nonclassicality assessment and made predictions for success probabilities and fidelities.

4.3 Stimulated generation via feedback in parametric down-conversion

In this section, we investigate the feedback-induced characteristic of the setup leading to an enhancement in the generation of photons in the cycling mode. The main focus is a simple measurement without EOM switching and without quasi-photon-number-resolved detection such that it is easily seen whether the stimulation of the PDC process is working as intended. Hence, we pump the source continuously at 76 MHz and only detect the heralding photon with one on-off detector, and the signal mode is continuously cycling in the feedback loop. The measurement we perform is the correlation of the first click (after the trigger) with the subsequent ones.

The measurement scheme is drafted in Fig. 4.13, with the upper plot showing the measurement scheme for the feedback heralding (FH) and the lower plot the direct heralding (DH). Here, we depict the scheme for the setup not in a looped configuration, but in a linear configuration to demonstrate the main differences between FH and DH. Within both measurements, every idler photon is detected and for the FH the signal photons enter the next PDC process whereas the signal for the DH is blocked. Furthermore, the FH system encounters for a given loop propagation loss η_{loop}, which does not play any role in the DH. The measurement gives the correlation within the clicks in the idler detection channel, meaning the time difference between the clicks. Thus, each click acts as a start signal for each time bin and as stop signal for the preceding bin. In general, positive and

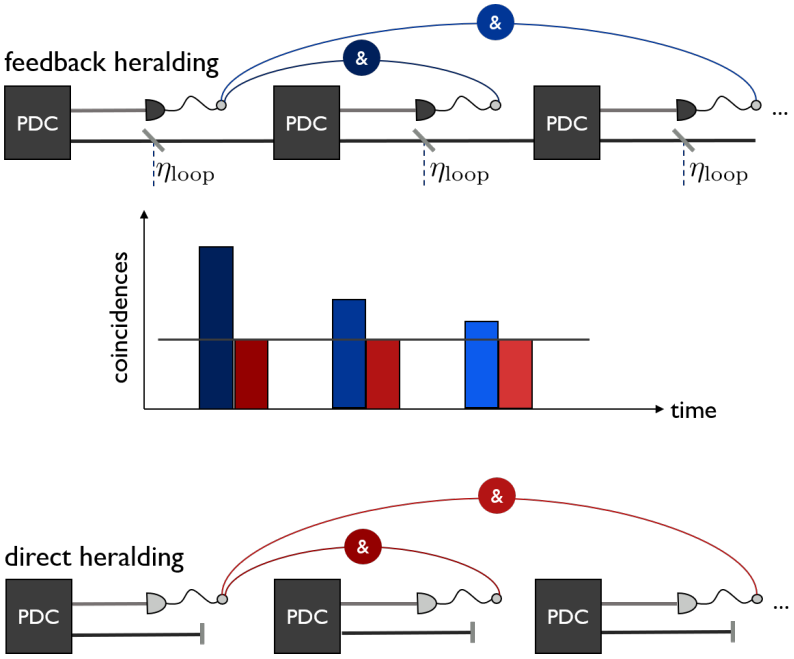

Figure 4.13.: Measurement scheme for the correlation with the FH (upper plot) and the DH (lower one). The expected result is shown in the middle plot, where we measure the coincidence clicks for the different time bins with the first click.

negative time differences are considered, leading to a symmetric distribution. We only take the positive time differences to have a closer look into the coincidences between the first and the next measured click.

The middle plot in Fig. 4.13 shows our expected result from these measurements, with the red bars being assigned to the DH and the blue bars to the FH. The result is shown as coincidence rate given for different time bins with a distance of the repetition rate τ. The first bar is the coincidence between the initial idler photon (first pump pulse) and the generated idler photon after one round trip in the loop for the FH or the idler generated with the second pump pulse for the DH. Accordingly, the second bar shows the coincidence with the idler after two round trips (if there was no click after one round trip) or with the idler generated within the third pump pulse, respectively, and so on. We expect that the coincidence rate of the DH is not changing within the measurement since the probability of generating a photon pair is not changing. This is stressed by the horizontal line in the plot. In contrast, we expect a higher coincidence rate for the FH due to the feedback within the setup, where the rates decrease with increasing time between the initial and the next click due to the propagation losses in the feedback loop. Since signal and idler have pair correlations, we expect to see the enhancement in the generation rate in the measured idler photon even if we ignore information about the cycling mode. We expect that the cycling mode transfers the information onto the generated idler photon in every PDC process, leading to higher generation rates in the

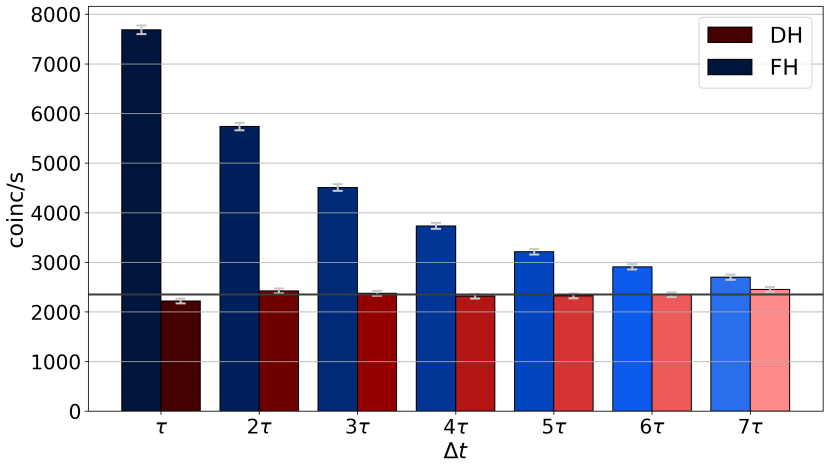

Figure 4.14.: Result of the measurement for the enhancement: The coincidence rates for different time differences Δt for the FH (various shades of blue) and the DH (various shades of red) for a pulse energy of $0.329 \cdot 10^{-11}$J. The gray line shows the mean of the coincidence rates within the DH at 2351.00 coincidences per second.

idler measurement. Inspired by this knowledge about transferred correlations found in this simple measurement scheme, we will investigate these correlations further in Sec. 4.5.

We performed several measurements for different pump pulse energies within this scheme and did two distinct types of analysis with these measurements: individual analysis of the enhancement for different pulse energies and analysis of the system parameters by subsequently optimizing the theoretical model in accordance to the data.

First of all, we start with the individual analysis of the data. The result for a measurement at a pulse energy (measured before the PDC source) of $0.329 \cdot 10^{-11}$J is given in Fig. 4.14 and for a pulse energy of $1.644 \cdot 10^{-11}$J in Fig. 4.15. Further measurements for the intermediate pulse energies of $0.658 \cdot 10^{-11}$J, $0.987 \cdot 10^{-11}$J and 1.315^{-11}J can

Table 4.2.: Coincidence rates for the FH and DH case with the calculated enhancement E at an pulse energy of $0.329 \cdot 10^{-11}$J.

Δt	FH [clicks]	DH [clicks]	E[%]
τ	7685 ± 90	2221 ± 45	246.03 ± 6.19
2τ	5735 ± 75	2425 ± 50	136.54 ± 3.65
3τ	4510 ± 65	2375 ± 50	89.80 ± 2.68
4τ	3735 ± 60	2315 ± 50	61.27 ± 2.07
5τ	3210 ± 55	2324 ± 50	38.22 ± 1.51
6τ	2910 ± 55	2344 ± 50	24.09 ± 1.13
7τ	2700 ± 50	2453 ± 50	10.11 ± 0.67

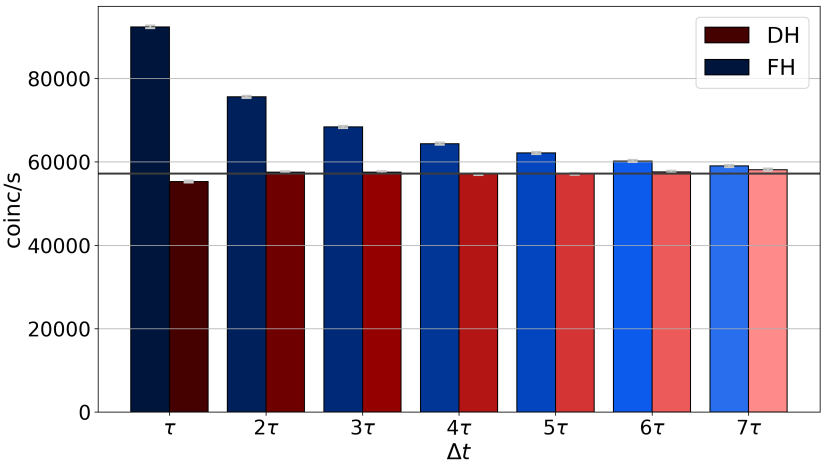

Figure 4.15.: Result of the measurement for the enhancement: The coincidence rates for different time differences Δt for the FH (various shades of blue) and the DH (various shades of red) for an pulse energy of $1.644 \cdot 10^{-11}$J. The gray line shows the mean of the coincidence rates within the DH at 57187.71 coincidences per second.

be found in Appendix D. We show the measured coincidence rates per second for the FH (shades of blue) and for the DH (shades of red) up to the seventh pulse after the initial pulse. As expected, the coincidence rates for the FH are higher than the ones for the DH and decreasing with increasing the time difference between the initial and next detected click for both cases. Furthermore, the coincidence rates for the DH remains almost constant for all time differences as we expect there no change with increasing time difference (see gray horizontal line). The first bar is in both cases a bit lower than the other ones since the detectors are not completely recovered between two consecutive events, even though the dead time of 10 ns is lower than the repetition time of 13.17 ns. This effect decreases the coincidences for FH and DH equally; thus it does not distort the comparison of both coincidences.

Table 4.3.: Coincidence rates for the FH and DH case with the calculated enhancement E at a pulse energy of $1.644 \cdot 10^{-11}$J.

Δt	FH [clicks]	DH [clicks]	E [%]
τ	92400 ± 305	55307 ± 235	67.07 ± 0.45
2τ	75595 ± 275	57541 ± 240	31.38 ± 0.27
3τ	68395 ± 260	57513 ± 240	18.92 ± 0.20
4τ	64380 ± 255	57058 ± 240	12.83 ± 0.16
5τ	62150 ± 250	57137 ± 240	8.77 ± 0.13
6τ	60220 ± 245	57621 ± 240	4.51 ± 0.09
7τ	59015 ± 245	58137 ± 240	1.51 ± 0.05

The exact results for the coincidence rates for all time differences Δt are given in Table 4.2 for the lower pulse energy and in 4.3 for the higher one. The quantifying parameter for showing the quantum feedback of the PDC source is given by the enhancement factor E for each time bin, which gives the relative increase of the coincidence rates cc of the FH compared to the DH by

$$E = \frac{cc_{\mathrm{FH}} - cc_{\mathrm{DH}}}{cc_{\mathrm{DH}}}, \tag{4.29}$$

where the ratio of the difference between the coincidence rates cc of the FH and DH with the coincidence rate of the DH is calculated. The enhancement in coincidence rates decreases with increasing the time difference between the detected clicks, which is expected. Furthermore, we see an increase of approximately 246% for next neighbor clicks for the lower pulse energy and still an increase of 67% for the highest pulse energy. This is a significant increase of the number of clicks achieved after one feedback of a signal. Moreover, we still see an enhancement after seven round trips of approximately 10% for the lowest pulse energy and 1.5% for the highest one, respectively. This, in turn, means that the quantum feedback in general works, and correspondingly, we can expect higher probabilities in the Fock-state generation. Within this measurement, we do not know anything about the generated state in the cycling mode since we do not measure it, but we can conclude that we gain from the feedback.

We have seen that the enhancement is increasing with decreasing pulse energies, which we will analyze in the following. Naively, one would expect that the enhancement increases with increasing pulse energies since the generation probability depends on the mean photon number in the pump pulse, being proportional to the pulse energies. Due to the performed measurement, we will see that it is the opposite way.

For analyzing this behavior, we start with the fundamental methods described in 4.2 making use of the methods to calculate the conditional probabilities to generate two subsequent photons.

We know our output function, given in Eq. (4.13), and their dependence on the intensity gain factor γ and the ideal measurement operators $\hat{\Pi}_0 = \hat{E}(0)$ and $\hat{\Pi}_1 = \hat{E}(1) - \hat{E}(0)$ for no and and one click, respectively. If p_{c_1,c_2} is the joint probability for having a click in the first and second time bin, we can define the conditional probability

$$p_{c_1|c_2} = \frac{p_{c_1,c_2}}{\sum_{c_2'} p_{(c_1,c_2')}}, \tag{4.30}$$

leading to the final form of the conditional probability to have one click under the condition that we had one click before as

$$p_{1|1} = \frac{p_{1,1}}{p_{1,0} + p_{1,1}}. \tag{4.31}$$

Assuming we measure the direct heralding case, then the scheme given in Fig. 4.10, reduces to one PDC source with two vacuum modes as input, where we detect the herald $\hat{E}(z)$ and trace over the second mode $\hat{F}(0,z)$, leading to

$$a(z) = \mathrm{tr}\left(\hat{F}(0,z)\right) = \frac{1}{\gamma - (\gamma-1)z}. \tag{4.32}$$

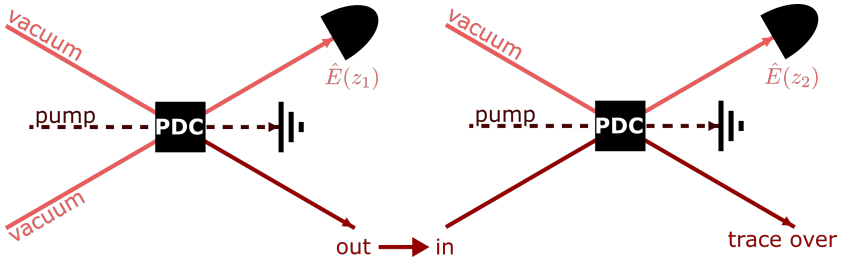

Figure 4.16.: Schematic description of the stimulation measurement for the FH case. For further details, see text.

From this, we can directly extract the probabilities for detecting no click as $p_0 = a(0) = \frac{1}{\gamma}$ and for detecting one click as $p_1 = a(1) - a(0) = 1 - \frac{1}{\gamma}$. Since, the next process is independent from the previous one, we can calculate the joint probabilities by the product of the individual probabilities as

$$\begin{aligned} p_{0,0} &= \frac{1}{\gamma^2} \\ p_{1,0} = p_{0,1} &= \frac{1}{\gamma}\left(1 - \frac{1}{\gamma}\right) \\ p_{1,1} &= \left(1 - \frac{1}{\gamma}\right)^2, \end{aligned} \tag{4.33}$$

leading to the conditional probability of

$$p_{1|1}^{\mathrm{DH}} = 1 - \frac{1}{\gamma}. \tag{4.34}$$

Measuring the FH case, we have to assume the scheme in Fig. 4.10 twice with one output from the first output as the input in the second process, as shown in Fig. 4.16. The first part (left side) is the same as the DH case. Therefore, we know the output of the first PDC process and the input into the second process, respectively. The output after the second process $\hat{F}(x_1, z_1)$ with $x_1 = (\gamma - 1)z_1/\gamma$ can then be calculated by

$$\frac{1}{\gamma}\hat{F}\left(\frac{(\gamma-1)z_1}{\gamma}, z_2\right) = \frac{1}{\gamma^2}\hat{E}\left(\frac{\frac{(\gamma-1)z_1}{\gamma} + (\gamma-1)z_2}{\gamma}\right), \tag{4.35}$$

thus tracing over the output leads to

$$b(z_1, z_2) = \frac{1}{\gamma^2 - (\gamma-1)(z_1 + \gamma z_2)}. \tag{4.36}$$

Therefore, we can calculate the probabilities with $p_{0,0} = b(0,0)$, $p_{1,0} = b(1,0) - b(0,0)$, $p_{0,1} = b(0,1) - b(0,0)$ and $p_{1,1} = b(1,1) - b(0,1) - b(1,0) + b(0,0)$, which leads to the conditional probability of

$$p_{1|1}^{\mathrm{FH}} = 1 - \frac{1}{\gamma(\gamma^2 - \gamma + 1)} \tag{4.37}$$

With this, we can calculate the enhancement dependent on the intensity gain factor of these measurements by

$$E(\gamma) = \frac{p_{1|1}^{\mathrm{FH}} - p_{1|1}^{\mathrm{DH}}}{p_{1|1}^{\mathrm{DH}}} = \frac{\gamma}{\gamma^2 - \gamma + 1}. \tag{4.38}$$

We can analyze from this, the behavior of the enhancement with increasing the squeezing parameter ζ relating to the intensity gain factor as $\gamma{=}\cosh^2|\zeta|$. The squeezing parameter is monotonously increasing with $|\zeta| \geq 0$. Thus, the derivative of the enhancement factor with increasing $|\zeta|$ shows

$$\partial_\gamma E(\gamma) = \frac{-(\gamma^2 - 1)}{(\gamma^2 - \gamma + 1)^2} \leq 0, \tag{4.39}$$

which in turn means, the function is decreasing with increasing pulse energies.

In the next step, we analyze the system parameters, such as loop propagation efficiency as well as the Klychko efficiency for the herald, by matching these in the theoretical model according to the data. We perform this analysis exemplary for the highest pump energy. The simulation of the initial state for DH and FH is given by Eq. (4.25).

In the case of the DH, we detect either one or no click, which is simulated by Eq. (4.15) and accounts for loss by applying Eq. (4.20). After tracing over the signal mode in the DH, we find the expectation value for having one or no click in the detection. Since the single processes of the DH are independent, the joint probability of different click pattern is again the product of the individual probabilities.

The FH simulation is a bit more complicated since we must cascade the state generation and account for loop propagation losses. Thus, for the loop propagation losses in the mode, we use Eq. (4.25) and use it alternating with the generation operator, depending on the number of roundtrips, being dependent on the time difference between the first and next click. The detection between the first and next click are then only accounted for the case of no clicks.

The free parameters are the pumping strength given by γ as defined in Eq. (4.12) with the squeezing parameter being proportional to the pump intensity $|\zeta|$, the overall detection efficiency η_{det}–or more precise the Klychko efficiency–and the loop propagation efficiency being only applied to the FH case. In Fig. 4.17, the experimental achieved enhancement (blue bars) and the corresponding simulation (red crosses) for increasing time difference τ between the first and next click is given. Here, we estimate the free parameters of our theoretical model from the data. We find the squeezing parameter $|\zeta| = 0.0095 \pm 0.0001$ corresponding to a mean photon number of $\langle n \rangle = 0.118 \pm 0.001$[2] for this pump intensity, the detection efficiency in the herald $\eta_{det} = 0.3891 \pm 0.0003$ and $\eta_{loop} = 0.5872 \pm 0.0001$ for the loop propagation efficiency. We see that the previously measured Klychko efficiency agrees with the estimation whereas the loop propagation efficiency is lower than the previously measured efficiency. The reason for the drop could

[2] The mean photon number is calculated by the relation $\langle n \rangle = \sinh^2(|\zeta|)$ for signal and idler separately. Thus, for the overall photon number in the PDC process $\langle n \rangle = 2\sinh^2(|\zeta|)$ holds true.

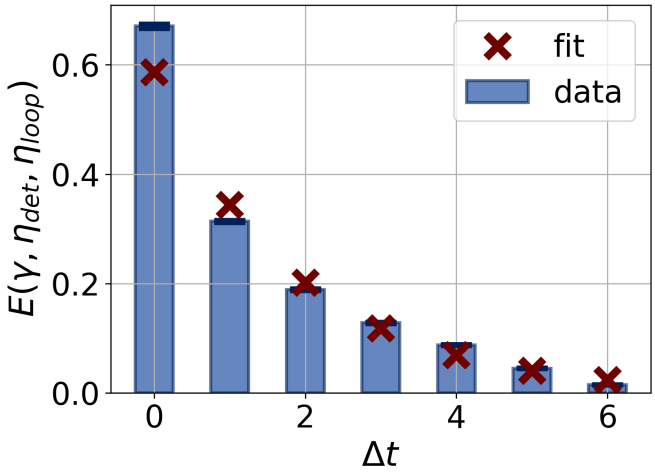

Figure 4.17.: Enhancement for a time difference of Δt between the first and next click in the detection. The experimental data is given as blue bars and the simulation is given by red crosses. For further details, see text.

be found in a slight mismatch of the pump pulses and the cycling mode since the overlap measurement is restricted in its resolution. Furthermore, it could be an overestimate of the efficiency measured with the alignment laser since the alignment laser has a larger beam size compared to the actual cycling mode, it could be that the feedback time of the cycling mode is increased or decreased compared to the laser repetition rate.

4.4 Fock-state generation via feedback in parametric down-conversion

In the previous chapters, we have introduced the Fock state generation and detection via our novel approach. In fact, in this project, we have established a full analysis of this new procedure on the basis of click counting statistics. In this section, we show the results of generating the Fock states within our novel approach (FH) and compare these with the conventional approach (DH). The figures of merit are again a joint analysis of the state fidelity $\mathcal{F}$ and the success probability $\mathcal{P}$ as well as the nonclassicality of the generated state. The data acquisition is developed and optimized for the used configuration of the setup, including a precise switching of the EOMs and the given detection schemes (see Fig. 4.1). Based on the two district approaches of the FH and DH, we first will introduce the measurement schemes and present the data we acquire within the measurements in Sec. 4.4.1. Consequently, we depict the analysis scripts, derived from the introduced theory framework in Sec. 4.2, with respect to the previously explained acquired data sets in Sec. 4.4.2. Finally, we will show the experimental results of the Fock-state generation (Sec. 4.4.3).

We divide the results into three main parts each with a different focus. The first part contains the analysis of the data for DH and FH with the desired heralding in the FH, defined as exactly one click in each time bin of the herald. Secondly, we analyze

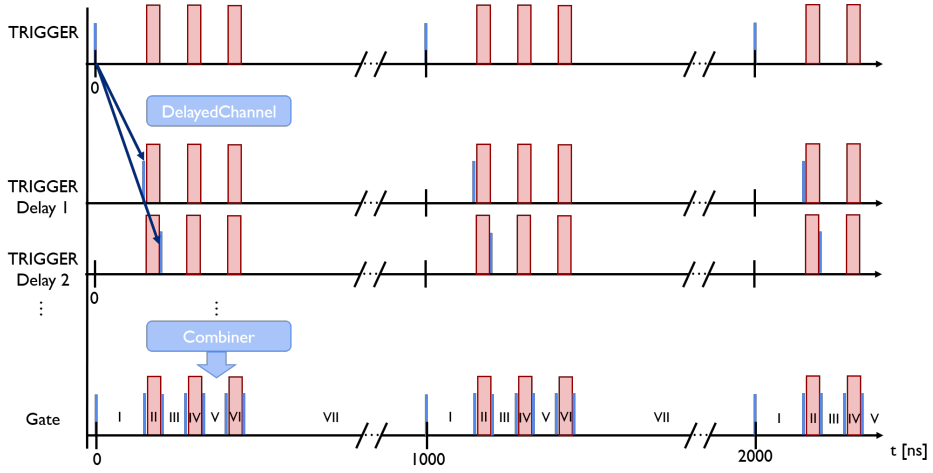

Figure 4.18.: Illustration of the `get-gate` function, adapted from [143].

the Fock-state generation of the DH as a part of the FH measurement with exactly n photons in the first of the n time bins of the herald to account for similar losses in DH and FH. Finally, we will analyze the higher-order contributions of the Fock-state generation within DH and FH. Eventually, we will show a data set for the two-photon Fock state generated after a further optimization within the setup.

4.4.1 Data acquisition and processing

We introduce two main requirements for the measurement of the Fock states generated within FH and DH schemes: the time-tagger used for the measurements and the measurement script.

In general, a time-tagger is a time-to-digital converter, here converting the signal of the detectors into a electrical signal. The used time-tagger from *Swabian Instruments*, allows for time-correlated single-photon counting to read out clicks in a certain detector, coincidence clicks between two detectors and, for example, histograms with a start and a stop channel. Furthermore, they provide a Python library, which facilitates easy interfacing and convenient integration into our excising infrastructure and thus, making it accessible for direct data acquisition. For initializing the time-tagger within a script, one needs to set two values for every channel of the time-tagger: the dead time of the detector, which is in our case 10 ns and 60 ns, as well as the trigger level, which is 0.1 V.

The functions needed for the measurement of the Fock states are the `Count Between Markers` function and the `Synchronized Measurements` function provided by *Swabian Instruments*. In addition, we use the `get-gate` and the `ck-mat` function developed within our group [143]. In the following, a more detailed description of these functions and their implementation into our analysis is provided.

The `get-gate` generates a gate signal for marking the position of the time bins in which the clicks of the herald and the state generation are located. This function was

already introduced within our group for the analysis of a quasi-photon-number-resolved measurement within multiplexing detection schemes [143]. In Fig. 4.18, we have illustrated the `get-gate` function, with the functions output marking the time bins we want to read out during our measurements. The knowledge of the exact positions of these time bins in relation to the trigger signal enables us to delay the trigger signal to a point at the beginning of the time bin and at the end of this time bin (see middle plot in Fig. 4.18). The function called `Delayed Channel`[3] creates a virtual channel delayed by a the known delay between trigger and the actual time bin. The script creates two virtual channels for every time bin we want to measure. For example, in Fig. 4.18, we have three time bins leading to six virtual channels. Every gate is then combined via the `Combiner`[3] function so that we have a overall gate for every detector. In general, the overall gate then contains $(2n+1)$ separated areas (see labels in the lower plot), such that we can distinguish between the required time bins containing information about the clicks in herald and the state and the not needed ones.

In our case, we have in total six detectors in use, four for the heralding, which is due to the spatial multiplexing, and two for the Fock-state detection. The number of time bins needed in the Fock-state detection are four for both detectors leading to a resolution of up to eight photons. However, the number of time bins in the herald depend on the state we aim to generate since the number of pump pulses is directly connected to the number of time bins in the herald (number of pump pulses is equal to the number of heralds). This means that this function is restricted in its efficiency leading to an increased measurement time with every added time bin in the herald.

The collection of the number of clicks in each time bin is performed by the `Count Between Markers` function. This function counts the clicks between the "start" and "stop" signal given by the `get-gate` function and records the data into a one-dimensional array of the length $(2n+1)m$ corresponding to the number of separated areas and the number of overall trigger signals m. As soon as a start signal is detected, the counter starts to accumulate the data in this certain area and is reset to zero when the next start/stop signal is detected.

In general, we have to synchronize the data accumulation of the herald and the Fock-state detection. The `Synchronized Measurements`[3] function ensures for this synchronized measurements. Every channel in the time-tagger is registered by `register Measurement`[3] and the measurement is started simultaneously.

The collected data for every channel is in a form of an one dimensional array with all the information of the number of clicks per time bin. In the first step for the data processing, we remove time bins, in which no information for our system is given. Having a look at Fig. 4.18 the time bins of interest would be the second, the fourth and sixth area. For the state detection, we want to gain the information of the total number of clicks in a single measurement with $n \in \{0, \ldots, 8\}$. Thus, we sum over the clicks in all required time bins. The heralding is treated differently. Since we want to have the number of clicks in every bin separately, we sum over the number of clicks in for

[3]provided by *Swabian Instruments*

Heralding pattern

No. of clicks in Fock state

	(0,0)	(0,1)	(0,2)	(0,3)	(0,4)	(1,0)	(1,1)	…
0	80282601	1590208	44073	861	5	1778256	67875	···
1	1128542	429217	23731	609	7	292917	29151	···
2	19234	15911	3541	177	2	9237	3330	···
3	246	325	144	18	0	195	119	···
4	4	8	5	1	0	2	4	···
…	…	…	…	…	…	…	…	…

Figure 4.19.: Final form of data for the two-photon Fock state after the measurement, here reduced to only a part of the table with exemplary numbers from a measurement. For further details see text.

a certain bin in all four heralding channels. Thus, we have $(N+1)^t$ possible options for the heralding pattern with N possible clicks. Here we have the possibility of zero to four clicks leading to $N+1=5$, with t pump pulses varying from one to four. In general, heralding pattern means the combination of clicks per time bin. For example, a heralding with one click in three time bins lead to a $(1,1,1)$ heralding pattern.

The final data is then rearranged into a table form, with the columns belonging to the heralding pattern and the rows give the number of the signal clicks for each heralding pattern. A reduced example for the two-photon Fock state data within the FH is given in Fig. 4.19 in which one can find sample data from an actual measurement. The labeling of the heralding pattern (x,y) is defined by the number of clicks in the first time bin (x) and in the second time bin (y) resulting from the first and second PDC process, respectively. The number given in each field is the amount of single measurements, where the given conditions, such as x clicks in the first herald time bin, y clicks in the second time bin, and n clicks in the signal, are fulfilled. We already found that the amount of single measurements fulfilling a given condition is decreasing with increasing the number of clicks. In general, the number of columns is increasing exponentially with increasing the number of PDC processes or more precise with the desired number of photons generated within the FH. For a target state $|n\rangle$ the cycling light is coupled out after $n-1$ complete round trips for the FH case. Hence, the configuration differs for each measurement and therefore, we need three different measurements to detect these states, one for each photon number. The data for the DH is a table in form of a 5×9 array since we have only one time bin in the heralding. The DH data contains the information about the two-, three- and four-photon Fock state.

Here, one experiment for the FH is defined by n pump pulses, n heralding time bins, $n-1$ round trips and one Fock-state measurement. Each experiment is repeated with a rate of 1 MHz, being defined by one initial trigger event. The overall measurement for one n-photon Fock-state generation is defined by the number of blocks with every block containing 100k single experiments. The data acquisition time is increasing with increasing photon number due to the post processing. The measurement time of one

block for the two-photon Fock-state generation within the DH is 0.896 s, and for the FH, it increases to 1.324 s. Furthermore, measuring one block for generating a three-photon state needs 1.324 s and for a four-photon state 2.060 s. In order to achieve reasonable statistics, we take at least 30k blocks for every data point. Thus, the measurement time for one data point is approximately 7.5 hours for the DH and approximately 11.04, 13.10 and 17.20 hours for the two-, three- and four-photon Fock state generated within the FH. In general, this measurements require a long-time stability which we were able to achieve.

4.4.2 Data analysis

The data analysis of the Fock-state generation experiment is mainly performed with only single columns of the overall taken data. We will need the entire table, specifically the correlations between columns, for the correlation analysis in Sec. 4.5.

For characterizing the generation quantity and state quality, we analyze the success probability $\mathcal{P}$, the fidelity $\mathcal{F}$ with the target state and the nonclassicality $\mathcal{N}$ of the generated state.

The success probability of the desired state indicates the quantity of successful events. In general, the success probability is given by the ratio of the number of events with the desired heralding pattern to the overall number of events in the measurement run. We can express this as

$$\mathcal{P} = \frac{\sum_k c_k}{\sum_{k_1,k_2} c_{k_1,k_2}}, \tag{4.40}$$

with c_k denoting the click-counting statistics of the desired click pattern and c_{k_1,k_2} as the overall click-counting statistics of the measurement. The sum over this gives the total number of experiments in the measurement.

The fidelity is obtained through the Bhattacharyya coefficient [144] calculating the similarity of the click statistics of the desired heralding with the target state. Hence, we can calculate the fidelity as

$$\mathcal{F} = \sum_{k=0}^{N} \sqrt{c_k^{(\mathrm{sim})}}\sqrt{c_k}, \tag{4.41}$$

with the measured data c_k and the click-counting distribution $c_k^{(\mathrm{sim})}$ for the target state. Here, we can perform two different analyses: calculating the fidelity with the target state detected by lossless detection, and the fidelity with the theoretical model of the system corrected for detection losses.

We start with the ideal case assuming to generate a perfect n-photon Fock state and to detect the state within lossless time multiplexed detection. The resulting click-counting statistics as introduced in Ref. [145]

$$c_k^{(n)} = \langle n|\hat{\Pi}_k|n\rangle = \binom{N}{k}\frac{k!}{N^n}\left\{{n \atop k}\right\} \tag{4.42}$$

is then serving as a target state for calculating the fidelity ($c_k^{(\mathrm{sim})}$). The Stirling number of the second kind is defined as

$$\left\{ {n \atop k} \right\} = \frac{1}{k!} \sum_{j=0}^{k} \binom{k}{j} (-1)^{k-j} j^n. \tag{4.43}$$

The second method we can use is modeling the system with the theory framework we have introduced in Sec. 4.2 and correcting for the detection losses. We optimize the theoretical model in accordance to the resulting data for every state by adapting the detection efficiency for the herald η_H, the detection efficiency for the state η_{state}, the loop propagation efficiency η_{loop} and the squeezing parameter $|\zeta|$ as free parameters in the model. The theoretical model for the DH is not accounting for the loop efficiency, because no loop propagation takes place.

In general, the state generation is given by Eq. (4.25) and the loop propagation is given by Eq. (4.21). The measurement operator is defined by Eq. (4.16), whereas Eq. (4.20) accounts for the detection loss. Due to the final structure of the data set, we have to bring the theoretical model into the same shape, leading to the definition of two measurement operators, one for the herald with each time bin containing from zero to four clicks and one for the state detection containing from zero to eight clicks. The DH is generated only with one pump pulse, meaning that we directly generate the state with Eq. (4.25). In contrast, for the FH, we have to alternate the state generation and the loop propagation loss several times for the feedback. The free parameters in the theoretical model are then optimized to match the data, enabling us to estimate the squeezing $|\zeta|$ for every data point. Furthermore, we obtain a good approximation of the detection efficiency in the herald η_H and Fock state detection η_{state}, as well as for the loop efficiency η_{loop}. Since we only want to correct the measurement for the detection efficiencies, we assume for the theoretical model no loop propagation losses. This modeling results into the click counting statistic $c_k^{(\mathrm{sim})}$ for calculating the state fidelity.

The nonclassicality $\mathcal{N}$ of the generated state is calculated via the method described in Sec. 3.3. Again, we use the events in the column of our table with the desired heralding pattern and calculate the matrix of moments M of this click-counting statistics. The smallest eigenvalue and the associated eigenvector $\vec{v}$ are then used to calculate the nonclassicality given as

$$\mathcal{N} = \vec{v}^{\dagger} M \vec{v} \tag{4.44}$$

with an uncertainty given by $\sigma\mathcal{N} = \sqrt{|\vec{v^{\dagger}}^2 |\Delta M^2| \vec{v}^2|}$ with the matrix of uncertainties ΔM. The statistical significance of the calculated nonclassicality is then given as ratio $\mathcal{N}/\sigma\mathcal{N}$.

4.4.3 Feedback heralding vs. direct heralding

In this section, we present the data and analysis for the Fock-state generation within our setup and compare these data with the conventional approach of DH. The overall analysis will be subdivided into three parts with every part focusing the fidelity, success probability and nonclassicality. First, we compare the states generated within the FH and the DH, where DH refers to the generation with one pump pulse and where we herald on n photons. In contrast to the first results we show, we try to account also for similar losses in FH and DH. Thus, the second performed comparison is done with a DH-like generation within the FH measurement, that is the heralding on n photons in one time bin of the FH. The DH data is then taken from the table resulting from the FH measurement. This will be further discussed later. Finally, we show a analysis of the higher-order photon numbers generated within the FH and compare it to the DH. In addition, we present the measurement of a two-photon Fock state, generated with a more optimized setup.

We start with the analysis of the success probability and the fidelity of the Fock state generated within FH (n pump pulses) with a heralding of one photon in each time bin and generated within DH (one pump pulse) with the heralding on n photons. In Fig. 4.20, the success probability (left) and fidelity (right) for the generated two- (upper plots), three- (middle plots) and four-photon (lower plots) Fock states is shown. We perform the analysis for the FH (blue) and the DH (red) for squeezing parameters $|\zeta|$ between 0.1 and 0.3, depending on the pulse energies per pulse. In Table 4.4, all values for pulse energies per pulse and the corresponding squeezing parameter are given. In general, the squeezing parameter is proportional to the product of the pump intensity, the coupling strengths and the interaction time of the pump within the crystal. Likewise, we can calculate the squeezing $s = -10\log_{10}(e^{-2|\zeta|}) = 20\log_{10}(e) \times |\zeta|$, corresponding to 1.0 dB to 2.6 dB squeezing in our experiment. Furthermore, we can calculate the mean photon number per PDC process as $\langle n \rangle = 2\sinh^2(|\zeta|)$, corresponding to a mean photon number from 0.027 to 0.190. The values are calculated via matching of the free parameters in the theoretical model to the actual data. In general, the data points for each state are measured at similar squeezing parameters.

The actual values for the fidelity and success probability can be found in Appendix E.

Table 4.4.: Squeezing parameters $|\zeta|$ for the realized number of pump pulses t depending on the pulse energies per pulse used for the measurement.

$t=1$		$t=2$		$t=3$		$t=4$	
E[nJ]	$\|\zeta\|$	E[nJ]	$\|\zeta\|$	E[nJ]	$\|\zeta\|$	E[nJ]	$\|\zeta\|$
		0.125	0.1172	0.165	0.1491		
0.285	0.1730	0.250	0.1670	0.365	0.1961	0.235	0.1670
0.570	0.2543	0.500	0.2326	0.500	0.2440	0.465	0.2326
0.850	0.2975	0.78	0.3038	0.790	0.2980	0.730	0.3038

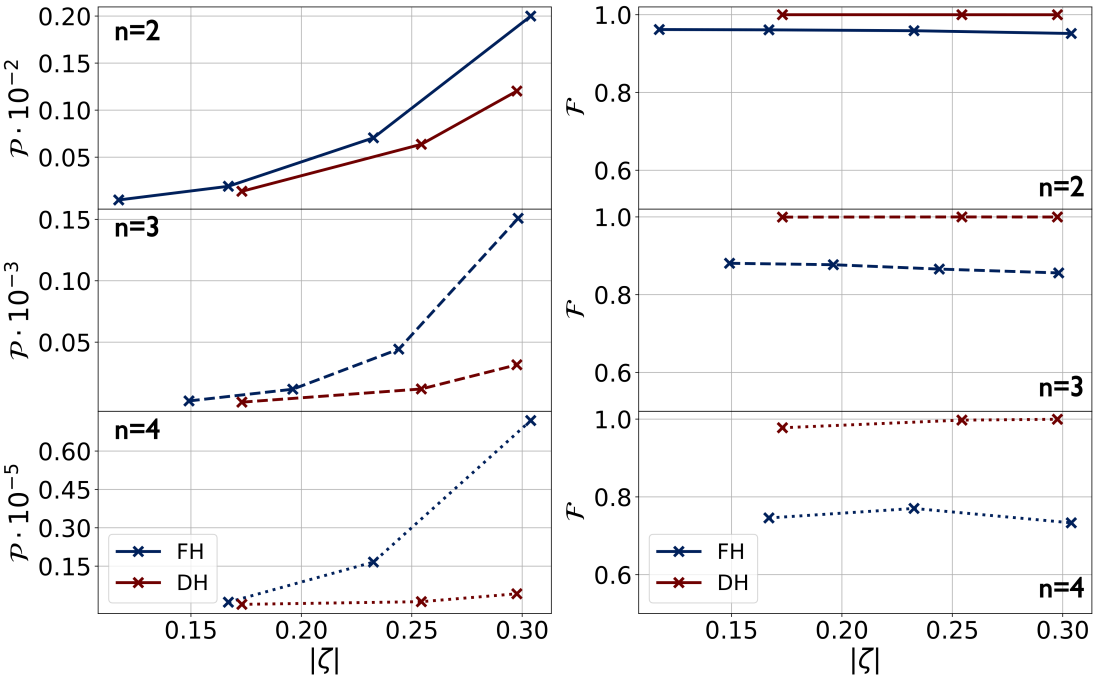

Figure 4.20.: Success probability $\mathcal{P}$(left) and Fidelity $\mathcal{F}$ (right) for the generated two- (upper plots), three- (middle plots) and the four-photon (lower plots) Fock state. The analysis is performed for FH (blue) and for DH (red) for squeezing values $|\zeta|$ between 0.1 and 0.3.

Here, the $c_k^{(\mathrm{sim})}$ in Eq. (4.41) for calculating the state fidelity accounts only for detection losses in herald and state detection and not for the loop propagation losses. This is done since the loop propagation affects mainly the state generation, whereas the detection losses are not determining the state. The detection efficiency for the herald is $\eta_H = 0.36$ and for the state detection is $\eta_{state} = 0.38$. The higher efficiency in the signal detection is caused by the higher efficient detectors used for the state detection (see Sec. 4.1.2).

We see that the success probability increases for smaller photon numbers n and also for higher pulse energies, likewise the squeezing parameter $|\zeta|$, since the photon pairs are produced with a higher rate. The success probability is decreasing almost equidistantly for decreasing n since the generation rate scales approximately with the number of photons. In general, for all photon numbers n, the success probability is higher for the FH compared to the DH. Especially, the difference between FH and DH increases for increasing the photon number n leading to the assumption that this effect will be even stronger if we generate even higher photon numbers. The success probability for generating a two-photon state is 60% higher in the FH case compared to the DH case. Further, this increases to a 17-fold higher $\mathcal{P}$ for a four-photon Fock state generated within FH compared to the DH case.

In contrast to the behavior of FH and DH with respect to the success probability, the

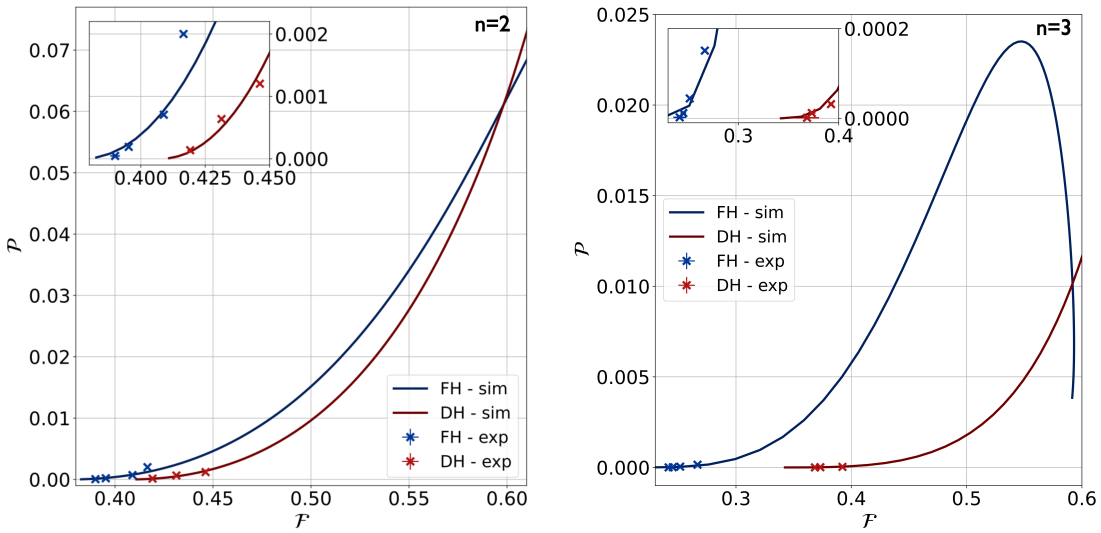

Figure 4.21.: Joint analysis of the success probability $\mathcal{P}$ and fidelity $\mathcal{F}$ for a two-photon Fock state (left) and a three-photon Fock state (right). We show the experimental data for the FH (light blue crosses) and for the DH (light red crosses) and further the simulation of the systems (FH in blue, DH in red) with the actual system parameters. The insets show a zoom into the area of the experimental data.

fidelity of the DH stays above the state fidelity of the FH. Generally, the fidelities stay almost constant for varying squeezing parameters $|\zeta|$. Moreover, the fidelities for the DH stay close to 99% while it decreases for the FH with increasing photon number n. The main limiting factor for the fidelity is the loop propagation efficiency since it determines the state purity. Still, the fidelity of the two-photon Fock state generated within the FH stays above 95% and even for the four-photon Fock state, the fidelity is approximately 74%. Thus, we have to find a trade-off between fidelity and success probability to have reasonable measurement times with high fidelities.

For finding that trade-off, we analyze $\mathcal{F}$ and $\mathcal{P}$ jointly so that we see the direct connection between the state quality and generation probability, similar to the analysis in Sec. 3.2.1. In this analysis, we do not account for any losses in the state fidelity since we want an analysis of the states without free parameters in the fidelity calculation. Hence, the $c_k^{(\mathrm{sim})}$ in Eq. (4.41) is given by the ideal detection as we model it via Eq. (4.42), similar to the analysis we performed in Fig. 4.11. The joint analysis for a two-photon Fock state (left) and the three-photon Fock state (right) are presented in Fig. 4.21. The experimental data for the FH (light blue crosses) and for the DH (light red crosses) are depicted together with the theoretical model of the system (FH as blue lines; DH as red lines) adapted with the actual system parameters; that are the detection efficiencies and the loop propagation efficiency. The fidelity of the model is also calculated for ideal detection expanding the range of the squeezing parameter $|\zeta|$ we cover with the exper-

imental data. Thus, we see the behavior of success probability and fidelity for higher $|\zeta|$. Within the insets, we show the overlap of the experimental data and the theoretical model. As above the detection efficiencies are given as $\eta_H = 0.36$ and $\eta_{state} = 0.38$, the loop propagation efficiency for the two-photon Fock state is $\eta_{loop} = 0.605$ and slightly lower for the three-photon state with $\eta_{loop} = 0.55$.

We can see that for both photon numbers, the FH performs better in the sense of success probabilities. Especially, if we want to generate a state with a certain fidelity, the success probability of the FH is higher compared to the DH. For example, if we aim to generate a two-photon Fock state with a fidelity of $\mathcal{F} = 0.5$, the success probability is approximately 1.5 times higher for the FH compared to the DH. This enhancement is varying with different fidelities. Moreover, the squeezing needed for the FH to reach this fidelity and success probability is $s_{FH} = 4.683\,\mathrm{dB}$ and increases to $s_{DH} = 5.107\,\mathrm{dB}$ for the DH. This values corresponds to a mean photon numbers of $\langle n\rangle_{FH} = 0.639$ and $\langle n\rangle_{DH} = 0.587$. This squeezing is already in a regime which is experimentally hard to achieve. Even the cross-over point, where FH and DH have the same success probabilities and fidelities, are at a squeezing above 7 dB. This squeezing is even harder to achieve with current experiments. Thus, in our experiment we can increase the success probability at same state fidelities already at a reasonable squeezing.

We see a similar behavior of the joint analysis in the three-photon case. Again, assuming we aim to generate a three-photon state with a fidelity of $\mathcal{F} = 0.5$ as it is the lower limit for achieving quantum light, we see a 10-times higher success probability. The squeezing for generating a three-photon Fock state with this fidelity is then given as $s_{FH} = 7.365\,\mathrm{dB}$ and $s_{DH} = 5.993\,\mathrm{dB}$. The mean photon numbers within the PDC process would then be $\langle n\rangle_{FH} = 1.81$ and $\langle n\rangle_{DH} = 1.11$. Here, the needed squeezing for the DH is lower than the FH because of exponential increase of loop losses with number of round trips (η_{loop}^n) resulting in higher power demand, but both values still are in a regime difficult to achieve experimentally.

We can conclude from this analysis that the FH in general outperforms the DH, especially in terms of the success probability for the same desired fidelities.

Table 4.5.: Nonclassicality $\mathcal{N}$ and its statistical significance (rightmost column) for FH indicated by one click in each time bin of the herald and for DH with n photons in the heralding generated for highest pulse energies with a squeezing parameter $|\zeta| \approx 0.3$.

Heralding pattern	n	t	$\mathcal{N} \times 10^{-4}$	$\lvert\mathcal{N}\rvert/\sigma(\mathcal{N})$
(2)	2	1	-13.515 ± 0.009	141
(1, 1)	2	2	-9.054 ± 0.004	183
(3)	3	1	-18.251 ± 0.104	17
(1, 1, 1)	3	3	-5.334 ± 0.022	24
(4)	4	1	-25.372 ± 13.032	2
(1, 1, 1, 1)	4	4	-5.187 ± 0.103	5

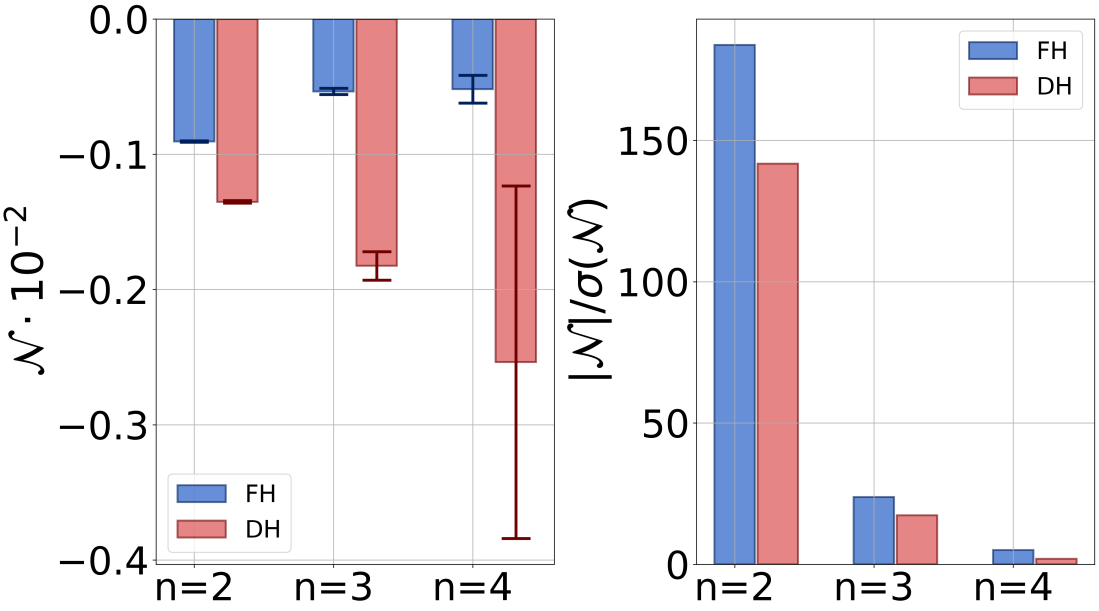

Figure 4.22.: Nonclassicality $\mathcal{N}$ (left) and significance $|\mathcal{N}|/\sigma(\mathcal{N})$ (right) of the two-, three- and four-photon Fock state generated within the FH (blue) and DH (red) generated for highest pulse energies with a squeezing parameter $|\zeta| \approx 0.3$.

Next, we analyze the nonclassical behavior or more precise the amount of nonclassicality of the generated states. In Fig. 4.22, the nonclassicality $\mathcal{N}$ and the corresponding significance $|\mathcal{N}|/\sigma(\mathcal{N})$ of the generated two-, three- and four-photon Fock states for FH (blue) and DH (red) at a given squeezing parameter $|\zeta| \approx 0.3$ are depicted. The values for every state generation differ, thus the actual squeezing values are given in Table 4.4 (lowest row). Additionally, $\mathcal{N}$ and $|\mathcal{N}|/\sigma(\mathcal{N})$ are given in Table 4.5 for this certain squeezing parameter for the different heralding patterns within the DH (n photons in the herald) and within FH (one photon in n heralding time bins). Furthermore, the number of pump pulses t is given for this generated state, as well as the desired photon number n.

The method for calculating the nonclassicality was already introduced in Sec. 3.3 and due to the eight-bin resolution in the state detection, we are able to employ moments up to the eighth order. We see that both FH and DH certify the violation of the constraints given in Eq. (4.28). Thus, the generated states within DH and FH show nonclassical properties. Note that, though the definition of the nonclassicality gives us negative values for $\mathcal{N}$, we will refer to its absolute value when comparing values for $\mathcal{N}$ for different data sets. Consequently, a lower negative value of $\mathcal{N}$ indicates a higher nonclassicality of the state. In general, according to the analysis performed in Sec. 4.2 (especially see Fig. 4.12), we expect the nonclassicality to increase for increasing photon number. In contrast to the FH case, we see the expected behavior of the nonclassicality only of the

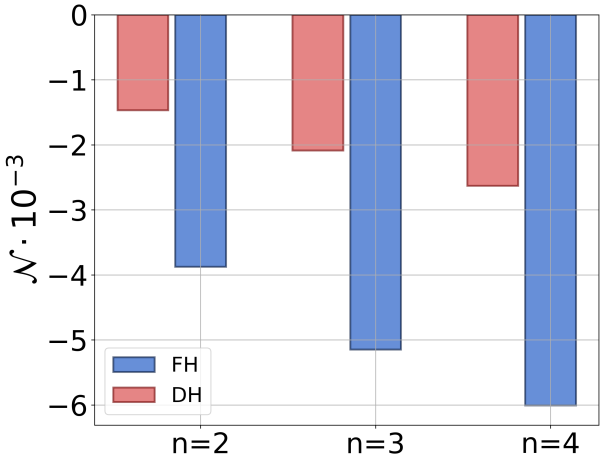

Figure 4.23.: Nonclassicality $\mathcal{N}$ of the simulated two-, three- and four-photon Fock state within the FH (blue) and DH (red) for highest pulse energies with a squeezing parameter $|\zeta| \approx 0.3$.

states generated within the DH. Still, the statistical significance of the nonclassicality, that is the reliability of this value, is higher for the FH. The decreasing significance with increasing photon number is due to the decreasing generation rate for higher photons. The reason for the decreasing behavior of the FH case is given by the summed loop propagation losses being more pronounced with every round trip the cycling mode travels through.

As a proof that the amount of nonclassicality of states generated within the FH depends on the loop propagation losses, we perform a analysis of $\mathcal{N}$ without the influence of the loop propagation loss. This is done by making use of the theoretical model with the given detection efficiencies in herald and state detection but without accounting for the loop propagation loss in the FH. The result of this analysis can be found in Fig. 4.23. With this, we see the expected behavior of the nonclassicality increasing with the photon number n also for the FH case. Moreover, $\mathcal{N}$ is higher for state generated within FH compared to the DH. This result confirms the influence of the loop propagation losses on the cycling mode and its impact on the generated state. Moreover, we see a direct connection between the roundtrip number and the suppressed nonclassicality since it leads to a inverse progression compared to the expectations.

As a proof of concept and to exclude errors in the measurement and analysis, we have calculated the nonclassicality of the vacuum component in all the measurements (defined by its pump pulses t), which can be found in Fig. 4.24. We expect that vacuum is not violating Eq. (4.28), since it is a classical state, and that it ought to have a nonclassicality of zero. The nonclassicality of the vacuum state for all numbers of pump pulses t is in the range of 10^{-12}, leading to the result of $\mathcal{N} \approx 0$.

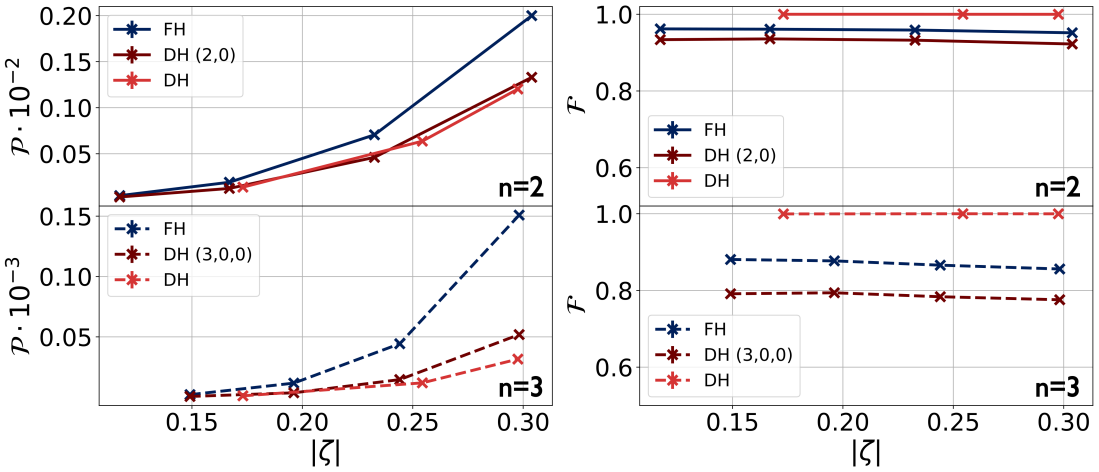

Figure 4.25.: Success probability $\mathcal{P}$(left) and Fidelity $\mathcal{F}$ (right) for the two- and three-photon Fock state generation. The analysis is performed for FH (blue), for DH (light red) and for the DH generated within the FH measurement (heralding patterns $(2,0)$ and $(3,0,0)$) for squeezing values $|\zeta|$ between 0.1 and 0.3.

Additionally, the nonclassicality of the vacuum component is nine orders of magnitude smaller than the generated states within FH and DH, proving again that it shows no nonclassical behavior. This indicates that our measurements do not exhibit major problems in the data acquisition or in the analysis. Thus, our nonclassicality analysis is performing as expected and does not lead to fake-negativities which occur with methods other than our click counting method.

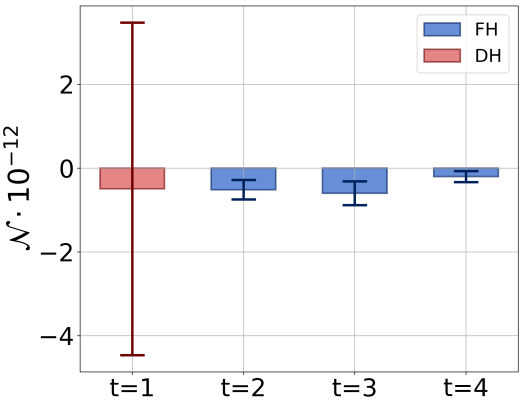

Figure 4.24.: Nonclassicality of vacuum within the FH (blue) and DH (red).

In the following, we will analyze the state generation within the DH while accounting for identical loop propagation losses as in the FH. We achieve this by extracting the DH case from the data detected with the FH, resulting in a heralding pattern of $(2,0)$ for the two-photon Fock-state generation and $(3,0,0)$ for the three-photon state. Thus, the generated state is traveling once through the loop. In general, we extract this additional DH data from the FH measurements by picking a certain column in the table (such as shown in Fig. 4.19) with the given conditions of two (three) clicks in the first heralding time bin and none in

the following. For the two-photon case, we have two additional DH-like cases with two photons in the first or two in the second time bin, increasing to three additional cases for three photons. We expect the success probability of both DH cases staying below the FH since we have no quantum feedback in the $(2,0)$- and $(3,0,0)$-DH cases. Additionally, if the loop propagation loss is the main limiting factor for the state fidelity, we expect $\mathcal{F}$ for the $(2,0)$- and $(3,0,0)$-DH cases to stay below the original DH case. Again, this is due to the lack of quantum feedback and the additional loss in the generation process.

In Fig. 4.25, we present the analysis of the success probabilities $\mathcal{P}$ (left) and the fidelities $\mathcal{F}$ of the two- and three-photon Fock state as we have seen before (FH- blue, DH - red) with the additional information about the DH case extracted from the FH measurements (dark red curves). We find that the FH case exceeds both DH cases in success probability and fidelity. As expected, the DH cases extracted from the FH measurement are mainly effected by the loop propagation losses, the fidelity of these drops below the FH. Thus, this is proving the limitations given by the loop propagation efficiency η_{loop}. Furthermore, we find that the success probability of the three-photon Fock-state generation is higher for the $(3,0,0)$-DH case compared to the original DH case. We expect this behavior since there are with a given probability photons seeding the process and being not measured in the heralding due to the losses in the system. Moreover, we can conclude, that the quantum feedback is compensating partially for the loop propagation losses leading to a higher fidelity of the FH compared to the DH-like cases.

We can have a further look into the nonclassical behavior of the generated state within the $(2,0)$- and $(3,0,0)$- and $(4,0,0,0)$-DH state generation being depicted in Fig. 4.26. Due to the impact of the loop propagation losses, the states generated by the DH extracted from the FH measurement show a decreasing nonclassicality being even more suppressed compared to the FH. The four-photon Fock state generated with the $(4,0,0,0)$-DH even shows no statistical significance (0.5 standard derivations). In general, this strengthens the fact that the loop efficiency is the main limiting factor in the FH system and that the FH is superior to the DH in comparable circumstances.

In addition to the analysis we have discussed so far, we are able to generate, for example, three-photon Fock states within two-pump pulses and to generate states with $n > 4$. Through the type of measurements we perform, especially regarding the resolution of the heralding, we are able to generate arbitrary photon numbers with $n \in \{0,\dots,8\}$. We are able to generate exponentially more photons via FH $n \leq (N)^t$ with N multiplexed heralding detectors (in our current configuration $N = 4$) and t passes through the source. Here, DH is constrained to $t = 1$, while we have data for the FH up to $t = 4$, which can be further increased.

We start with the generation of $n > t$ photons within FH and compare it to the previous analysis. Within the FH data with two heralding bins, that is two pump pulses, we are able to generate three-photon Fock states with the heralding pattern $(2,1)$ and $(1,2)$ as well as with three clicks in one time bin. Since the $(0,3)$- and $(3,0)$-case

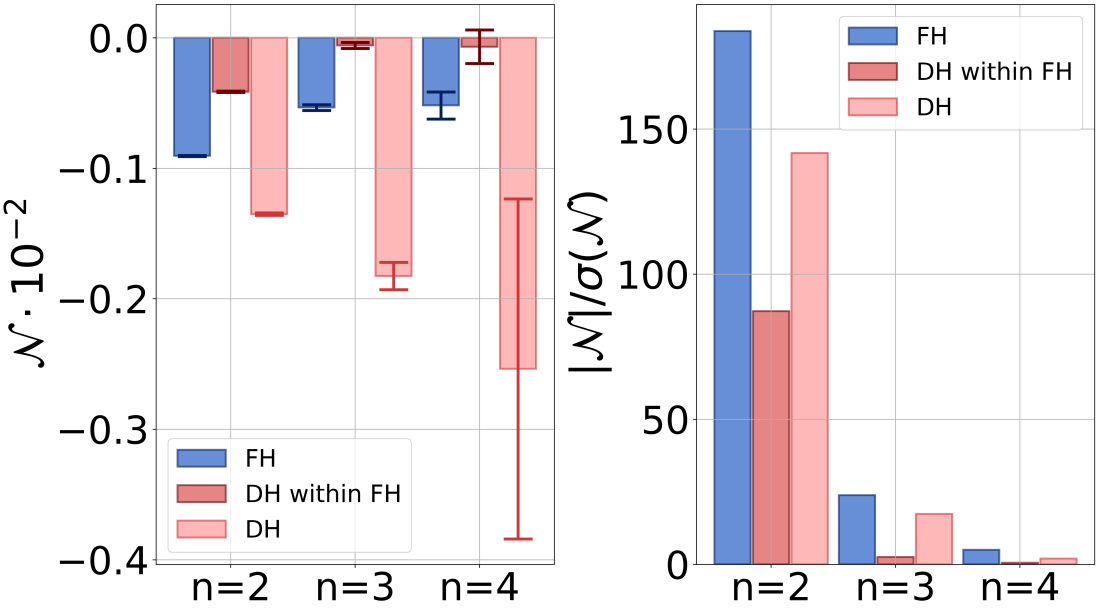

Figure 4.26.: Nonclassicality (left) and significance (right) of the two-, three- and four photon Fock state generated within the FH (blue), DH measured within the FH (red) and the DH (light red) generated for highest pulse energies with a squeezing parameter $|\zeta| \approx 0.3$.

correspond to the DH case without any seeding, we will not investigate them further. In Fig. 4.27, we compare the success probability and fidelity of the three-photon Fock state, generated within DH (red) and FH (heralding pattern $(1,1,1)$, solid light blue), with the generation within the FH with the heralding pattern $(2,1)$ (dashed, blue) and $(1,2)$ (dashed, dark blue). Thus, we compare measurements with three to two pump pulses. We find that both additional generation pattern stay in between the FH and DH case for both the success probability $\mathcal{N}$ (left) and the fidelity $\mathcal{F}$ (right).

The success probability for both cases stays above the DH, showing clearly a feedback

Table 4.6.: Nonclassicality $\mathcal{N}$ and its statistical significance (rightmost column) for generating $n = 3$ photons within different heralding pattern of the FH and for DH with n photons in the heralding generated for highest pulse energies with a squeezing parameter $|\zeta| \approx 0.3$.

Heralding pattern	n	t	$\mathcal{N} \times 10^{-4}$	$\lvert\mathcal{N}\rvert/\sigma(\mathcal{N})$
(3)	3	1	-18.251 ± 0.104	17
$(1,1,1)$	3	3	-5.334 ± 0.022	24
$(1,2)$	3	2	-13.903 ± 0.041	33
$(2,1)$	3	2	-10.169 ± 0.036	28

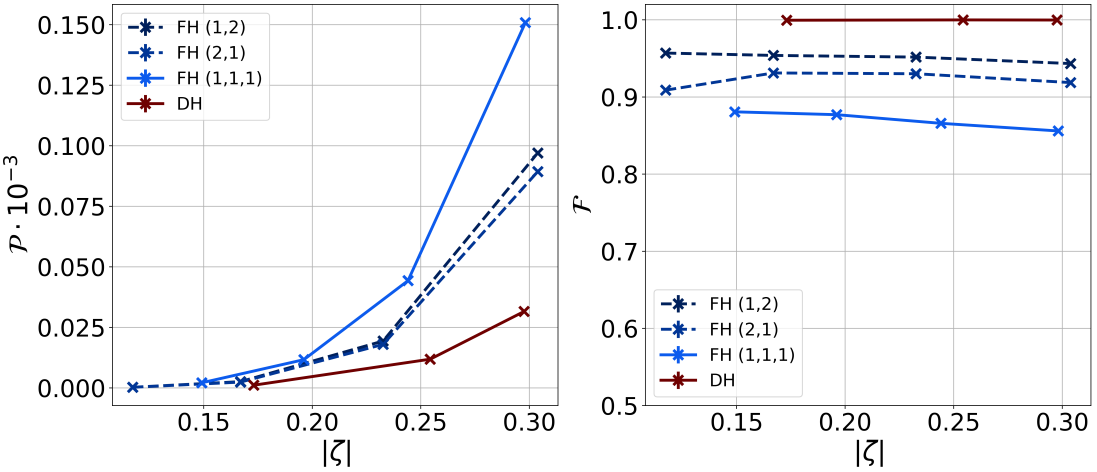

Figure 4.27.: Success probability $\mathcal{P}$ (left) and Fidelity $\mathcal{F}$ (right) for the three-photon Fock state generation. We analyze in addition to the DH (red) and the standard heralding pattern $(1,1,1)$ (light blue) within the FH additional three-photon data from the FH generated with two pump pulses, namely $(1,2)$ (dashed, dark blue) and $(2,1)$ (dashed, blue). The data is given for squeezing values $|\zeta|$ between 0.1 and 0.3.

of the initial photons (either one or two) in the second PDC process. Actually, they do not reach the success probability of the FH with $(1,1,1)$ desired for the three-photon Fock state since they only contain one feedback process instead of two. The reason for the slight difference between both additional cases is given by the different generation of either one or two photons in the first time bin leading to a change in the feedback and the amount of loop propagation loss. The fidelity of both stay below the DH case, but due to only single propagation through the feedback, instead of double propagation, they stay above the $(1,1,1)$-FH case. The fidelity of the $(1,2)$-FH case is higher compared to the other FH cases, since the higher photon number is not effected by the loop loss as much as the $(2,1)$ case and again, the cycling mode is only traveling through the loop once.

In Table 4.6, we find the nonclassicalities of the additional heralding pattern to generate a three-photon Fock state. The nonclassicality of these heralding pattern is still below the DH. At the same time, the statistical significance is again higher. The $(1,2)$ case indicates the highest nonclassicality for $n = 3$ generated within the FH. This result is expected since we have already seen that the nonclassicality is mainly limited by the loop propagation efficiency. Thus, if the higher photon number is generated in the last time bin, the generated state is less effected by the loop.

We can further generate four-photon Fock states within the case of two and three heralding bins. We analyze for the two-bin heralding three possible pattern to generate four photons, namely $(2,2)$, $(3,1)$ and $(1,3)$. Here, the most interesting heralding is the

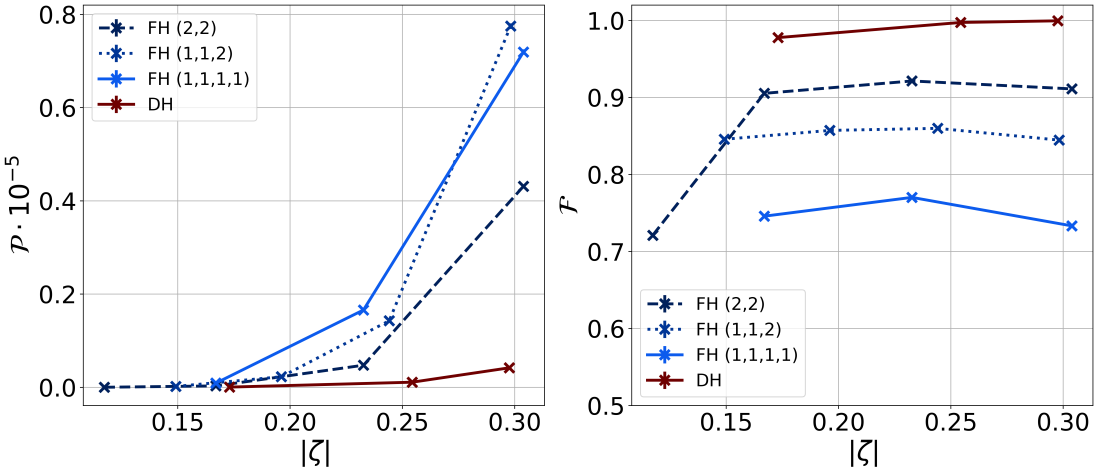

Figure 4.28.: Success probability $\mathcal{P}$(left) and Fidelity $\mathcal{F}$ (right) for the four-photon Fock state generation. We analyze in addition to the DH (red) and the standard heralding pattern $(1,1,1,1)$ (light blue) within the FH additional four-photon data from the FH generated with two and and three pump pulses, namely $(2,2)$ (dashed, dark blue) and $(1,2,1)$ (dotted, blue). The data is given for squeezing values $|\zeta|$ between 0.1 and 0.3.

$(2,2)$ click pattern since we expect for the other cases a similar behavior as we have seen before. Furthermore, for the three-bin heralding, we find also three heralding pattern $(1,1,2)$, $(1,2,1)$ and $(2,1,1)$, expecting the first one to perform best in the sense of fidelities. In all these cases we can investigate the effects of the quantum feedback. In Fig. 4.28, the fidelity and success probability for the four-photon Fock state generation is presented. For reasons of comparison, we show again the data for the DH (red) and

Table 4.7.: Nonclassicality $\mathcal{N}$ and its statistical significance (rightmost column) for generating $n = 4$ photons within different heralding pattern of the FH and for DH with n photons in the heralding generated for highest pulse energies with a squeezing parameter $|\zeta| \approx 0.3$.

Heralding pattern	n	t	$\mathcal{N} \times 10^{-4}$	$\lvert\mathcal{N}\rvert/\sigma(\mathcal{N})$
(4)	4	1	-25.372 ± 13.032	2
$(1,1,1,1)$	4	4	-5.187 ± 0.103	5
$(2,2)$	4	2	-13.179 ± 2.521	5
$(1,3)$	4	2	-17.555 ± 3.424	5
$(1,3)$	4	2	-7.716 ± 3.079	2
$(2,1,1)$	4	3	-4.546 ± 0.128	3
$(1,2,1)$	4	3	-5.082 ± 0.135	4
$(1,1,2)$	4	3	-5.863 ± 0.162	4

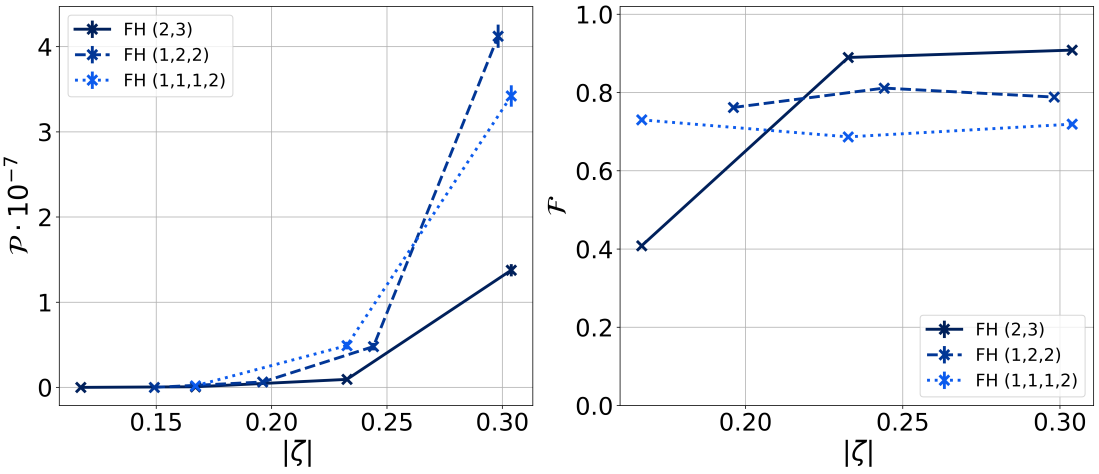

Figure 4.29.: Success probability $\mathcal{P}$(left) and fidelity $\mathcal{F}$ (right) for the five-photon Fock state generation. We analyze the generation within the two- to four-bin heralding resulting into different pattern. The data is given for squeezing values $|\zeta|$ between 0.1 and 0.3.

the initially for four photons desired FH-case ($(1,1,1,1)$, solid light blue) together with the $(2,2)$-FH (dashed, dark blue) and the $(1,1,2)$-FH (dotted, blue).

Similar to the case of three-photon generation, we find the additional generation patterns $(1,1,2)$ and $(2,2)$ in between the FH and DH for $\mathcal{P}$ and $\mathcal{N}$. The $(1,1,2)$-case is even outperforming the usual FH case in terms of success probabilities for the highest squeezing value. This could be explained by the very low generation rates of four photon pairs one after the other, even for high squeezing values, whereas it is more likely for this squeezing to generate four photons in three PDC processes. The fidelity of the two-bin generation $(2,2)$ is higher compared to the three- and four-bin generation due to the fact that it was less affected by the loop losses. The nonclassicalities can be found in Table 4.7 showing again lower $\mathcal{N}$ for all FH cases compared to the DH. In general, the statistical significance is higher compared to the DH.

In general, we can already conclude that, even with other heralding pattern, the FH outperforms the DH generation in terms of success probability whereas the fidelity and the nonclassicality are still limited by the loop propagation losses.

Additionally to the shown analysis, we are able to generate Fock states with $n > 4$ within the current configuration of the FH. In contrast, no DH with four single-photon detectors is capable of producing this higher photon-number state. We will show this generation exemplary for $n = 5$ since for even higher photon numbers, the number of successive events is quite low. By increasing the measurement time, we expect to see even more successive events allowing for a analysis of this data. In Fig. 4.29, the analysis of success probability and fidelity of the five-photon Fock state is depicted. Even if the

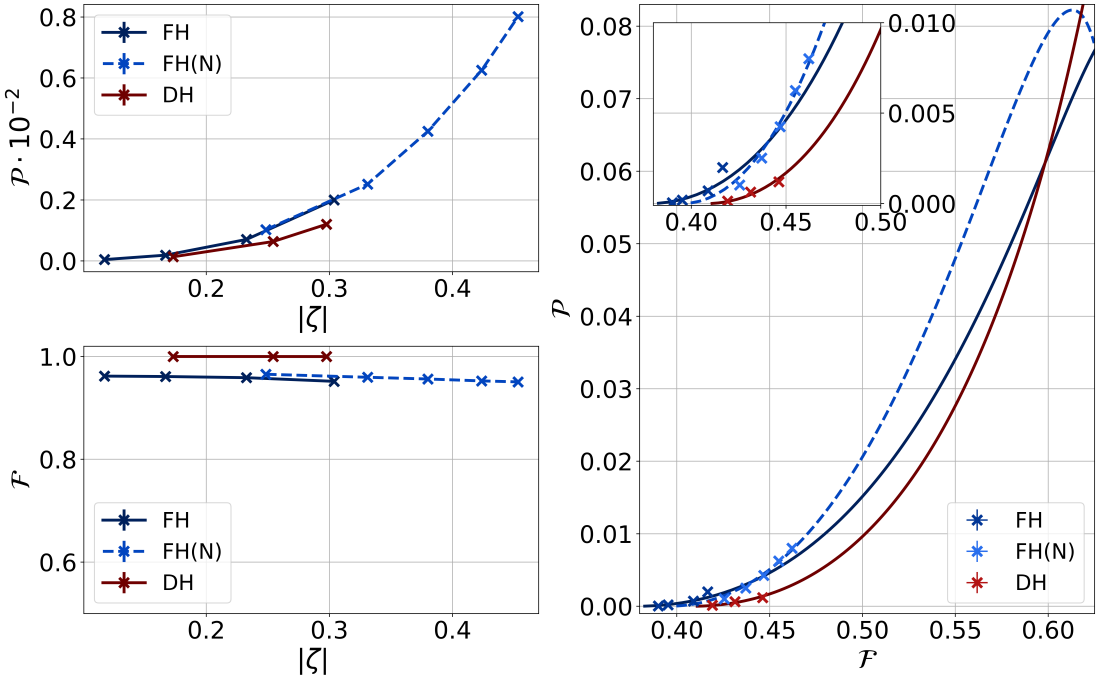

Figure 4.30.: Success probability $\mathcal{P}$(left) and fidelity $\mathcal{F}$ (right) for the two-photon Fock state generation. We show the data for the FH (blue) and DH (red) and compare it to a new data set with higher efficiencies FH(N) (dashed, blue). The data for DH and FH is given for squeezing values $|\zeta|$ between 0.1 and 0.3 whereas the range is increased to $|\zeta| = 0.453$ corresponding to a squeezing $s = 3.93$, a pulse energy of $E = 0.665\,\mathrm{nJ}$ and a mean photon number of $\langle n \rangle = 0.43$ for the additional data set.

number of successive events is already quite low, we find that the success probability is higher than 10^{-7} for the highest squeezing parameter. Thus, since one data-point for a certain state usually containing 3 billion single measurements, we still find more than 300 successive events for this certain click patterns.

The fidelity of the three cases stay almost constant. We find that the $(2, 3)$ case shows the highest fidelity with $\mathcal{F} > 0.9$, except for one data point. This is, once again, caused by the lower effect of the loop propagation losses on states generated with a lower number of round trips. Still, the fidelity of the state generated within the $(1, 1, 1, 2)$ FH stays above 0.7.

Consequently, the FH outperforms the DH not only in terms of success probabilities, but also allows for a flexible approach for even higher-order photon numbers $n > 4$. In principle, the FH enables the generation of arbitrary photon-number states being only limited by the loop propagation losses.

With further effort in optimizing the system we were able to increase efficiencies in the system, especially the maximal pump energies leading to higher squeezing parameters, as well as the detection efficiencies. These achievements are accompanied by a lot of effort in optimizing many components in the setup. However, as the optimization reached its final stage, some components prevented us from going beyond the data discussed here. Thus, we had only the chance to take a data set for the two-photon Fock state generation with these higher efficiencies. The fidelity and success probability, as well as the joint analysis, can be found in Fig. 4.30. In addition to the previous analysis of the FH (blue) and the DH (red), we present the new FH data (dashed, blue). As before, we show the individual analysis of the success probability (left, up) and fidelity (left, bottom) and the joint analysis of both without accounting for any losses in the state fidelity. Due to the increase of the in-coupling efficiency of the pump pulses into the source, we were able to increase the squeezing parameter to $|\zeta| = 0.453$, corresponding to a squeezing $s = 3.93\,\mathrm{dB}$. Thus, we are now able to cover a larger squeezing range. The dependence of the success probability $\mathcal{P}$ as a function of the squeezing parameter is now more apparent. It seems that $\mathcal{P}$ is increasing quadratic with increasing the squeezing whereas the fidelity is still constant for higher squeezing parameters. Estimating the success probability for the DH, the gap between the success probabilities of both systems will presumably increase further. Hence, we see also a strong dependence between the success probability and the feedback, making the gap in between FH and DH larger for higher squeezing parameters.

Having now a closer look into the joint analysis of $\mathcal{P}$ and $\mathcal{F}$, we find again that the curve for the new FH data (FH(N)) is still significantly above the DH in terms of success probabilities. Nevertheless, one has to mention that the DH data are still the measurements with the less efficient configuration. Assuming, as before, that we aim to generate states with a fidelity $\mathcal{F} = 0.5$, we find for the new FH data an increase of the success probability by a factor of 1.3 compared to the FH data. Thus, within the new configuration, we have a 2.1-fold higher success probability compared to the DH. As mentioned, this enhancement is varying for different fidelities. The cross over point between the new FH data and the DH increases to squeezing values of $s_{FH(N)} = 9.346\,\mathrm{dB}$ and $s_{DH} = 9.050\,\mathrm{dB}$.

In general, with the more efficient configurations in the setup and with optimizing the loop further, we expect that the FH outperforms the DH more strongly in terms of the success probability and that it will even gets closer to the fidelity of the DH. We have already seen in Sec. 4.2 within the joint analysis of fidelity and success probability of the system for the lossless scenario that we are able to outperform the DH even more strongly. If the loop propagation efficiency within the measurement would fit to the measured efficiency in Sec. 4.1.2 with $\eta_{loop} = 0.72$, we expect already a great improvement. Thus, one has to investigate this mismatch of efficiencies in the setup and trying to find a way of measuring the final efficiency on a photon level. Moreover, for loop propagation efficiencies above $\eta_{loop} > 0.90$, we expect fidelities close to the DH.

Since the efficiencies in the setup are mainly determined by the source, that is the through-coupling to the PDC source and the transmission losses, an improvement must be made at the level of the source engineering and design of the setup configuration.

4.5 Feedback-mediated long-range photon-photon correlations

In this section, we will have a closer look at the nonclassical quantum correlations between various idler photons generated within the setup. Previously, we have already seen the increased success probability in the generation of multi-photon Fock states (see Sec. 4.4) and the general enhanced generation in Sec. 4.3. From previous analysis, we gain information about the induction of correlations within the setup. Because of the photon pair correlation of signal and idler, we expect induced correlations between subsequently generated idler photons.

Let us discuss these correlations further by taking a closer look into the data and the measurement we have shown in Sec. 4.3 (especially see Fig. 4.13), in which we have analyzed the general viability of our approach. In these measurements, we have already mentioned that because of the pair correlation, the enhanced generation probability can be measured by detecting the idler photon even if only the signal photon is cycling the loop and fed back into the process. Here, we will further discuss this effect by having a closer look at the correlations between the photons in the system. In Fig. 4.31, we depict the generation process in our system (left) with the corresponding correlations (right) appearing between several photons. Similar to the previous figure in Sec. 4.3, we show the system in spatial multiplexing instead of time multiplexing for sake of simplicity.

Additionally to the measurements, we have already discussed in Sec. 3.1.3 the generation of a two-mode squeezed vacuum state, leading to a pairwise generation of signal and idler within the PDC process. We have seen in Eq. (3.28) that signal and idler exhibit photon-pair correlations within the generation process via applying the squeezing operator onto two-mode vacuum states. This pair correlations can be seen in the generation process as a green line labeled as C_i. In the first generation process, a photon pair (signal s_1 and idler i_1) is generated with photon-pair correlation (green line, C_1). Afterwards, the signal photon seeds another PDC process in which a second photon pair (signal s_2 and ilder i_2) is generated. Whilst the signal photon has still correlations with the first idler photon i_1, a pair correlation with the next generated idler photon i_2 arises because of the quantum feedback. Consequently, both idler photons i_1 and i_2 have pair correlations with the two signal photons s_1 and s_2. Therefore, the seeding of the PDC process by the signal photon mediates the quantum correlation between the idler photons i_1 and i_2 (red line in between marked with C_{ind}). In case of seeding another PDC process, we induce further correlations. Finally, we find quantum correlations between all subsequently generated idler photon in our system. This means that the cycling photon in the feedback system is carrying the information about every idler photon because of the photon-pair correlation. In the following, we will investigate these nonclassical quantum correlations between two and more modes induced within the FH and especially compare them to the DH.

In Sec. 4.5.1, we will briefly introduce the data acquisition and analysis schemes for the correlation measurements. Afterwards, in Sec. 4.5.2, we show the experimental results for this measurement.

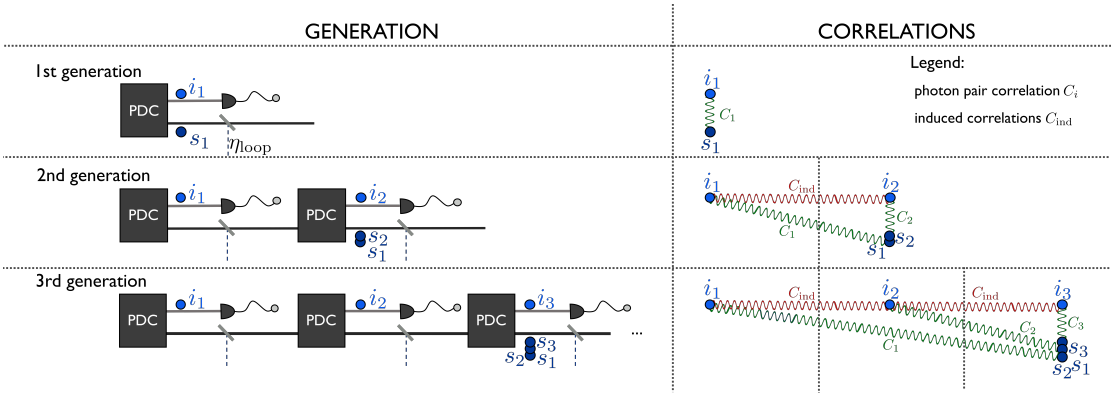

Figure 4.31.: Generation process (left) with the corresponding correlations generated within the system (right). The signal photon is send into several subsequent PDC processes and the idler photon is detected after every process. The signal photon mediates quantum correlations (red lines) between subsequently generated idler photons due to pair correlations (green lines). For a detailed explanation, see text.

4.5.1 Data acquisition and analysis schemes

We have already mentioned that we will use the same data as we use for the Fock state measurements analogously to the table in Fig. 4.19. In general, we want to show the correlation between subsequent heralding time bins for a given photon number in the signal. Therefore, the data we need for this analysis is the information about click statistics for every heralding pattern, that is the probability of having certain heralding pattern with respect to the number of clicks in the signal. In fact, we have already conducted this measurement within the data acquisition for the Fock state generation measurements (see Sec. 4.4.1). For the Fock state measurements, we needed the full information of the click statistics within the signal detection for a certain heralding pattern. In contrast, for the cross-correlations between multiple modes, we need a certain row of the table, that is the click pattern of every heralding pattern for a given number of photons in the signal. This leads to a cross-correlation between the idler modes for generating a given photon number. However, the data for the DH are not the same as for the Fock-state generation since previously we took only information about one single time bin in the herald detection preventing us from determining the correlations between two or more time bins. Thus, we take further datasets for the DH with two and three pump pulses (similar to the FH measurements) with the feedback path being blocked to avoid the seeding. The experimental data for the FH is the same as for the Fock-state generation measurements. Accordingly, we have four data sets each for the FH and DH with two pump pulses entering the source and three data sets with three pump pulses. Furthermore, we have three data sets for the FH with four pump pulses entering the source, but no data for that DH case.

The analysis methods we use for the cross correlation analysis are already introduced in Sec. 3.3. Similar to the analysis of the nonclassicality of the Fock states, we use the matrix of moments M of the overall click-counting statistics. In contrast to the Fock analysis, we need to account for two or more modes in the analysis instead of one mode. Due to the four-bin resolution in every heralding bin, we are able to calculate up to the fourth moment in every time bin, thus leading to a 9×9 matrix of moments for two modes and a 27×27 matrix of moments for three modes (in general, $(N/2+1)^t \times (N/2+1)^t$ matrices for N heralding bins and t passes through the source). For example, the matrix of moments for a single mode is given as

$$M_{A/B} = \begin{pmatrix} 1 & \langle:\hat{\pi}:\rangle & \langle:\hat{\pi}^2:\rangle \\ \langle:\hat{\pi}:\rangle & \langle:\hat{\pi}^2:\rangle & \langle:\hat{\pi}^3:\rangle \\ \langle:\hat{\pi}^2:\rangle & \langle:\hat{\pi}^3:\rangle & \langle:\hat{\pi}^4:\rangle \end{pmatrix}, \tag{4.45}$$

with the individual moments calculated via Eq. (3.56) and for the click counting statistic of the desired photon number. According to this, we can expand the matrix for two modes A and B like

$$M_{A,B} = \begin{pmatrix} 1 & \langle:\hat{\pi}_B:\rangle & \langle:\hat{\pi}_B^2:\rangle & \langle:\hat{\pi}_A:\rangle & \langle:\hat{\pi}_A\hat{\pi}_B:\rangle & \langle:\hat{\pi}_A\hat{\pi}_B^2:\rangle & \langle:\hat{\pi}_A^2:\rangle & \langle:\hat{\pi}_A^2\hat{\pi}_B:\rangle & \langle:\hat{\pi}_A^2\hat{\pi}_B^2:\rangle \\ \langle:\hat{\pi}_B:\rangle & \langle:\hat{\pi}_B^2:\rangle & \langle:\hat{\pi}_B^3:\rangle & \langle:\hat{\pi}_A\hat{\pi}_B:\rangle & \langle:\hat{\pi}_A\hat{\pi}_B^2:\rangle & \langle:\hat{\pi}_A\hat{\pi}_B^3:\rangle & \langle:\hat{\pi}_A^2\hat{\pi}_B:\rangle & \langle:\hat{\pi}_A^2\hat{\pi}_B^2:\rangle & \langle:\hat{\pi}_A^2\hat{\pi}_B^3:\rangle \\ \langle:\hat{\pi}_B^2:\rangle & \langle:\hat{\pi}_B^3:\rangle & \langle:\hat{\pi}_B^4:\rangle & \langle:\hat{\pi}_A\hat{\pi}_B^2:\rangle & \langle:\hat{\pi}_A\hat{\pi}_B^3:\rangle & \langle:\hat{\pi}_A\hat{\pi}_B^4:\rangle & \langle:\hat{\pi}_A^2\hat{\pi}_B^2:\rangle & \langle:\hat{\pi}_A^2\hat{\pi}_B^3:\rangle & \langle:\hat{\pi}_A^2\hat{\pi}_B^4:\rangle \\ \langle:\hat{\pi}_A:\rangle & \langle:\hat{\pi}_A\hat{\pi}_B:\rangle & \langle:\hat{\pi}_A\hat{\pi}_B^2:\rangle & \langle:\hat{\pi}_A^2:\rangle & \langle:\hat{\pi}_A^2\hat{\pi}_B:\rangle & \langle:\hat{\pi}_A^2\hat{\pi}_B^2:\rangle & \langle:\hat{\pi}_A^3:\rangle & \langle:\hat{\pi}_A^3\hat{\pi}_B:\rangle & \langle:\hat{\pi}_A^3\hat{\pi}_B^2:\rangle \\ \langle:\hat{\pi}_A\hat{\pi}_B:\rangle & \langle:\hat{\pi}_A\hat{\pi}_B^2:\rangle & \langle:\hat{\pi}_A\hat{\pi}_B^3:\rangle & \langle:\hat{\pi}_A^2\hat{\pi}_B:\rangle & \langle:\hat{\pi}_A^2\hat{\pi}_B^2:\rangle & \langle:\hat{\pi}_A^2\hat{\pi}_B^3:\rangle & \langle:\hat{\pi}_A^3\hat{\pi}_B:\rangle & \langle:\hat{\pi}_A^3\hat{\pi}_B^2:\rangle & \langle:\hat{\pi}_A^3\hat{\pi}_B^3:\rangle \\ \langle:\hat{\pi}_A\hat{\pi}_B^2:\rangle & \langle:\hat{\pi}_A\hat{\pi}_B^3:\rangle & \langle:\hat{\pi}_A\hat{\pi}_B^4:\rangle & \langle:\hat{\pi}_A^2\hat{\pi}_B^2:\rangle & \langle:\hat{\pi}_A^2\hat{\pi}_B^3:\rangle & \langle:\hat{\pi}_A^2\hat{\pi}_B^4:\rangle & \langle:\hat{\pi}_A^3\hat{\pi}_B^2:\rangle & \langle:\hat{\pi}_A^3\hat{\pi}_B^3:\rangle & \langle:\hat{\pi}_A^3\hat{\pi}_B^4:\rangle \\ \langle:\hat{\pi}_A^2:\rangle & \langle:\hat{\pi}_A^2\hat{\pi}_B:\rangle & \langle:\hat{\pi}_A^2\hat{\pi}_B^2:\rangle & \langle:\hat{\pi}_A^3:\rangle & \langle:\hat{\pi}_A^3\hat{\pi}_B:\rangle & \langle:\hat{\pi}_A^3\hat{\pi}_B^2:\rangle & \langle:\hat{\pi}_A^4:\rangle & \langle:\hat{\pi}_A^4\hat{\pi}_B:\rangle & \langle:\hat{\pi}_A^4\hat{\pi}_B^2:\rangle \\ \langle:\hat{\pi}_A^2\hat{\pi}_B:\rangle & \langle:\hat{\pi}_A^2\hat{\pi}_B^2:\rangle & \langle:\hat{\pi}_A^2\hat{\pi}_B^3:\rangle & \langle:\hat{\pi}_A^3\hat{\pi}_B:\rangle & \langle:\hat{\pi}_A^3\hat{\pi}_B^2:\rangle & \langle:\hat{\pi}_A^3\hat{\pi}_B^3:\rangle & \langle:\hat{\pi}_A^4\hat{\pi}_B:\rangle & \langle:\hat{\pi}_A^4\hat{\pi}_B^2:\rangle & \langle:\hat{\pi}_A^4\hat{\pi}_B^3:\rangle \\ \langle:\hat{\pi}_A^2\hat{\pi}_B^2:\rangle & \langle:\hat{\pi}_A^2\hat{\pi}_B^3:\rangle & \langle:\hat{\pi}_A^2\hat{\pi}_B^4:\rangle & \langle:\hat{\pi}_A^3\hat{\pi}_B^2:\rangle & \langle:\hat{\pi}_A^3\hat{\pi}_B^3:\rangle & \langle:\hat{\pi}_A^3\hat{\pi}_B^4:\rangle & \langle:\hat{\pi}_A^4\hat{\pi}_B^2:\rangle & \langle:\hat{\pi}_A^4\hat{\pi}_B^3:\rangle & \langle:\hat{\pi}_A^4\hat{\pi}_B^4:\rangle \end{pmatrix}. \tag{4.46}$$

The expansion for each mode is proceeded according to the shown matrices.

Previously, we have analyzed the nonclassicality of the generated Fock states and similar to this, we can analyze the cross correlations between the idler modes by calculating the eigenvalue and eigenvectors of the matrix of moments. Thus, the smallest eigenvalue and the corresponding eigenvector $\vec{v}$ lead to a nonclassicality of

$$\mathcal{N} = \vec{v}^\dagger M \vec{v} \tag{4.47}$$

with its uncertainty $\sigma_\mathcal{N} = |\vec{v}^\dagger|\Delta M|\vec{v}|$.

In general, we do not expect any correlation between the individual time bins in the independent sources, as we do not have any feedback of the previously generated photon. Moreover, we expect, that the calculated cross correlation via Eq. (4.47) is mainly determined by the single mode nonclassicality in the second time bin. Accordingly, the value calculated using Eq. (4.47) does not provide the actual correlation between the modes. Thus, we have to define another parameter specifying the multi-mode nonclassicality conditioned to the fact that this is not exclusively determined by the last time

bin. Consequently, we define the parameter of the excess nonclassicality for two-modes as

$$\mathcal{N}(A|B) = \mathcal{N}(A,B) - \mathcal{N}(B), \tag{4.48}$$

with $\mathcal{N}(A,B)$ denoting the two-mode correlation between the first time bin A and the second time bin B and $\mathcal{N}(B)$ as the single mode correlation for the second time bin. The excess nonclassicality for all higher modes is defined accordingly. In contrast to Eq. (4.47), the defined excess nonclassicality fulfills our demand for a figure of merit accounting for the actual correlation between the modes since it removes the amount of nonclassicality exclusively determined by the last time bin.

In general, such multi-mode correlations are very rarely discussed and investigated. Thus, the theoretical description of these effects is not fully developed and moreover, we show the first experimental investigation of these correlations. Some theoretical work in the direction of nonclassicalities in multi-mode systems can be found in Refs. [146–151]. Consequently, the full theoretical description of these is an outstanding problem and has to be investigated further.

4.5.2 Correlation measurement results

In this section, we present the analysis of the multi-mode nonlinear quantum correlations generated within the FH and compare them to the analysis for corresponding parts of the DH case.

We perform different analyses of the excess nonclassicality starting with the proof of our concept via analyzing $\mathcal{N}$ within the vacuum component of our data. Afterwards, we have a look at the individual multi-mode nonclassicalities for the given number of pump pulses and thus, the scalability of the correlations regarding the mode numbers. Furthermore, we analyze the correlation depending on the temporal separation between two modes. At the end, we will show again analysis of the excess nonclassicality of the new FH data and analyze together with the FH data the dependence of the excess nonclassicality on the squeezing parameter. Note again that, though the definition of the excess nonclassicality gives us negative values for $\mathcal{N}$, a lower negative value of $\mathcal{N}$ indicates a higher correlation or nonclassicality of the modes.

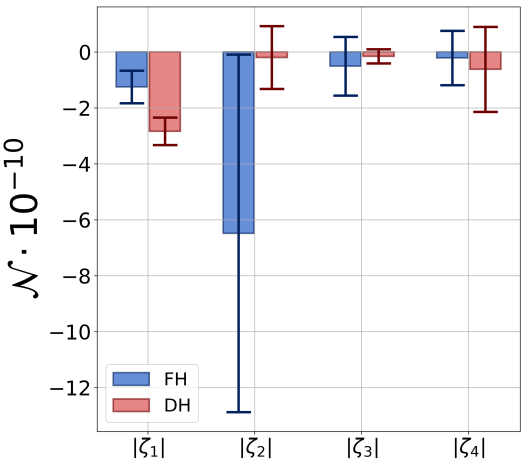

Figure 4.32.: Nonclassicality of vacuum within the FH (blue) and DH (red) with expected value of zero.

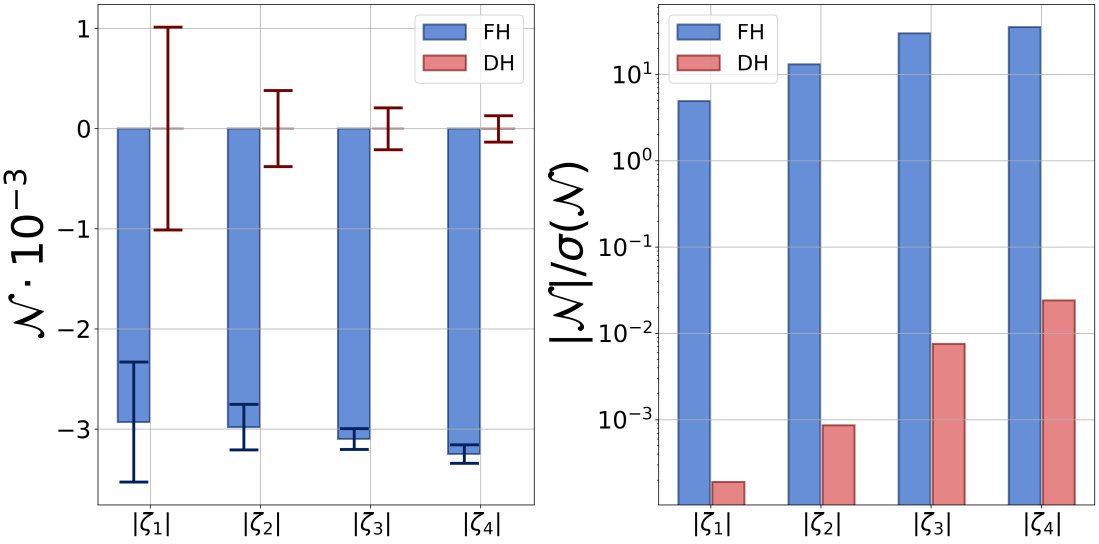

Figure 4.33.: Two-mode excess nonclassicality (left) and significance (right) of the two-bin heralding for FH (blue) and DH (red) for squeezing parameters from $|\zeta_1| = 0.1172$ to $|\zeta_4| = 0.3038$ (see Table 4.4). Note, that the significance is plotted on a logarithmic scale to make the DH visible in the diagram.

As a proof of concept, similar to the analysis we have performed for the Fock state generation, we calculate the nonclassical quantum correlation of the vacuum component, that is no photons in the signal detection. We show this correlation in Fig. 4.32 for all squeezing parameters of the two-bin heralding for FH (blue) and DH (red). The correlations for vacuum component in the three- and four-bin heralding look similar. The squeezing values for these measurements were already given in Table 4.4 with the 1 denoting the smallest and 4 the highest squeezing for this specific number of pump pulses. According to the previous analysis of vacuum components, we expect again that the vacuum component is not violating Eq. (4.28). The nonclassicality of all data sets are in a range of 10^{-10}. It becomes evident that the vacuum component exhibit a vanishing nonclassicality. Comparing this order of magnitude with the results for higher photon numbers, we will discuss hereafter. Therefore, we know that our measurements do not exhibit major problems in the data analysis.

Now, we analyze the excess nonclassicality of the two-mode and three-mode measurements for the desired photon number of $n = 2$ and $n = 3$, respectively. Unfortunately, the statistical significance for the four-mode measurements with $n = 4$ in the signal is very low. Thus, we can not calculate a excess nonclassicality with any significance.

We start with the analysis of the two-bin heralding and the two-mode correlations. The excess nonclassicality $\mathcal{N}$ and the corresponding statistical significance $|\mathcal{N}|/\sigma(\mathcal{N})$ for two photons generated in the signal is depicted in Fig. 4.33 for FH (blue) and DH (red). We give the data for squeezing parameters from $|\zeta_1| = 0.1172$ to $|\zeta_4| = 0.3038$ (see Table

4.4 second column.) Here, the significance of the DH is given in logarithmic scale to make it perceptible. We find that the DH nonclassicality is remaining to a range of $1 \cdot 10^{-5}$ as expected and thus, not showing significant nonclassicalities. In contrast, the FH shows nonclassicalities in the range of $3 \cdot 10^{-3}$ and definitely violates Eq. (4.28). Furthermore, the statistical significance of the FH is increasing with increasing squeezing parameters. Again, this behavior was expected beforehand since the significance is dependent on the number of clicks in the given click-counting statistics increasing with pump energies. The statistical significance of the DH stays close to zero but is also increasing with increasing squeezing parameters. The actual values for the excess nonclassicality $\mathcal{N}(A|B)$ and the corresponding significance of the data can be found in Table 4.33 for all squeezing parameters. In addition, we give the data for the two-mode correlation $\mathcal{N}(A, B)$ and the nonclassicality of the second time bin $\mathcal{N}(B)$.

We can see that the nonclassicality between both modes and the nonclassicality of

Table 4.8.: Two-mode excess nonclassicality $\mathcal{N}(A|B)$ and its statistical significance for the two-bin heralding in FH and DH with the corresponding squeezing parameter ζ for generating $n = 2$ photons in the signal. Furthermore, we give the cross-correlation between the two modes and the nonclassicality of the last mode.

$\lvert\zeta\rvert$		$\mathcal{N}(\mathcal{A}\lvert\mathcal{B}) \cdot 10^{-3}$	$\lvert\mathcal{N}\rvert/\sigma(\mathcal{N})$	$\mathcal{N}(\mathcal{A}, \mathcal{B}) \cdot 10^{-3}$	$\mathcal{N}(\mathcal{B}) \cdot 10^{-3}$
0.1172	FH	-2.930 ± 0.599	4.89	-8.215 ± 0.476	-5.285 ± 0.363
	DH	-0.001 ± 1.012	0.000	-14.270 ± 0.715	-14.270 ± 0.715
0.1670	FH	-2.981 ± 0.228	13.09	-8.209 ± 0.180	-5.228 ± 0.139
	DH	-0.001 ± 0.379	0.000	-13.687 ± 0.268	-13.686 ± 0.268
0.2326	FH	-3.099 ± 0.104	29.87	-7.431 ± 0.082	-4.332 ± 0.063
	DH	-0.002 ± 0.208	0.007	-12.791 ± 0.147	-12.789 ± 0.147
0.3038	FH	-3.249 ± 0.092	35.17	-6.319 ± 0.073	-3.071 ± 0.056
	DH	-0.003 ± 0.132	0.024	-11.473 ± 0.093	-11.470 ± 0.093

Table 4.9.: Three-mode excess nonclassicality $\mathcal{N}(A|B|C)$ and its statistical significance for the three-bin heralding in FH and DH with the corresponding squeezing parameter ζ for generating $n = 3$ photons in the signal. Furthermore, we give the cross-correlation between the three modes and the nonclassicality of the last mode.

$\lvert\zeta\rvert$		$\mathcal{N}(\mathcal{A}\lvert\mathcal{B}\lvert\mathcal{C}) \cdot 10^{-3}$	$\lvert\mathcal{N}\rvert/\sigma(\mathcal{N})$	$\mathcal{N}(\mathcal{A}, \mathcal{B}, \mathcal{C}) \cdot 10^{-3}$	$\mathcal{N}(\mathcal{C}) \cdot 10^{-3}$
0.1961	FH	-5.420 ± 2.303	2.35	-7.493 ± 1.919	-2.073 ± 1.273
	DH	-0.010 ± 6.781	0.000	-17.172 ± 4.812	-17.161 ± 4.778
0.2441	FH	-5.516 ± 1.317	4.19	-6.656 ± 1.135	-1.139 ± 0.669
	DH	-0.015 ± 3.923	0.000	-15.269 ± 2.788	-15.254 ± 2.760
0.2981	FH	-5.030 ± 0.739	6.81	-5.216 ± 0.723	-0.186 ± 0.151
	DH	-0.019 ± 2.108	0.009	-12.221 ± 1.501	-12.201 ± 1.480

the second mode of the DH show approximately the same values. This means that the two-mode nonclassicality $\mathcal{N}(A,B)$ is determined exclusively by the second mode nonclassicality. Thus, this is a sanity check for our excess nonclassicality. Thus, the defined excess nonclassicality $\mathcal{N}(A|B)$ is a reasonable measure for showing the actual cross-correlation between the two modes. In general, the cross-correlation is higher for the DH than for the FH. This can be explained by the additional loop propagation loss in the FH case, similar to the nonclassicality of the Fock states. We make use of all heralding pattern for this two-mode nonclassicality, where some of them are more or less affected by the loop propagation losses. In contrast, the DH is not affected by these losses at all since we have no feedback in the measurements. Moreover, the nonclassicality of the FH is not only determined by the second-bin nonclassicality since $\mathcal{N}(B)$ is lower than $\mathcal{N}(A,B)$ leading to an increased excess nonclassicality.

We can already conclude that the DH is not showing two-mode correlations whereas the FH is clearly showing them. This results reflects exactly our expectations that we induce cross-correlations through feedback.

We will now have a closer look into the three-mode excess nonclassicality, which can be found in Table 4.9 together with the three-mode and single-mode nonclassicality. We find again, that $\mathcal{N}(A|B|C) = \mathcal{N}(A,B,C) - \mathcal{N}(C)$ for the DH is a bit higher compared to the two-mode case, but still only in a range of $1 \cdot 10^{-4}$ and with a statistical significance of almost zero not showing any nonclassicalities. For the FH, $\mathcal{N}(A|B|C)$ is slightly higher compared to the two-mode case, what has been expected since we have one more feedback in the system. Thus, the FH is clearly violating Eq. (4.28). Again, the three-mode and single-mode nonclassicality of the DH is within the same range leading again to the result, that $\mathcal{N}(A,B,C)$ is exclusively determined by the last mode. Furthermore, $\mathcal{N}(A,B,C)$ for the DH is higher compared to the FH being again explained by the loop propagation losses.

Thus, this strengthens the fact that the FH is clearly showing three-mode correlations, whereas DH is not showing them.

In the following, we will have a closer look to the dependence of the excess nonclassicality on the time difference between the two modes for detecting $n = 2$ photons in the signal. The smallest time difference between both modes is τ, which is represented by the two-bin heralding. Thus, the time difference of both modes with 2τ is given by the three-bin heralding conditioned on no click in the middle time bin and 3τ is then given by the four-bin heralding conditioned to no clicks in the two middle time bins.

Before discussing these data, we will briefly have a look back into the previous measurements in Sec. 4.3. We have seen in Fig. 4.17 that the enhancement factor is decreasing with increasing time difference between the two clicks. Due to the measurement, we know that if we find an enhancement in the t-th time bin, one photon was propagating through the feedback $t-1$ times to enhance the generation probability in the PDC process. Therefore, we find that the higher the enhancement is, the more likely we find correlations between the two clicks. This also indicates that the correlation of two modes will decrease with increasing time difference Δt. Otherwise, if we find no

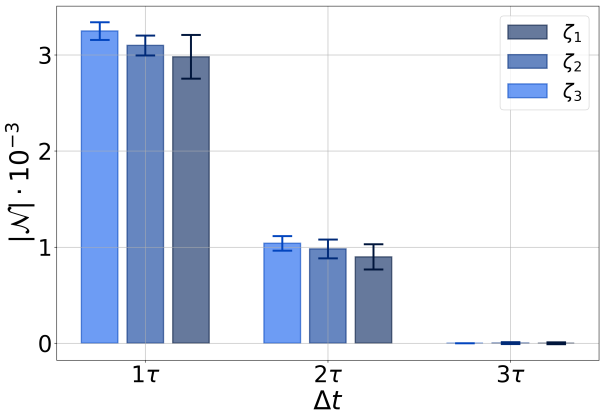

Figure 4.34.: Two-mode excess nonclassicality for increasing time difference Δt between the first and second time bin for squeezing parameters $|\zeta_1| \approx 0.167$, $|\zeta_2| \approx 0.236$ and $|\zeta_3| \approx 0.304$.

enhancement, it is very unlikely that the signal photon was propagating several times trough the feedback. In the previous measurements, we were able to measure up to the seventh bin after the initial pulse due to the measurement scheme. In contrast, for this analysis, we are only able to investigate up to a time difference of 3τ.

In Fig. 4.34, we have drawn the two-mode excess nonclassicality dependent on the time difference Δt for the different squeezing parameters. The squeezing parameters are $|\zeta_1| \approx 0.167$ (dark blue), $|\zeta_2| \approx 0.236$ (blue) and $|\zeta_3| \approx 0.304$ (light blue), whereas the actual parameters for every measurements can be found in Table 4.4. We find that the lowest squeezing parameter shows in total the highest excess nonclassicality and that, as already mentioned, the excess nonclassicality of the four-bin case shows a very low nonclassicality. Since the statistical significance of this measurements is still quite low, we expect that with optimizing the efficiencies and even with longer measurement times the excess nonclassicality shows higher values for the four-bin heralding. In general, the behavior of the nonclassicality with increasing time difference is as we have expected priorly decreasing. Furthermore, one can find a power dependent decay with increasing time difference Δt as we have seen a similar behavior for the measurements in Fig. 4.17.

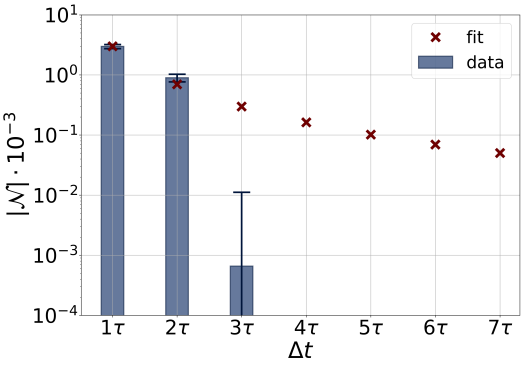

Figure 4.35.: Two-mode excess nonclassicality (log-scale) for a squeezing of $|\zeta| \approx 0.167$.

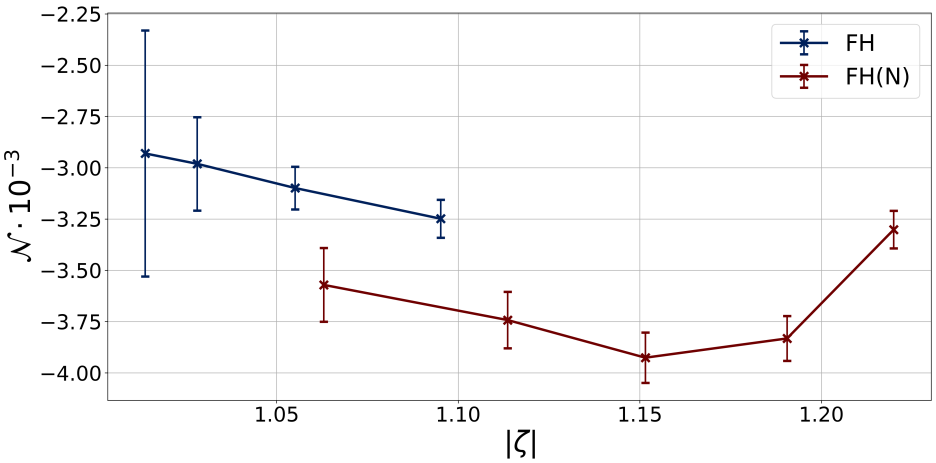

Figure 4.36.: Two-mode excess nonclassicality for the two-bin heralding for the different squeezing parameters for the FH data (blue) and the new FH data set (red).

We want to investigate the decay of the excess nonclassicality for increasing time difference further and have accordingly performed a fit of our three data points to a power function. The weight is decreased for the third data point within the fit since we expect this value to be lower due to its statistics. In Fig. 4.35, the excess nonclassicality (log-scale) for the lowest squeezing parameter with $|\zeta| \approx 0.167$ for the time difference Δt (blue bars) with its fit function $a \cdot x^b$ (red crosses) is depicted. We find for the fit parameters $a = (2.998 \pm 0.128)$ being directly connected to the first data point and as a decay parameter $b = (-2.102 \pm 0.401)$. Due to the lack of data points, we can not completely connect the decay parameter with the already known parameter of the loop propagation loss and detection loss. Nevertheless, we can directly see that the excess nonclassicality shows a power-law dependence and we are able to estimate the excess nonclassicality for higher time differences. In general, one has to further investigate this behavior with a larger number of data points and then compare it to the previous measurements in Sec. 4.3.

Finally, we will have a closer look into the dependence of the excess nonclassicality on the squeezing parameter and analyze the new data set with the more efficient setup configuration. In Fig. 4.36, the two-mode excess nonclassicality for the FH (blue) and the new FH (red) data are depicted for the different squeezing parameters. First, we see that the nonclassicality of the FH data is increasing with increasing squeezing parameter. In contrast, for the new FH data, the nonclassicality is increasing and for the highest squeezing parameter decreasing again. This behavior of decreasing nonclassicality for higher squeezing parameters can be partially explained by the increasing higher photon number contributions and by the excess noise taking into account for these high squeezing parameters.

For further investigating this, we show the excess nonclassicality of the vacuum component in Fig. 4.37. We find that the nonclassicality of the vacuum component is increasing

with increasing squeezing parameter, which typically should not happen. This leads to the fact that the vacuum component for this high squeezing parameters is less occupied for lower photon numbers in the idler time bins. Furthermore, this behavior is also given by the increasing uncertainty for higher squeezing parameters. The higher the squeezing, the more higher photon numbers contribute to the generated states in the signal. Still, the nonclassicality of the vacuum component is three orders of magnitude smaller than the two-photon component. Since we make a conditioned measurement, we would expect that we still have nonclassicalities in our measurements. Moreover, it seems that also other effects play a role in the nonclassicality for very high squeezing parameters, which have to be investigated further.

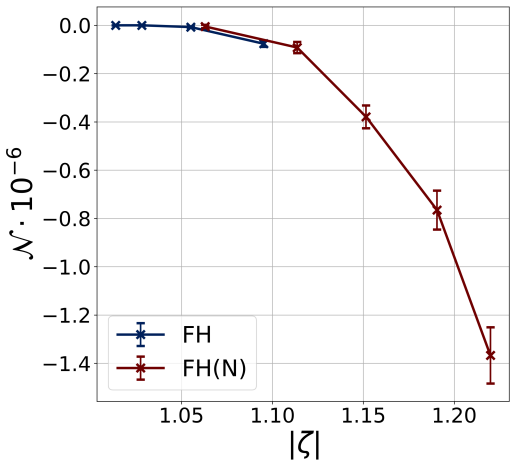

Figure 4.37.: Nonclassicality of vacuum within the FH (blue) and new FH (red).

Thus, we expect the nonclassicality for the two-photon component to continue decreasing for higher squeezing parameters.

Taking one step back to the squeezing dependence of the excess nonclassicality, we see a linear relation between squeezing parameter and nonclassicality for low squeezing values. This behavior is expected since the nonclassicality strongly depends on the measured statistics, where more click-pattern in the idler are occupied, the higher the squeezing.

The actual values of the excess nonclassicality for the new FH data and its statistical significance are given in Table 4.10. We also give the two-mode correlation $\mathcal{N}(A, B)$ and the single-mode correlation $\mathcal{N}(B)$ within the second mode. Comparing these data to the

Table 4.10.: Two-mode excess nonclassicality $\mathcal{N}(A|B)$ and its statistical significance for the two-bin heralding of the new FH data set with the corresponding squeezing parameter ζ for generating $n = 2$ photons in the signal. Furthermore, we give the cross-correlation between the two modes and the nonclassicality of the last mode.

$\lvert\zeta\rvert$	$\mathcal{N}(\mathcal{A}\lvert\mathcal{B}) \cdot 10^{-3}$	$\lvert\mathcal{N}\rvert/\sigma(\mathcal{N})$	$\mathcal{N}(\mathcal{A}, \mathcal{B}) \cdot 10^{-3}$	$\mathcal{N}(\mathcal{B}) \cdot 10^{-3}$
0.2484	-3.571 ± 0.179	19.85	-8.506 ± 0.142	-4.934 ± 0.109
0.3310	-3.742 ± 0.137	27.17	-7.199 ± 0.109	-3.457 ± 0.083
0.3800	-3.926 ± 0.122	32.10	-6.057 ± 0.097	-2.131 ± 0.073
0.4237	-3.832 ± 0.109	35.12	-4.429 ± 0.091	-0.597 ± 0.058
0.4237	-3.301 ± 0.091	36.06	-3.362 ± 0.089	-0.061 ± 0.020

results for the FH given in Table 4.8, we find that the excess nonclassicality is higher for the new data compared to the other data set. As already seen in Fig. 4.36, that even for similar squeezing parameters, the excess nonclassicality is higher, reflecting the increased efficiencies. Interestingly, the two-mode cross-correlation $\mathcal{N}(A,B)$ of the FH data is less strongly decreasing compared to the new FH data. Even both start for their lowest squeezing parameter at a value of $\mathcal{N}(A,B) \approx -8$, the new FH data decrease for the same increase of the squeezing parameter by 5.144. In contrast, the FH data is just decreasing by 1.896. Also, its very interesting that both have a similar cross-correlation for very different squeezing parameters of $|\zeta_{FH}| = 0.1172$ and $|\zeta_{FH(N)}| = 0.2484$, which is somehow unexpected. We find a similar behavior in the single-mode nonclassicality, whereas the value for the lowest squeezing is lower for the new FH, explaining the higher excess nonclassicality.

In general, one should investigate this behavior further, when having data set with the same parameters in the system which covers a larger squeezing range.

We can conclude from this analysis again that we induce correlations between the different modes within the FH. In contrast, no correlations are given for the DH measurements. Furthermore, the two-mode excess nonclassicality is decreasing with increasing time difference between the photons following a power dependence. The nonclassicality is linearly dependent on the squeezing parameter for low squeezing values.

In general, the shown analysis of this long-range photon-photon correlations is preliminary since its the first kind for investigating this nonlinear quantum feedback. Thus a in-depth analysis of these feedback-mediated correlations have yet to be made.

Chapter

5 Conclusion and outlook

The aim of the presented thesis was the implementation of a novel approach for PDC processes to increase generation probabilities for Fock states and to show long-range photon-photon correlations. Finally, we summarize the results of this work and give an outlook for further experiments and applications that are rendered possible in the future because of the new experimental platform and theoretical methods I devised in my PhD project.

5.1 Conclusion

In this thesis, I have depicted a novel way of implementing of implementation of a PDC source that is used as an active element in a feedback-based configuration. The aim was to generate Fock states with higher rates compared to the standard approach of using only one PDC source, i.e. direct heralding (DH), by making use of a feedback of one generated mode. Thus, in the feedback heralding (FH), the generated idler mode serves as a herald and the signal mode is cycled in the feedback to induce seeding in subsequent PDC processes. Consequently, the detection of exactly one photon in n subsequent heralding bins indicates a coherent addition of n photons to the cycling mode. We relate this to a ladder-like climbing of the photon numbers, in which each of the rungs of the Fock-state ladder refers to a round trip and therefore also to the coherent addition of one photon. Moreover, we have discussed the linear and nonlinear properties of our dispersion-engineered PDC source, showing the viability of this source for our purposes. We make use of a waveguided periodically poled KTP source by *AdvR*, allowing a type-II PDC processes that is spatially single mode and decorrelated. The process generates polarization non-degenerate photon pairs at a wavelength of 1542 nm with a conversion efficiency of 1.10%/W. Moreover, the mode overlap of the out- and in-coupled modes, being paramount for the feedback, is quite high with 96.8% for the feedback mode. Thus, due to this special engineering of this source, it is suitable for being implemented into our approach. We have discussed the configuration of the setup in greater detail with the efficiencies as well as all components needed for the generation

and detection of the states. The two critical efficiencies are the loop propagation efficiency given as 72% and the Klychko efficiency given as 39% and 38%, containing the detection and the detection path efficiencies. Finally, it is worth emphasizing that my results are only possible because of the unique properties of the engineered source.

We have introduced a theoretical framework for our approach based on the experimentally easier and accessible click, rather than photon, statistics. Within that framework, we have devised an input-output relation $\hat{E}(x) \rightarrow \hat{F}(x, z)$ for modeling our approach. Furthermore, we have established a formalism for modeling losses, multiplexed detection schemes and conditional detection. In general, the figures of merit are the success probability $\mathcal{P}$, the state fidelity $\mathcal{F}$ and the nonclassicality of the state $\mathcal{N}$. We could show for the ideal system, i.e. the system without any loop propagation losses or losses within the detection, that the FH is clearly outperforming the DH in terms of the success probability for same fidelities. The nonclassicality is depicted to increase even for the DH and FH with increasing the photon number n.

The first basic measurement for showing the viability of our approach was performed via a correlation measurement within the idler detection. To this end, we have continuously pumped the PDC source at 76 MHz and the cycling mode was continuously cycling in the feedback loop. We took the correlation measurement within the FH and the DH for the clicks in the idler detection so that we find the coincidence clicks between single clicks. We compared the coincidence clicks in the FH and DH, in which we find enhanced coincidence rates due to the feedback in the FH. We could show an enhancement by a factor of 246% for the first time bin after the initial pulse for the lowest measured pulse energies and for the highest one an enhancement of 67%. Moreover, we were able to present a enhanced generation up to the seventh time bin after the initial pulse with a enhancement factor of more than 10% for the lowest pulse energy. With our theory framework, we were able to demonstrate the experimental behavior that the enhancement decreases with increasing pulse energies. Finally, we modeled our framework to the decreasing enhancement factor with increasing time difference of the two photons, finding the experimental Klychko efficiency of $(38.91 \pm 0.03)\%$ in the idler mode and the loop efficiency of $(58.72 \pm 0.01)\%$. Thus, we could conclude from this straightforward measurement that the feedback approach is increasing generation probabilities even though we did not measure the cycling mode itself. Moreover, this already showed the induced correlations between independently generated idler photons due to the photon-pair correlation between signal and idler photons.

Afterwards, we showed the experimental results of generating Fock states within the FH and compared them to the DH. Firstly, we have presented that we have a 60% higher success probability of the two-photon Fock state generated within the FH compared to the DH case. Furthermore, this enhanced success probability is even more pronounced with increasing photon numbers. For a three-photon Fock state, the FH has a 5-fold higher success probability and for a four-photon Fock state, we find a 17-fold higher $\mathcal{P}$. At the same time, the fidelity for FH is lower compared to DH and even decreasing

with increasing photon numbers. Thus, we find that the fidelity is determined by the loop propagation efficiency and thus, even more effective for higher photon numbers. For investigating the trade-off between the success probability and the fidelity, we have performed an joint analysis of these quantities, including the calculation of the fidelity as a comparison to the ideal system. We found that for same fidelities, the FH is still outperforming the DH. By assuming a fidelity of $\mathcal{F} = 0.5$, we found an enhanced success probability of 150% for the two-photon Fock state and a 10-fold higher $\mathcal{P}$ for the three-photon Fock state. Thus, the FH is clearly outperforming the DH in the sense of the success probability in experiments as we have already seen for the ideal system parameters and concluded from the previous analysis. The nonclassicality of all generated states are violating the classical bounds, but the nonclassicality of the states generated within the FH are lower compared to the DH. This is caused again by the loop propagation losses, which we proved by making use of our theoretical model.

Furthermore, we investigated the effects of the loop propagation losses by making use of a DH-like generation within the FH measurements. These analyses clearly show that the main limiting factor in our system is the loop propagation losses, decreasing the fidelity of the DH-like generated states.

Because of the type of measurement, we are also able to generate three- or four-photon Fock states with a lower number of time bins as in the herald and even more interestingly, we are, in principle, able to generate arbitrary photon numbers in the signal. We have demonstrated the generation of a three-photon Fock state with two-bin heralding and a four-photon Fock state with two- and three bin heralding. Both results show a behavior being directly connected to the known effects of the feedback and the loop propagation losses. Moreover, we have shown the generation of a five-photon Fock state within the two-, three- and four-bin heralding. The generation of higher photon numbers is not possible within the DH without increasing the resolution of the heralding detection scheme. Moreover, the generation of Fock states with arbitrary photon numbers is not possible within the DH.

Finally, we have shown a two-photon Fock state measurement within the FH with increased efficiencies in the setup, enabling us to show higher squeezing parameters. This data set shows that the gap between the success probability of the FH and DH is increasing when increasing the squeezing and the efficiencies further.

The last experimental analysis investigates the photon-photon correlations generated within the FH. We show the two- and three-mode excess nonclassicalities within the DH and FH referring to the correlations between the idler photons. The DH is not showing any correlations between the idler modes, whereas the FH is clearly showing them. Thus, the feedback is inducing quantum correlations between the independently generated idler photons by the pair correlations of signal and idler. We could also show a similar behavior of the excess nonclassicality as the enhancement factor is decreasing with increasing time difference between two generated photons. The excess nonclassicality has a power dependence on the time difference between the two photons. The correlation decreases linear with increasing the squeezing parameter although this holds

true only for low squeezing values.

In general, we have shown the advantages of our novel approach in the sense of generation rates and induced long-range quantum correlations. We expect this advantages to be even more pronounced the more the setup will be optimized, mainly in the sense of loop propagation efficiencies.

5.2 Outlook

We will now discuss possible applications for our novel approach in addition to the shown application of the Fock state generation and the generation of long-range photon-photon correlations.

First, we can start further optimizing the current configuration of the setup, i.e. mainly increasing the loop propagation efficiency. Having a look back into the setup in Sec. 4.1.2 and Fig. 4.7, we can identify a few things that could be optimized. The BPF for filtering the pump is a silicon filter with a efficiency of 97.5% at 1550 nm. One can think about changing this filter into a more efficient filter, another type of filter, like a broadband filter at 1550nm, or test whether the DWDM filter in the two detection arms are already sufficient. Moreover, one should check whether it is even better to move the DWDM filter from the position after PBS-1 to the state detection path. Furthermore, the DM for the in-coupling of the pump is not an optimized DM-mirror, but more like every other mirror at 1550 nm transmissive for 775 nm light. Thus, the efficiency for transmitting the pump light is quite low with $\approx 50\%$. This could increase the squeezing parameter within the measurements even further. Another part is the mismatch of the measured loop efficiency of 72% and the effective efficiency in the measurements of 60.5%, which has to be investigated. In general, the less efficient part is the in-coupling and transmission of light through the source. Thus, one step could be to change the source with a more efficient one and further optimizing the in-coupling. This is indeed a hard task since the used source is already one of the most efficient ones.

Another approach could be to change the setup geometry and to reduce the components in the feedback. This could be, for example, a highly reflecting coating at one end-facet of the source to directly reflect the generated light back while the pump light is transmitted. This would lead to a increased mode overlap in the feedback and only one in- and out-coupling side, but a higher transmission loss in the source at the same time. In general, in this configuration, we can abandon the BPF and the DM altogether.
These changes and optimizations could lead, in general, to a more efficient Fock-state generation and enables us to find even stronger correlations for higher time differences between the idler photons.

We have already mentioned possible applications of the generated Fock states in Sec. 3.2.3. Thus, one can use the generated states and send them into another setup for generating for example Holland-Burnett states and Schrödinger cat states. Further-

more, we have already shown the generation of TNS states within the setup in Ref. [28] and in Appendix B, one can find a detailed description. Here, we will just briefly summarize this work. Within the current configuration of this setup, we are already able to generate multi-mode W and GHZ states with different configurations of the EOM and with different pumpings of the source. The only amendment is adding a phase stabilization in the setup to stabilize the feedback path to the laser. Furthermore, with addition of another delay path with a repetition rate of τ/n, we are able to generate two-dimensional TNS. One-dimensional TNS can be efficiently simulated on classical computers whereas two-dimensional TNS scale badly (e.g. exponentially) with the system size. Thus, being able to generate two-dimensional TNS leads to obtaining a non-trivial quantum-computational speedup. With adding further delays, it would be even possible to generate TNS of even higher dimensions.

The two-dimensional configuration of the setup shown in Fig. B.2 used for the generation of two-dimensional TNS is already looking like a one-dimensional quantum walk (see for example Ref. [152, 153]). We have already shown in Ref. [57] a quantum walk with an active element to achieve amplification of the light as it is done in classical optics. In principle, one could also think about amplification with a PDC source within the quantum walk. This is commonly known as driven quantum walks and was introduced by our group in Ref. [154]. Performing a driven quantum walk with a single-mode input leads to the same result as a multi-mode coherent state launching through a original quantum walk. Furthermore, driven quantum walks can create several output states by changing the shape of the pump or the frequency. The walker can be amplified in whatever step and also be coherently destroyed during the walk. Furthermore, we have already shown first simulations in Ref. [155]. Thus, this type of quantum walk could lead to interesting results, including quantum amplification, squeezing, and entanglement.

Furthermore, a completely different application of the setup can be found in the non-Hermitian generation of brighter broadband pseudo-thermal light (see Ref. [156]). This work shows that in contrast to the standard approach of lossless systems, in some scenarios, losses could be useful in quantum-state engineering. They assume a loss-engineered non-phase-matched material to increase brightness of broadband pseudo-thermal states, generated in one output mode of the source. This could be realized within our setup with some modifications. Instead of only one mode being fed back into the PDC source, they suggest to use both modes as a seed, where one mode accumulates more loss than the other one. This could be realized by changing PBS-1 in Fig. 4.7 into a partially polarizing beam splitter (PPBS), meaning that one mode is transmitted completely and the other mode only partially. The lossless mode is then exhibiting a larger brightness. Furthermore, since our process is phase-matched, the effective phase mismatch is introduced as a phase drift within the feedback of the photons, which can be conducted by not stabilizing the repetition rate of the laser. The light reflected at the PPBS is used for some extend as a herald and after t round trips of the cycling modes, we swap polarizations to measure the increase in brightness of the lossless mode as a function of the number of round trips.

Thus, the generation of Fock states are just the beginning of an exciting series of possible experiments with our novel approach, allowing us to access new types of application-relevant quantum states with high quality in the future. We are looking forward for further experiments in this direction.

Bibliography

[1] E. Knill, R. Laflamme, and G. Milburn. "A scheme for efficient quantum computation with linear optics". In: *Nature* 409 (2000), p. 46.

[2] N. Gisin and R. Thew. "Quantum communication". In: *Nat. Photon.* 1 (2007), p. 165.

[3] B. Vlastakis, G. Kirchmair, Z. Leghtas, et al. "Deterministically Encoding Quantum Information Using 100-Photon Schrödinger Cat States". In: *Science* 342 (2013), p. 607.

[4] M. Planck. "Ueber das Gesetz der Energieverteilung im Normalspectrum". In: *Annalen der Physik* 309.3 (1901), p. 553.

[5] A. Einstein. "Über einen die Erzeugung und Verwandlung des Lichtes betreffenden heuristischen Gesichtspunkt". In: *Annalen der Physik* 322.6 (1905), p. 132.

[6] G. I. Taylor. "Interference Fringes with Feeble Light". In: *Proc. Camb. Philos. Soc.* 14 (1909), p. 114.

[7] A. Einstein. "Zum gegenwärtigen Stand des Strahlungsproblems". In: *Phys. Zeitschr.* 10 (1909), p. 185.

[8] P. A. M. Dirac and N. H. D. Bohr. "The quantum theory of the emission and absorption of radiation". In: *Proceedings of the Royal Society of London. Series A, Containing Papers of a Mathematical and Physical Character* 114.767 (1927), p. 243.

[9] G. Lewis. "The Conservation of Photons". In: *Nature* 118 (1926), p. 874.

[10] R. Hanbury-Brown and R. Q. Twiss. "A new type of interferometer for use in radio astronomy". In: *Philosophical Magazine Series* 7.366 (1954), p. 663. eprint: `https://doi.org/10.1080/14786440708520475`.

[11] R. Hanbury-Brown and R. Q. Twiss. "Correlation between Photons in two Coherent Beams of Light". In: *Nature* 177 (1956), p. 27. eprint: `https://doi.org/10.1038/177027a0`.

[12] R. J. Glauber. "Coherent and Incoherent States of the Radiation Field". In: *Phys. Rev.* 131 (1963), p. 2766.

[13] H. J. Kimble and L. Mandel. "Theory of resonance fluorescence". In: *Phys. Rev. A* 13 (1976), p. 2123.

[14] H. J Kimble, M. Dagenais, and L. Mandel. "Photon Antibunching in Resonance Fluorescence". In: *Phys. Rev. Lett.* 39 (11 1977), p. 691.

[15] C. H. Bennett and G. Brassard. "Quantum cryptography: Public key distribution and coin tossing". In: *Theoretical Computer Science* 560 (2014), p. 7.

[16] P. Kok, W. J. Munro, K. Nemoto, et al. "Linear optical quantum computing with photonic qubits". In: *Rev. Mod. Phys.* 79 (1 2007), p. 135.

[17] M. A. Nielsen and I. L. Chuang. *Quantum Computation and Quantum Information: 10th Anniversary Edition*. Cambridge University Press, 2010.

[18] T. Rudolph. "Why I am optimistic about the silicon-photonic route to quantum computing". In: *APL Photonics* 2.3 (2017), p. 030901.

[19] J. A. Dunningham. "Using quantum theory to improve measurement precision". In: *Contemporary Physics* 47.5 (2006), p. 257.

[20] N. Gisin and R. Thew. "Quantum communication". In: *Nature Photon* 1 (2007), p. 165.

[21] M. D. Eisaman, J. Fan, A. Migdall, and S. V. Polyakov. "Invited Review Article: Single-photon sources and detectors". In: *Review of Scientific Instruments* 82.7 (2011), p. 071101.

[22] X. Cao, M. Zopf, and F. Ding. "Telecom wavelength single photon sources". In: *Journal of Semiconductors* 40.7 (2019), p. 071901.

[23] P. G. Kwiat, K. Mattle, H. Weinfurter, et al. "New High-Intensity Source of Polarization-Entangled Photon Pairs". In: *Phys. Rev. Lett.* 75 (1995), p. 4337.

[24] C. Kurtsiefer, M. Oberparleiter, and H. Weinfurter. "High-efficiency entangled photon pair collection in type-II parametric fluorescence". In: *Phys. Rev. A* 64 (2001), p. 023802.

[25] A. Einstein, B. Podolsky, and N. Rosen. "Can Quantum-Mechanical Description of Physical Reality Be Considered Complete?" In: *Phys. Rev.* 47 (1935), p. 777.

[26] X. Zou, K. Pahlke, and W. Mathis. "Generation of an entangled four-photon W state". In: *Phys. Rev. A* 66 (2002), p. 044302.

[27] X. Zou and W. Mathis. "Generating a four-photon polarization-entangled cluster state". In: *Phys. Rev. A* 71 (2005), p. 032308.

[28] I. Dhand, M. Engelkemeier, L. Sansoni, et al. "Proposal for Quantum Simulation via All-Optically-Generated Tensor Network States". In: *Phys. Rev. Lett.* 120 (2018), p. 130501.

[29] M. J. Holland and K. Burnett. "Interferometric detection of optical phase shifts at the Heisenberg limit". In: *Phys. Rev. Lett.* 71 (1993), p. 1355.

[30] A. Datta, L. Zhang, N. Thomas-Peter, et al. "Quantum metrology with imperfect states and detectors". In: *Phys. Rev. A* 83 (6 2011), p. 063836.

[31] P. Domokos, M. Brune, J. M. Raimond, and S. Haroche. "Photon-number-state generation with a single two-level atom in a cavity: a proposal". In: *The European Physical Journal D - Atomic, Molecular, Optical and Plasma Physics* 1.1 (1998), pp. 1–4. ISSN: 1434-6079.

[32] A. Kuhn, M. Hennrich, and G. Rempe. "Deterministic Single-Photon Source for Distributed Quantum Networking". In: *Phys. Rev. Lett.* 89 (2002), p. 067901.

[33] M. Wittemer, J.-P. Schröder, F. Hakelberg, et al. "Trapped-ion toolkit for studies of quantum harmonic oscillators under extreme conditions". In: *Philosophical Transactions of the Royal Society A: Mathematical, Physical and Engineering Sciences* 378.2177 (2020), p. 20190230.

[34] M. Uria, P. Solano, and C. Hermann-Avigliano. "Deterministic Generation of Large Fock States". In: *Phys. Rev. Lett.* 125 (2020), p. 093603.

[35] P. Michler, A. Kiraz, C. Becher, et al. "A Quantum Dot Single-Photon Turnstile Device". In: *Science* 290 (2000), p. 2282.

[36] D. Loss and D. P. DiVincenzo. "Quantum computation with quantum dots". In: *Phys. Rev. A* 57 (1998), p. 120.

[37] X. Ding, Y. He, Z.-C. Duan, et al. "On-Demand Single Photons with High Extraction Efficiency and Near-Unity Indistinguishability from a Resonantly Driven Quantum Dot in a Micropillar". In: *Phys. Rev. Lett.* 116 (2016), p. 020401.

[38] C. Kurtsiefer, S. Mayer, P. Zarda, and H. Weinfurter. "Stable Solid-State Source of Single Photons". In: *Phys. Rev. Lett.* 85 (2 2000), pp. 290–293.

[39] D. C. Burnham and D. L. Weinberg. "Observation of Simultaneity in Parametric Production of Optical Photon Pairs". In: *Phys. Rev. Lett.* 25 (1970), p. 84.

[40] P. Grangier, G. Roger, and A. Aspect. "Experimental Evidence for a Photon Anticorrelation Effect on a Beam Splitter: A New Light on Single-Photon Interferences". In: *Europhysics Letters (EPL)* 1.4 (1986), p. 173.

[41] R. Ghosh and L. Mandel. "Observation of nonclassical effects in the interference of two photons". In: *Phys. Rev. Lett.* 59 (1987), p. 1903.

[42] M. Fox. *Quantum optics: an introduction*. Oxford master series in atomic, optical, and laser physics. Oxford: Oxford Univ. Press, 2006.

[43] G.Harder, V. Ansari, B. Brecht, et al. "An optimized photon pair source for quantum circuits". In: *Opt. Express* 21.12 (2013), p. 13975.

[44] A. Eckstein, A. Christ, P. J. Mosley, and C. Silberhorn. "Highly Efficient Single-Pass Source of Pulsed Single-Mode Twin Beams of Light". In: *Phys. Rev. Lett.* 106 (2011), p. 013603.

[45] W. H. Louisell, A. Yariv, and A. E. Siegman. "Quantum Fluctuations and Noise in Parametric Processes. I." In: *Phys. Rev.* 124 (1961), p. 1646.

[46] D. A. Kleinman. "Theory of Optical Parametric Noise". In: *Phys. Rev.* 174 (1968), p. 1027.

[47] B. R. Mollow. "Photon Correlations in the Parametric Frequency Splitting of Light". In: *Phys. Rev. A* 8 (1973), p. 2684.

[48] R. J. Glauber. "Quantum Theory of Parametric Amplification I". In: John Wiley and Sons, Ltd, 2006. Chap. 6, pp. 221–262. ISBN: 9783527610075.

[49] B. Y. Zel'Dovich and D. N. Klyshko. "Field statistics in parametric luminescence". In: *ZhETF Pis ma Redaktsiiu* (1969), p. 9.

[50] E. Knill, R. Laflamme, and G. Milburn. "A scheme for efficient quantum computation with linear optics." In: *Nature* 409 (2001), p. 46.

[51] A. B. U'Ren, C. Silberhorn, K. Banaszek, and I. A. Walmsley. "Efficient Conditional Preparation of High-Fidelity Single Photon States for Fiber-Optic Quantum Networks". In: *Phys. Rev. Lett.* 93 (2004), p. 093601.

[52] E. Waks, E. Diamanti, and Y. Yamamoto. "Generation of photon number states". In: *New Journal of Physics* 8 (2006), p. 4.

[53] M. Cooper, L. J. Wright, C. Söller, and D. J. Smith. "Experimental generation of multi-photon Fock states". In: *Opt. Express* 21.5 (2013), p. 5309.

[54] M. Bouillard, G. Boucher, J. F. Ortas, B. Kanseri, and R. Tualle-Brouri. "High production rate of single-photon and two-photon Fock states for quantum state engineering". In: *Opt. Express* 27.3 (2019), p. 3113.

[55] K. T. McCusker and P. G. Kwiat. "Efficient Optical Quantum State Engineering". In: *Phys. Rev. Lett.* 103 (2009), p. 163602.

[56] B. L. Glebov, J. Fan, and A. Migdall. "Photon number squeezing in repeated parametric downconversion with ancillary photon-number measurements". In: *Opt. Express* 22 (2014), pp. 20358–20365.

[57] M. Engelkemeier, L. Lorz, S. De, et al. "Quantum photonics with active feedback loops". In: *Phys. Rev. A* 102 (2020), p. 023712.

[58] M. Engelkemeier, J. Sperling, J. Tiedau, et al. "Climbing the Fock ladder: Advancing multiphoton state generation". In: *arXiv* 2105.03720 (2021). arXiv: `2105.03720 [quant-ph]`.

[59] C. H. Bennett and G. Brassard. "Quantum cryptography: Public key distribution and coin tossing". In: *Theoretical Computer Science* 560 (2014), p. 7.

[60] S. Pirandola, B. R. Bardhan, T. Gehring, C. Weedbrook, and S. Lloyd. "Advances in photonic quantum sensing". In: *Nature Photonics* 12.12 (2018), p. 724.

[61] W. Demtröder. "Geometrische Optik". In: *Experimentalphysik 2: Elektrizität und Optik*. Berlin, Heidelberg: Springer Berlin Heidelberg, 2006, p. 259. ISBN: 978-3-540-33795-9.

[62] B. E. A. Saleh and M. C. Teich. *Fundamentals of photonics; 2nd ed.* Wiley series in pure and applied optics. New York, NY: Wiley, 2007.

[63] M. Bass, C. DeCusatis, J. Enoch, et al. *Handbook of Optics, Third Edition Volume I: Geometrical and Physical Optics, Polarized Light, Components and Instruments(Set)*. 3rd ed. USA: McGraw-Hill, Inc., 2009. ISBN: 0071498893.

[64] C. Gerry and P. Knight. *Introductory Quantum Optics*. Cambridge University Press, 2004.

[65] R. J. Glauber. "The Quantum Theory of Optical Coherence". In: *Phys. Rev.* 130 (1963), p. 2529.

[66] P. N. Butcher and D. Cotter. *The Elements of Nonlinear Optics*. Cambridge Studies in Modern Optics. Cambridge University Press, 1990.

[67] R. W. Boyd. *Nonlinear Optics, Third Edition*. 3rd. Academic Press, Inc., 2008. ISBN: 0123694701.

[68] M. Born, E. Wolf, A. B. Bhatia, et al. *Principles of Optics: Electromagnetic Theory of Propagation, Interference and Diffraction of Light*. 7th ed. Cambridge University Press, 1999.

[69] P. J. M. andJ. S. Lundeen, B. J. Smith, P. Wasylczyk, et al. "Heralded Generation of Ultrafast Single Photons in Pure Quantum States". In: *Phys. Rev. Lett.* 100 (2008), p. 133601.

[70] S. Krapick, H. Herrmann, V. Quiring, et al. "An efficient integrated two-color source for heralded single photons". In: *New Journal of Physics* 15 (2013), p. 033010.

[71] C. Eigner, L. Padberg, M. Santandrea, et al. "Spatially single mode photon pair source at 800 nm in periodically poled Rubidium exchanged KTP waveguides". In: *Opt. Express* 28 (2020), p. 32925.

[72] K. Laiho, K. N. Cassemiro, and C. Silberhorn. "Producing high fidelity single photons with optimal brightness via waveguided parametric down-conversion". In: *Opt. Express* 17 (2009), p. 22823.

[73] T. Dirmeier, J. Tiedau, I. Khan, et al. "Distillation of squeezing using an engineered pulsed parametric down-conversion source". In: *Opt. Express* 28 (2020), p. 30784.

[74] S. Barnett and P. Radmore. *Methods in Theoretical Quantum Optics*. Oxford science publications. Clarendon Press, 1997. ISBN: 9780198563624.

[75] C. K. Hong and L. Mandel. "Theory of parametric frequency down conversion of light". In: *Phys. Rev. A* 31 (1985), p. 2409.

[76] A. Christ, B. Brecht, W. Mauerer, and C. Silberhorn. "Theory of quantum frequency conversion and type-II parametric down-conversion in the high-gain regime". In: *New Journal of Physics* 15.5 (2013), p. 053038.

[77] N. Quesada and J. E. Sipe. "Time-Ordering Effects in the Generation of Entangled Photons Using Nonlinear Optical Processes". In: *Phys. Rev. Lett.* 114 (2015), p. 093903.

[78] K. C. Law, I. A. Walmsley, and J. H. Eberly. "Continuous Frequency Entanglement: Effective Finite Hilbert Space and Entropy Control". In: *Phys. Rev. Lett.* 84 (2000), p. 5304.

[79] V. Singh. "Einstein-Podolsky-Rosen Correlations". In: *Recent Developments in Quantum Optics*. Ed. by R. Inguva. Springer US, 1993, pp. 37–42. ISBN: 978-1-4615-2936-1.

[80] H. Paul, P. Törmä, T. Kiss, and I. Jex. "Photon Chopping: New Way to Measure the Quantum State of Light". In: *Phys. Rev. Lett.* 76 (14 1996), p. 2464.

[81] D. Achilles, C. Silberhorn, C. Sliwa, et al. "Photon-number-resolving detection using time-multiplexing". In: *Journal of Modern Optics* 51 (2004), p. 1499.

[82] J. Sperling, W. Vogel, and G. S. Agarwal. "True photocounting statistics of multiple on-off detectors". In: *Phys. Rev. A* 85 (2012), p. 023820.

[83] J. Sperling, W. Vogel, and G. S. Agarwal. "Correlation measurements with on-off detectors". In: *Phys. Rev. A* 88 (2013), p. 043821.

[84] J. Sperling, M. Bohmann, W. Vogel, et al. "Uncovering Quantum Correlations with Time-Multiplexed Click Detection". In: *Phys. Rev. Lett.* 115 (2015), p. 023601.

[85] G. Harder, T. J. Bartley, A. E. Lita, et al. "Single-Mode Parametric-Down-Conversion States with 50 Photons as a Source for Mesoscopic Quantum Optics". In: *Phys. Rev. Lett.* 116 (2016), p. 143601.

[86] J. Tiedau, T. J. Bartley, G. Harder, et al. "Scalability of parametric down-conversion for generating higher-order Fock states". In: *Phys. Rev. A* 100 (2019), p. 041802.

[87] W. Mauerer, M. Avenhaus, W. Helwig, and C. Silberhorn. "How colors influence numbers: Photon statistics of parametric down-conversion". In: *Phys. Rev. A* 80 (2009), p. 053815.

[88] A. Christ and C. Silberhorn. "Limits on the deterministic creation of pure single-photon states using parametric down-conversion". In: *Phys. Rev. A* 85 (2012), p. 023829.

[89] A. L. Migdall, D. Branning, and S. Castelletto. "Tailoring single-photon and multiphoton probabilities of a single-photon on-demand source". In: *Phys. Rev. A* 66 (2002), p. 053805.

[90] T. B. Pittman, B. C. Jacobs, and J. D. Franson. "Single photons on pseudodemand from stored parametric down-conversion". In: *Phys. Rev. A* 66 (2002), p. 042303.

[91] X.-S. Ma, S. Zotter, J. Kofler, T. Jennewein, and A. Zeilinger. "Experimental generation of single photons via active multiplexing". In: *Phys. Rev. A* 83 (2011), p. 043814.

[92] T. Jennewein, M. Barbieri, and A. G. White. "Single-photon device requirements for operating linear optics quantum computing outside the post-selection basis". In: *Journal of Modern Optics* 58 (2011), pp. 276–287.

[93] F. Kaneda and R. G. Kwiat. "High-efficiency single-photon generation via large-scale active time multiplexing". In: *Science Advances* 5.10 (2019).

[94] E. Meyer-Scott, C. Silberhorn, and A. Migdall. "Single-photon sources: Approaching the ideal through multiplexing". In: *Review of Scientific Instruments* 91 (2020), p. 041101.

[95] K. Sanaka. "Linear optical extraction of photon-number Fock states from coherent states". In: *Phys. Rev. A* 71 (2005), p. 021801.

[96] L. A. Ngah, O. Alibart, L. Labonté, V. D'Auria, and S. Tanzilli. "Ultra-fast heralded single photon source based on telecom technology". In: *Laser and Photonics Reviews* 9 (2015), p. L1.

[97] G. M. D'Ariano, L. Maccone, M. G. A. Paris, and M. F. Sacchi. "Optical Fock-state synthesizer". In: *Phys. Rev. A* 61 (2000), p. 053817.

[98] K. R. Brown, K. M. Dani, D. M. Stamper-Kurn, and F. B. Whaley. "Deterministic optical Fock-state generation". In: *Phys. Rev. A* 67 (2003), p. 043818.

[99] T. B. Pittman, B. C. Jacobs, and J. D. Franson. "Heralding single photons from pulsed parametric down-conversion". In: *Optics Communications* 246 (2005), pp. 545 –550.

[100] S. Castelletto, I. P. Degiovanni, V. Schettini, and A. Migdall. "Optimizing single-photon-source heralding efficiency and detection efficiency metrology at 1550nm using periodically poled lithium niobate". In: *Metrologia* 43 (2006), S56–S60.

[101] A. Zavatta, S. Viciani, and M. Bellini. "Tomographic reconstruction of the single-photon Fock state by high-frequency homodyne detection". In: *Phys. Rev. A* 70 (2004), p. 053821.

[102] A. I. Lvovsky, H. Hansen, T. Aichele, et al. "Quantum State Reconstruction of the Single-Photon Fock State". In: *Phys. Rev. Lett.* 87 (2001), p. 050402.

[103] A. M. Brańczyk, T. C. Ralph, W. Helwig, and C. Silberhorn. "Optimized generation of heralded Fock states using parametric down-conversion". In: *New Journal of Physics* 12 (2010), p. 063001.

[104] A. Ourjoumtsev, R. Tualle-Brouri, and P. Grangier. "Quantum Homodyne Tomography of a Two-Photon Fock State". In: *Phys. Rev. Lett.* 96 (2006), p. 213601.

[105] M. Homeister. *Quantum Computing verstehen : Grundlagen - Anwendungen - Perspektiven*. 4. Auflage. 2017. ISBN: 978-3-658-10455-9.

[106] M. Krenn, M. Malik, T. Scheidl, R. Ursin, and A. Zeilinger. "Optics in our time". In: *Optics in Our Time*. Ed. by M. D. Al-Amri, M. El-Gomati, and M. S. Zubairy. Springer International Publishing, 2016. Chap. Quantum Communication with Photons, pp. 455–482. ISBN: 978-3-319-31903-2.

[107] D. P. DiVincenzo. "The Physical Implementation of Quantum Computation". In: *Fortschritte der Physik* 48 (2000), p. 771.

[108] G. Xiang, H. Hofmann, and G. Pryde. "Optimal multi-photon phase sensing with a single interference fringe". In: *Sci Rep* 3 (2013), p. 2684.

[109] V. Giovannetti, S. Lloyd, and L. Maccone. "Advances in quantum metrology." In: *Nature Photon* 5 (2011), p. 222.

[110] M. Bergmann and P. van Loock. "Quantum error correction against photon loss using NOON states". In: *Phys. Rev. A* 94 (2016), p. 012311.

[111] K. Edamatsu, R. Shimizu, and T. Itoh. "Measurement of the Photonic de Broglie Wavelength of Entangled Photon Pairs Generated by Spontaneous Parametric Down-Conversion". In: *Phys. Rev. Lett.* 89 (2002), p. 213601.

[112] T. Nagata, R. Okamoto, J. L. O'Brien, K. Sasaki, and S. Takeuchi. "Beating the Standard Quantum Limit with Four-Entangled Photons". In: *Science* 316 (2007), p. 726.

[113] M. Yabuno, R. Shimizu, Y. Mitsumori, H. Kosaka, and K. Edamatsu. "Four-photon quantum interferometry at a telecom wavelength". In: *Phys. Rev. A* 86 (2012), p. 010302.

[114] R.-B. Jin, M. Fujiwara, S. Ryosuke, et al. "Detection-dependent six-photon Holland-Burnett state interference". In: *Sci Rep* 6 (2016), p. 36914.

[115] E. Schrödinger. "Die gegenwärtige Situation in der Quantenmechanik". In: *Naturwissenschaften* 23 (1935), p. 807.

[116] M. Stobińska, H. Jeong, and T. C. Ralph. "Violation of Bell's inequality using classical measurements and nonlinear local operations". In: *Phys. Rev. A* 75 (2007), p. 052105.

[117] J. Wenger, M. Hafezi, F. Grosshans, R. Tualle-Brouri, and P. Grangier. "Maximal violation of Bell inequalities using continuous-variable measurements". In: *Phys. Rev. A* 67 (2003), p. 012105.

[118] T. C. Ralph, A. Gilchrist, G. J. Milburn, W. J. Munro, and S. Glancy. "Quantum computation with optical coherent states". In: *Phys. Rev. A* 68 (2003), p. 042319.

[119] H. Jeong, M. S. Kim, and J. Lee. "Quantum-information processing for a coherent superposition state via a mixedentangled coherent channel". In: *Phys. Rev. A* 64 (2001), p. 052308.

[120] A. Ourjoumtsev, J. Hyunseok, R. Tualle-Brouri, and P. Grangier. "Generation of optical 'Schrödinger cats' from photon number states." In: *Nature* 448 (2007), p. 784. eprint: `https://doi.org/10.1038/nature06054`.

[121] E. V. Mikheev, A. S. Pugin, D. A. Kuts, S. A. Podoshvedov, and N. B. An. "Efficient production of large-size optical Schrödinger cat states". In: *Sci Rep* 9 (2019), p. 14301.

[122] W. Dür, G. Vidal, and J. I. Cirac. "Three qubits can be entangled in two inequivalent ways". In: *Phys. Rev. A* 62 (2000), p. 062314.

[123] J. Joo, J. Lee, J. Jang, and Y.-J. Park. "Quantum Secure Communication via a W State". In: *Journal of the Korean Physical Society* 46.4 (2005), p. 763.

[124] W. Jian, Z. Quan, and T. Chao-Jing. "Quantum Secure Communication Scheme with W State". In: *Communications in Theoretical Physics* 48.4 (2007), p. 637.

[125] V. Bužek and M. Hillery. "Quantum copying: Beyond the no-cloning theorem". In: *Phys. Rev. A* 54 (1996), p. 1844.

[126] N. Gisin and S. Massar. "Optimal Quantum Cloning Machines". In: *Phys. Rev. Lett.* 79 (1997), p. 2153.

[127] D. Bruß, D. P. DiVincenzo, A. Ekert, et al. "Optimal universal and state-dependent quantum cloning". In: *Phys. Rev. A* 57 (1998), p. 2368.

[128] T. Yamamoto, K. Tamaki, M. Koashi, and N. Imoto. "Polarization-entangled W state using parametric down-conversion". In: *Phys. Rev. A* 66 (2002), p. 064301.

[129] J. Biamonte and V. Bergholm. *Tensor Networks in a Nutshell*. 2017. arXiv: `1708.00006 [quant-ph]`.

[130] R. Orús. "A practical introduction to tensor networks: Matrix product states and projected entangled pair states". In: *Annals of Physics* 349 (2014), p. 117.

[131] Y. Sagi. "Scheme for generating Greenberger-Horne-Zeilinger-type states of n photons". In: *Phys. Rev. A* 68 (2003), p. 042320.

[132] A. Christ, K. Laiho, A. Eckstein, K. N. Cassemiro, and C. Silberhorn. "Probing multimode squeezing with correlation functions". In: *New Journal of Physics* 13.3 (2011), p. 033027.

[133] E. Schrödinger. "Der stetige Übergang von der Mikro- zur Makromechanik". In: *Naturwissenschaften* 14.28 (1926), pp. 664–666.

[134] P. R. Tapster and J. G. Rarity. "Photon statistics of pulsed parametric light". In: *Journal of Modern Optics* 45 (1998), p. 595.

[135] L. Mandel. "Sub-Poissonian photon statistics in resonance fluorescence". In: *Opt. Lett.* 4.7 (1979), p. 205.

[136] M. Avenhaus., K. Laiho, M. V. Chekhova, and C. Silberhorn. "Accessing Higher Order Correlations in Quantum Optical States by Time Multiplexing". In: *Phys. Rev. Lett.* 104 (2010), p. 063602.

[137] T. J. Bartley, G. Donati, X.-M. Jin, et al. "Direct Observation of Sub-Binomial Light". In: *Phys. Rev. Lett.* 110 (17 2013), p. 173602.

[138] J. Tiedau, M. Engelkemeier, B. Brecht, J. Sperling, and C. Silberhorn. "Statistical Benchmarking of Scalable Photonic Quantum Systems". In: *Phys. Rev. Lett.* 126 (2021), p. 023601.

[139] L. Padberg, M. Santandrea, M. Rüsing, et al. "Characterisation of width-dependent diffusion dynamics in rubidium-exchanged KTP waveguides". In: *Opt. Express* 28 (2020), p. 24353.

[140] R. Regener and W. Sohler. "Loss in low-finesse Ti:LiNbO3 optical waveguide resonators". In: *Appl. Phys. B* 36 (1985), p. 143.

[141] M. Avenhaus, A. Eckstein, P. J. Mosley, and C. Silberhorn. "Fiber-assisted single-photon spectrograph". In: *Opt. Lett.* 34 (2009), p. 2873.

[142] W. Vogel and D.-G. Welsch. *Quantum Optics*. Wiley, 2006.

[143] J. Tiedau. "Quantum optics in the photon number basis". PhD thesis. Paderborn: Paderborn University, Department of physics, 2020.

[144] A. Bhattacharyya. "On a Measure of Divergence between Two Multinomial Populations". In: *Sankhyā: The Indian Journal of Statistics (1933-1960)* 7 (1946), p. 401.

[145] O. P. Kovalenko, J. Sperling, W. Vogel, and A. A. Semenov. "Geometrical picture of photocounting measurements". In: *Phys. Rev. A* 97 (2018), p. 023845.

[146] L. Knoll and G. Weber. "Theory of n-fold time-resolved correlation spectroscopy and its application to resonance fluorescence radiation". In: *Journal of Physics B: Atomic and Molecular Physics* 19.18 (1986), p. 2817.

[147] W. Vogel. "Nonclassical Correlation Properties of Radiation Fields". In: *Phys. Rev. Lett.* 100 (2008), p. 013605.

[148] Y. Aharonov, S. Popescu, J. Tollaksen, and L. Vaidman. "Multiple-time states and multiple-time measurements in quantum mechanics". In: *Phys. Rev. A* 79 (2009), p. 052110.

[149] S. Brierley, A. Kosowski, M. Markiewicz, T. Paterek, and A. Przysiężna. "Nonclassicality of Temporal Correlations". In: *Phys. Rev. Lett.* 115 (2015), p. 120404.

[150] F. Krumm, W. Vogel, and J. Sperling. "Time-dependent quantum correlations in phase space". In: *Phys. Rev. A* 95 (2017), p. 063805.

[151] J. Sperling and I. A. Walmsley. "Classical evolution in quantum systems". In: *Physica Scripta* 95.6 (2020), p. 065101.

[152] A. Schreiber, K. N. Cassemiro, V. Potoăek, et al. "Photons Walking the Line: A Quantum Walk with Adjustable Coin Operations". In: *Phys. Rev. Lett.* 104 (5 2010), p. 050502.

[153] A. Schreiber, A. Gábris, P. P. Rohde, et al. "A 2D Quantum Walk Simulation of Two-Particle Dynamics". In: *Science* 336.6077 (2012), pp. 55–58. ISSN: 0036-8075. eprint: `https://science.sciencemag.org/content/336/6077/55.full.pdf`.

[154] C. S. Hamilton, R. Kruse, L. Sansoni, C. Silberhorn, and I. Jex. "Driven Quantum Walks". In: *Phys. Rev. Lett.* 113 (2014), p. 083602.

[155] P. Held. "Driven Gaussian Quantum Walks". B.Sc. Thesis. Paderborn: Paderborn University, Department of physics, 2020.

[156] N. Quesada, E. Adjei, R. El-Ganainy, and A. M. Brańczyk. "Non-Hermitian engineering for brighter broadband pseudothermal light". In: *Phys. Rev. A* 100 (2019), p. 043805.

[157] R. Loudon. *The Quantum Theory of Light*. Oxford: Clarendon Press, 1973.

[158] L. Zehnder. "Ein neuer Interferenzrefraktor". In: *Zeitschrift für Instrumentenkunde* 11 (1891), p. 275.

[159] L. Mach. "Über einen Interferenzrefraktor". In: *Zeitschrift für Instrumentenkunde* 12 (1892), p. 83.

Acknowledgment

First of all, I would like to thank my supervisor Professor Dr. Christine Silberhorn for giving me the chance to work on such a amazing and interesting topic. I thank you for giving me the opportunity and for believing in my ability to research in the field of integrated quantum optics, even though I came from a completely different background. Thanks for your guidance, advice and help.

Furthermore, I want to thank my second referee J.-Prof. Dr. Polina Sharapova for evaluating my thesis.

Special thanks to Benjamin Brecht and Jan Sperling for helping me in experiment and theory. Without both of you this work and this results would not have been possible. Also thanks for proofreading my thesis to both and especially to Jan for finding every single wrongly placed and missing comma and hyphen.

Also many thanks to Sonja Barkhofen for introducing me to the topic when I started with my Phd. Thank you for all your support.

Furthermore, thanks to Johannes Tiedau, Evan Meyer-Scott and Syamsundar De for all the discussions, proofreading of my papers and helping me in the lab.
I thank also my collaborators Prof. Dr. Martin Plenio and Ish Dhand for all our successful projects, discussions and results coming out of this collaboration.

Thanks to all my colleagues in the group for this great time together. Especially I want to mention Felix vom Bruch, Christof Eigner and Laura Padberg. Thanks Felix for proofreading my thesis and having a look at my topic from another perspective and for supporting me especially towards the end of my thesis. One should mention his contribution to the experiment, as he very selflessly changed a beam block.
Thank you Christof and Laura for great times in the office during our morning coffee sessions. Thanks for your friendship, the talks about work, private and funny stuff, the little Christmas sessions and all the time together.

Furthermore, I will thank Michael Stefszky, Kai Hong Luo, Christian Kießler and Nid-

hin Prasannan for their support and thanks to the whole group.

Many thanks also to our secretaries Petra Bobe and Rita Prevor for all their support regarding administrative stuff, helping me with all the forms and very nice personal talks.

Zum Schluss möchte ich meinem Vater danken ohne dessen Zuspruch, Unterstützung und fortwährendes Fördern und Fordern, ich nicht dort wäre wo ich heute bin. Danke für alles! Außerdem danke ich meinen Geschwistern, welche immer für mich da waren, mich jederzeit unterstützt haben und mir während meines Studiums und der Promotion auf allen Ebenen geholfen haben. Des Weiteren möchte ich meinem Cousin danken, mit welchem ich jederzeit über meine Arbeit sprechen konnte und der mich für die Abbildung zu den Korrelationen inspiriert hat und seiner Frau, welche mich mit entspannten Abenden von meiner Arbeit ablenken konnte. Außerdem widme ich diese Arbeit meiner verstorbenen Oma für ihre Liebe und Unterstützung.

Chapter

A

List of scientific contributions

A.1 Publications at University of Paderborn

(1) Feedback-mediated long-range photon-photon correlations

Melanie Engelkemeier, Jan Sperling, Johannes Tiedau, Sonja Barkhofen, Ish Dhand, Martin B. Plenio, Benjamin Brecht and Christine Silberhorn
Manuscript in preparation

(2) Climbing the Fock ladder: Advancing multiphoton state generation

Melanie Engelkemeier, Jan Sperling, Johannes Tiedau, Sonja Barkhofen, Ish Dhand, Martin B. Plenio, Benjamin Brecht and Christine Silberhorn
Submitted to physical review letter on 12th of May 2021

(3) Statistical Benchmarking of Scalable Photonic Quantum Systems

Johannes Tiedau, Melanie Engelkemeier, Benjamin Brecht, Jan Sperling, Christine Silberhorn
Physical Review Letter 126, 023601 (2021)

(4) Quantum photonics with active feedback loops

Melanie Engelkemeier , Lennart Lorz, Syamsundar De, Benjamin Brecht, Ish Dhand, Martin B. Plenio, Christine Silberhorn, and Jan Sperling
Physical Review A 102, 023712 (2020)

(5) Proposal for Quantum Simulation via All-Optically-Generated Tensor Network States

Ish Dhand, Melanie Engelkemeier, Linda Sansoni, Sonja Barkhofen, Christine Silberhorn, Martin B Plenio
Physical Review Letter 120,130501 (2018)

A.2 Conference Contributions

(1) Multi-photon Fock-state generation via climbing the Fock ladder

Melanie Engelkemeier, Jan Sperling, Johannes Tiedau, Sonja Barkhofen, Ish Dhand, Martin B. Plenio, Benjamin Brecht and Christine Silberhorn
CLEO US 2021 - talk

(2) Quantum Feedback, self-stimulation and Fock State Generation

Melanie Engelkemeier, Ish Dhand, Evan Meyer-Scott, Jan Sperling, Sonja Barkhofen, Benjamin Brecht, Martin Plenio, and Christine Silberhorn
DPG spring meeting, Hannover 2020 - talk

(3) State generation with quantum feedback in parametric down-conversion

Melanie Engelkemeier, Ish Dhand, Evan Meyer-Scott, Jan Sperling, Sonja Barkofen, Benjamin Brecht, Martin Plenio and Christine Silberhorn
CoCus, Vienna 2019 - poster

(4) Quantum feedback in parametric down-conversion

Melanie Engelkemeier, Evan Meyer-Scott, Jan Sperling, Sonja Barkofen, Benjamin Brecht and Christine Silberhorn
CEWQO, Paderborn 2019 - poster

(5) State generation by quantum feedback in parametric downconversion

Melanie Engelkemeier, Evan Meyer-Scott, Jan Sperling, Sonja Barkhofen, Benjamin Brecht, and Christine Silberhorn
DPG spring meeting, Rostock 2019 - talk

(6) All-optically generation of tensor network states in one and higher dimensions

Melanie Engelkemeier, Ish Dhand, Linda Sansoni, Sonja Barkhofen, Christine Silberhorn, and Martin Plenio
DPG spring meeting, Erlangen 2018 - talk

(7) Towards a feedbacked down-conversion source for large complex quantum states

Melanie Engelkemeier, Regina Kruse, Linda Sansoni, Sonja Barkhofen, and Christine Silberhorn
DPG spring meeting, Mainz 2017 - poster

A.3 Publications at TU Dortmund

(1) **Statistics of VHE γ-rays in temporal association with radio giant pulses from the Crab pulsar**

MAGIC Collaboration
Astronomy & Astrophysics 634, A25 (2020)

(2) **Extreme HBL behavior of Markarian 501 during 2012**

MAGIC Collaboration
Astronomy & Astrophysics 620, A181 (2018)

(3) **Constraints on particle acceleration in SS433/W50 from MAGIC and HESS observations**

MAGIC Collaboration
Astronomy & Astrophysics 612, A14 (2018)

(4) **The 2016–2017 peak luminosity of the pre-main sequence variable V2492 Cygni**

MAGIC Collaboration
Astronomy & Astrophysics 611, A54 (2018)

(5) **Search for very high-energy gamma-ray emission from the microquasar Cygnus X-1 with the MAGIC telescopes**

MAGIC Collaboration
Monthly Notices of the Royal Astronomical Society 472, 3474 (2017)

(6) **A cut-off in the TeV gamma-ray spectrum of the SNR Cassiopeia A**

MAGIC Collaboration
Monthly notices of the royal astronomical society 472, 2956 (2017)

(7) **MAGIC observations of the microquasar V404 Cygni during the 2015 outburst**

MAGIC Collaboration
Monthly notices of the royal astronomical society 471, 1688 (2017)

(8) **Observation of the black widow B1957+ 20 millisecond pulsar binary system with the MAGIC telescopes**

MAGIC Collaboration
Monthly notices of the royal astronomical society 470, 4608 (2017)

(9) **Cherenkov Telescope Array Contributions to the 35th International Cosmic Ray Conference (ICRC2017)**

MAGIC Collaboration
arXiv 1709.03483 (2017)

(10) **Performance of the MAGIC telescopes under moonlight**
MAGIC Collaboration
Astroparticle Physics 94, 29 (2017)

(11) **Constraining Lorentz invariance violation using the Crab Pulsar emission observed up to TeV energies by MAGIC**
The Astrophysical Journal Supplement Series 232, 9 (2017)

(12) **MAGIC Contributions to the 35th International Cosmic Ray Conference (ICRC2017)**
MAGIC Collaboration
arXiv 1708.05153 (2017)

(13) **First multi-wavelength campaign on the gamma-ray-loud active galaxy IC 310**
MAGIC Collaboration
Astronomy & Astrophysics 603, A25 (2017)

(14) **Multiwavelength observations of a VHE gamma-ray flare from PKS 1510-089 in 2015**
MAGIC Collaboration
Astronomy & Astrophysics 603, A29 (2017)

(15) **Multiband variability studies and novel broadband SED modeling of Mrk 501 in 2009**
MAGIC Collaboration
Astronomy & Astrophysics 603, A31 (2017)

(16) **Very-high-energy gamma-ray observations of the Type Ia Supernova SN 2014J with the MAGIC telescopes**
MAGIC Collaboration
Astronomy & Astrophysics 602, A98 (2017)

(17) **MAGIC detection of very high energy γ-ray emission from the low-luminosity blazar 1ES 1741+ 196**
MAGIC Collaboration
Monthly Notices of the Royal Astronomical Society 468, 1534 (2017)

(18) **Observations of Sagittarius A* during the pericenter passage of the G2 object with MAGIC**
MAGIC Collaboration
Astronomy & Astrophysics 601, A33 (2017)

(19) **A search for spectral hysteresis and energy-dependent time lags from X-ray and TeV gamma-ray observations of Mrk 421**
MAGIC Collaboration
The Astrophysical Journal 834, 2 (2016)

(20) Detection of very high energy gamma-ray emission from the gravitationally lensed blazar QSO B0218+ 357 with the MAGIC telescopes

MAGIC Collaboration
Astronomy & Astrophysics 595, A98 (2016)

(21) Multiwavelength observations of a VHE gamma-ray flare from PKS 1510-089 in 2015

MAGIC Collaboration
PUBDB-2016-06249 (2016)

Chapter B

Tensor network state generation

The developed setup as it is described in Sec. 4.1.2 enables us to generate one-dimensional tensor network states (TNS) and with an extension, we are able to generate two-di/-men/-sion/-al TNS. Thus, the introduced applications given in Sec. 3.2.3 can be measured within the FH. Here, we will present the theoretical proposed generation of these states. So far, the experimental measurements have to be performed within the setup. The content we present here was published in Ref. [28].

Current implementations for generating TNS states typically rely on spatial modes of light increasing with the required size of the TNS [26, 27]. We make use of temporal modes of light (commonly known as time bins) in our setup to overcome these limitations. The experimental setup for the generation of the one-dimensional TNS is already depicted in Fig. 4.1 (left). We can represent the setup in another form, the quantum circuit, to emphasize the generation of one-dimensional TNS. We depict the quantum circuit for four round trips of the cycling mode in Fig B.1. Thus, we consider five input modes with vacuum $|0\rangle$ since we add after every detection of the idler (V-polarized photon) another mode and the cycling mode is detected after four round trips. In this illustration, $\hat{S}^{(i)}$ represents the two-mode squeezing operation as it is given in Eq. (4.10) and $\hat{V}^{(i)}$ gives the EOM transformation. The swapping of the modes shows the action of the PBS to detect the idler mode (solid red lines) and to make the signal mode (dashed dark red lines). The final TNS is then represented by the temporal modes $\hat{b}_1$ to $\hat{b}_4$ in the upper right grey box. A post selection of the TNS can be performed by the cycling mode $\hat{b}_5$ (box with red contour) containing at least one photon. One cycle in the setup is then represented by one two-mode squeezing $\hat{S}^{(i)}$, the mode swapping and a EOM transformation $\hat{V}^{(i)}$.

Suppose we want to generate a heralded three-mode W-state as we have introduced it in Sec. 3.2.3. This then leads to $\hat{S}^{(i)} = \hat{S}$ for $i\epsilon\ \{1,2,3\}$, $\hat{S}^{(4)} = \mathbb{1}$. Furthermore, the signal mode is cycling without a EOM transformation leading to $\hat{V}^{(i)} = \mathbb{1}$ for $i\epsilon$ $\{1,2\}$ and is swapped in polarization in the last EOM transformation $\hat{V}^{(3)} = \hat{V}$. We can calculate the resulting W state in a very simple way by a Taylor expansion of the

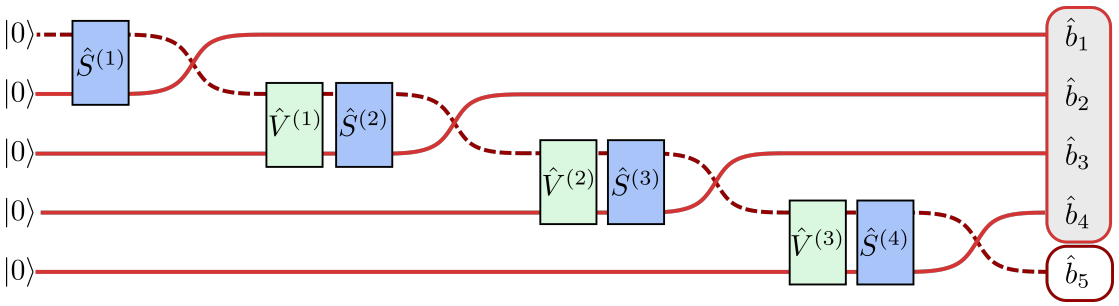

Figure B.1.: Quantum circuit with four cycles in the feedback for the experimental generation of TNS. The input modes are in vacuum $|0\rangle$, the output modes $\hat{b}_i$ represent the final state. $\hat{S}^{(i)}$ is the two-mode PDC process and $\hat{V}^{(i)}$ the EOM transformation. Redrawn from Ref. [28].

two-mode squeezing operator,

$$\begin{aligned}\hat{S} &= \exp(\zeta \hat{a}_V^\dagger \otimes \hat{a}_H^\dagger - \zeta^* \hat{a}_V \otimes \hat{a}_H) \\ &\approx \mathbb{1} + (\zeta \hat{a}_V^\dagger \otimes \hat{a}_H^\dagger - \zeta^* \hat{a}_V \otimes \hat{a}_H) + O(\zeta^2).\end{aligned} \tag{B.1}$$

The initial state is given as vacuum in every mode $|0,0,0,0,\ldots\rangle$, leading to the first PDC generation that acts on the first two modes as

$$\begin{aligned}|\psi_1\rangle &= \hat{S}\,|0,0,0,0,\ldots\rangle \\ &= |0,0,0,0,\ldots\rangle + \zeta\,|1,1,0,0,\ldots\rangle + O(\zeta^2).\end{aligned} \tag{B.2}$$

We are not accounting for ζ^2-terms in the state generation since we assume that the squeezing parameter is sufficiently small for higher terms and we have omitted the normalization terms for simplicity. Thus, the second PDC process can be written as

$$\begin{aligned}|\psi_2\rangle &= \hat{S}\,|\psi_1\rangle \\ &= |0,0,0,0,\ldots\rangle + \zeta\,|1,0,1,0,\ldots\rangle + \zeta\,|1,1,0,0,\ldots\rangle + O(\zeta^2)\end{aligned} \tag{B.3}$$

and further the last PDC process leads to

$$\begin{aligned}|\psi_3\rangle &= \hat{S}\,|\psi_2\rangle \\ &= |0,0,0,0,\ldots\rangle + \zeta\,|1,0,0,1,\ldots\rangle + \zeta\,|1,0,1,0,\ldots\rangle + \zeta\,|1,1,0,0,\ldots\rangle + O(\zeta^2).\end{aligned} \tag{B.4}$$

We can rewrite this state in the following way while removing unused modes:

$$|\psi_4\rangle = |0\rangle \otimes |0,0,0\rangle + \zeta\,|1\rangle \otimes (|0,0,1\rangle + |0,1,0\rangle + |1,0,0\rangle) + O(\zeta^2), \tag{B.5}$$

leading to the three-mode W state by heralding onto one click in $\hat{b}_4$. Thus, we can expand the number of modes in the W state by adding more cycles.

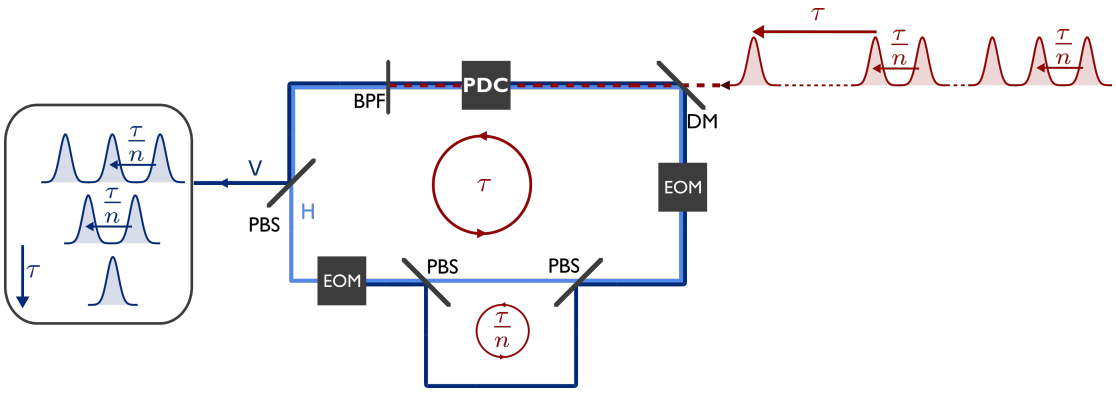

Figure B.2.: Extended setup for the generation of two-dimensional TNS. A second EOM is added as well as a delay path with τ/n for the vertical polarized photons from the second PDC process.

Assuming we want to generate a four-mode GHZ (Greenberger–Horne–Zeilinger) state, we will find that $\hat{S}^{(i)} = \hat{S}$ for odd numbers $i \in \{2, 4\}$ and $\hat{S}^{(i)} = \mathbb{1}$ for even numbers i, meaning no pumping of the PDC process. In contrast, the EOM transformations are performed for even numbers, $\hat{V}^{(i)} = \hat{V}$, and for odd numbers $\hat{V}^{(i)} = \mathbb{1}$. We can now derive the state, starting with applying a two-mode squeezing onto the initial vacuum state as we have shown for the W state (see Eq. (B.2)) and then perform a EOM transformation as

$$\begin{aligned} |\psi_2\rangle &= \hat{V}\,|\psi_1\rangle \\ &= |0,0,0,0,\ldots\rangle + \zeta\,|0,1,1,0,\ldots\rangle + O(\zeta^2). \end{aligned} \tag{B.6}$$

Thus, the next PDC process acts on the first and fourth mode, resulting in

$$|\psi_3\rangle = |0,0,0,0,\ldots\rangle + \zeta\,|1,0,0,1,\ldots\rangle + \zeta\,|0,1,1,0,\ldots\rangle + O(\zeta^2). \tag{B.7}$$

With the last EOM transformation, the state is then given as

$$|\psi_4\rangle = |0,0,0,0,\ldots\rangle + \zeta(|1,1,0,0,\ldots\rangle + |0,0,1,1,\ldots\rangle) + O(\zeta^2), \tag{B.8}$$

which is a superposition of the GHZ state with vacuum.

This means, with the current implementation of the setup as it is used for the Fock-state generation, we are able to generate multi-mode W and GHZ states. The only things to change are the readout of the data and the EOM switchings.

So far, classical computer can efficiently obtain properties of one-dimensional TNS. For higher dimensional TNS, classical algorithms scale exponentially with the system size. Thus, the generation of higher dimensional TNS would lead to a quantum-computational speedup of these simulations. With adding a EOM and another delay path within the setup, we are able to generate two-dimensional TNS. In Fig. B.2, we find the setup we would need for this generation. Due to a swapping of the signal polarization into a

diagonal polarization and the delay path adding a time delay of τ/n, we transform the polarization modes into different time bins, similar to two-dimensional quantum walks [152, 153]. Pumping the source with a reduced repetition rate τ/n will result in a two dimensional state because of the addition of the temporal mode. The overall setup then leads to a two-dimensional TNS with one dimension given by the polarization and the other is then given by the temporal delay.

Chapter C

First- and second-order correlation functions

We start here with the introduction of first-order correlation to facilitate the understanding into the second-order. Furthermore, we will briefly show the translation of correlations into a quantum picture.

The first-order correlation function can be calculated by analyzing the intensities within a Mach-Zehnder interferometer [158, 159], shown in Fig. C.1. An incident electric field amplitude $E(t)$ of a light beam is split up at a 50:50 beam splitter (BS) into two light beams with the same intensity ($E_1(t)$ and $E_2(t)$). Both light beams travel different paths z_1 and z_2 and are then interfered at a second 50:50 BS. Afterwards, the intensities of the resulting beams $E_3(t)$ and $E_4(t)$ are detected. We know due to the characteristics of the 50:50 beam spitter that the electric field amplitude in one arm is given as

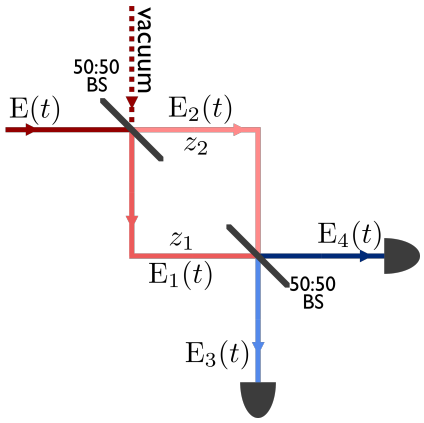

Figure C.1.: Mach-Zehnder interferometer [157]

$$E_4(t) = RTE(t_1) + TRE(t_2) \tag{C.1}$$

with the reflectivity R and transmittivity T for which $T^2 + R^2 = 1$ holds true. The traveling time is given as $t_{1,2} = t - \frac{z_{1,2}}{c}$. Hence, for the time-averaged intensity, it follows

$$\langle I_4(t)\rangle = \frac{1}{2}\varepsilon_0 c|R|^2|T|^2|\tau|^2\left[\langle I_1\rangle + \langle I_2\rangle + 2\mathrm{Re}\langle E^*(t_1)E(t_2)\rangle\right] \tag{C.2}$$

with the time difference $\tau = t_2 - t_1$. The first term $\langle I_1\rangle + \langle I_2\rangle$ is given by the intensities through the internal parts of the interferometer whereas the second term is responsible for the interference fringes. We find that the interference fringes give us the first-order correlation between both arms as

$$\langle E^*(t)E(t+\tau)\rangle = \frac{1}{T}\int_0^T dt E^*(t)E(t+\tau), \tag{C.3}$$

where T is much larger than the characteristic timescale of the field fluctuations. The degree of first-order coherence, i.e. the ability of light to interfere, can be then written as

$$g^{(1)}(\tau) = \frac{\langle E^*(t)E(t+\tau)\rangle}{\langle E^*(t)E(t)\rangle}, \tag{C.4}$$

which is the first-order correlation normalized by the average intensity [42].

The second-order correlation function is derived from the correlation of two intensities whereas for the first order, we are looking at interference of field amplitudes. In 1954 Hanbury Brown and Twiss (HBT) showed a method for measuring the size of an astronomical object by the correlation of photons send from this object measured in two separate telescopes [10], which was the basis for their work in 1956 introducing the degree of the second-order coherence [11]. The basic experiment is the splitting of a optical intensity $I_1(t)$ at a 50:50 beam splitter into two intensities as shown in Fig. C.2. It follows directly $I_3(t) = I_4(t) = \frac{1}{2}I_1(t)$ for the resulting intensities. Similar to the first-order coherence, we can introduce the degree of second-order coherence from the correlation between $I_3(t)$ and $I_4(t+\tau)$ with the time difference τ between the two paths as

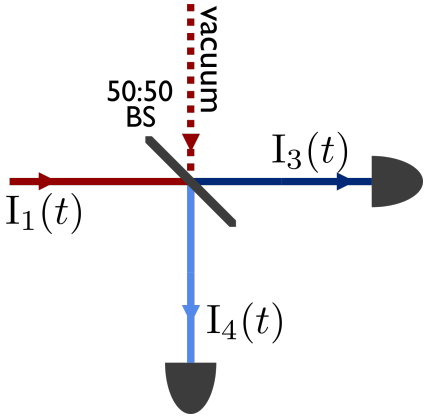

Figure C.2.: HBT experiment [157]

$$g^{(2)}_{3,4}(\tau) = \frac{\langle T_3(t)I_4(t+\tau)\rangle}{\langle I_3(t)\rangle\langle I_4(t)\rangle}. \tag{C.5}$$

We can express this further in terms of field amplitudes

$$g^{(2)}(\tau) = \frac{\langle I(t)I(t+\tau)\rangle}{(\langle I(t)\rangle)^2} = \frac{\langle E^*(t)E^*(t+\tau)E(t+\tau)E(t)\rangle}{(\langle E^*(t)E(t)\rangle)^2}. \tag{C.6}$$

The ordering of the field amplitudes is important here [42].

We use this expression to translate the classical correlation into the second-order quantum correlation function. We replace the electric field amplitudes by the electric field operators $\hat{E}^-(t)$ and $\hat{E}^+(t)$. They describe the positive and negative frequency parts for the electric field operator $\hat{E}(\vec{r},t) = \hat{E}^+(\vec{r},t) + \hat{E}^-(\vec{r},t)$, leading to

$$\hat{E}^+(\vec{r},t) = \sum_{\vec{k}}\sum_{\lambda} \vec{e}_{\vec{k}\lambda}\sqrt{\frac{\hbar\omega_k}{2\varepsilon_0 V}}\hat{a}_{\vec{k}\lambda}\exp(-i(\omega_k - \vec{k}\vec{r}) - \frac{\pi}{2}) \tag{C.7}$$

and $\hat{E}^-(\vec{r},t)$ as its Hermitian conjugated. Using these expressions in the second-order of coherence given in Eq. (C.7), we directly see only a dependence on the creation and annihilation operators,

$$g^{(2)} = \frac{\langle \hat{a}^\dagger\hat{a}^\dagger\hat{a}\hat{a}\rangle}{(\langle \hat{a}^\dagger\hat{a}\rangle)^2}. \tag{C.8}$$

Chapter

D Stimulation

In this appendix, we provide further experimental results for the basic measurement of the stimulated generation of photon pairs in the PDC source via the feedback (see Sec. 4.3). This additional results provide no further information to the already shown ones. However, we want to show them here to further support the given analysis in Sec. 4.3. The data for the pulse energies of $0.329 \cdot 10^{-11}$J and $1.644 \cdot 10^{-11}$J have been already given previously in Sec. 4.3. Here we show the intermediate pulse energies of $0.658 \cdot 10^{-11}$J in Fig. D.1, $0.987 \cdot 10^{-11}$J in Fig. D.2 and 1.315^{-11}J in Fig. D.3. The coincidence rates for the FH measurement (shades of blue) and for the DH measurement (shades of red) are given for the time difference Δt between the first and the next measured click. Like before, we can show the data up to a time difference of $\Delta t = 7\tau$, i.e. the seventh pulse after the initial pulse. We see that the coincidence rates of the FH are higher compared to the DH and that they are decreasing with increasing time difference and the coincidence rates of the DH remain almost constant. The exact results of the coincidence rates and the enhancement factor are given in Table D.1, Table D.2 and Table D.3. We see again the power dependence of the enhancement, which decreases for increasing pulse energies. The enhancement of coincidence rates between the first and

Table D.1.: Coincidence rates for the FH and DH case with the calculated enhancement E at an in-coupling pulse energy of $0.658 \cdot 10^{-11}$J.

Δt	FH [clicks]	DH [clicks]	E [%]
τ	27130 ± 165	12205 ± 110	122.32 ± 1.49
2τ	21140 ± 145	12530 ± 110	68.72 ± 0.96
3τ	17930 ± 135	12505 ± 110	43.36 ± 0.71
4τ	16025 ± 125	12645 ± 110	26.73 ± 0.52
5τ	14700 ± 120	12615 ± 110	16.52 ± 0.39
6τ	13710 ± 115	12575 ± 110	9.01 ± 0.28
7τ	13455.57 ± 116.00	12538.0 ± 111.97	7.32 ± 0.25

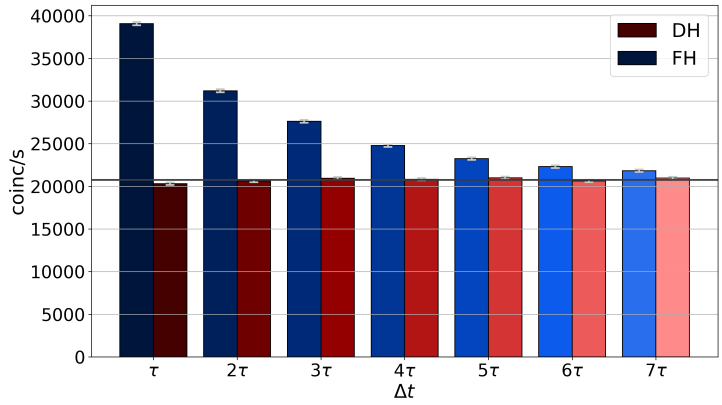

Figure D.1.: Result of the measurement for the enhancement: The coincidence rates for different time differences Δt for the FH (various shades of blue) and the DH (various shades of red) for an in-coupling pulse energy of $0.658 \cdot 10^{-11}$J. The gray line shows the mean of the coincidence rates within the DH at 12516.42 coincidences per second.

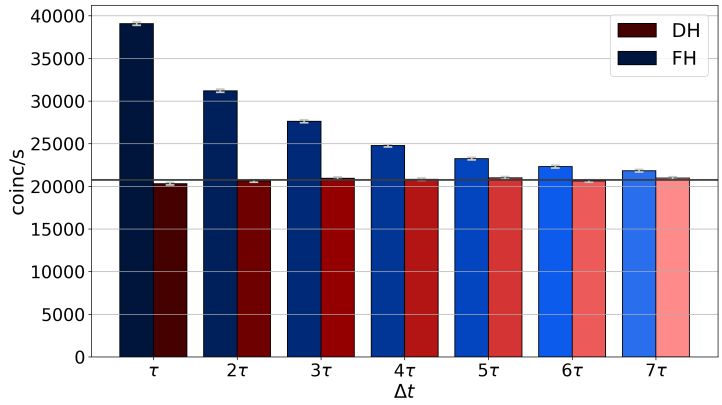

Figure D.2.: Result of the measurement for the enhancement: The coincidence rates for different time differences Δt for the FH (various shades of blue) and the DH (various shades of red) for an in-coupling pulse energy of $0.987 \cdot 10^{-11}$J. The gray line shows the mean of the coincidence rates within the DH at 20759.14 coincidences per second.

the subsequent pump pulse is approximately 122%, 92% and 76% for the different pulse energies. We still see a enhancement of more than 3% of the coincidence clicks after the seventh round trip for all pulse energies. These data underline once again the analyses we have carried out previously.

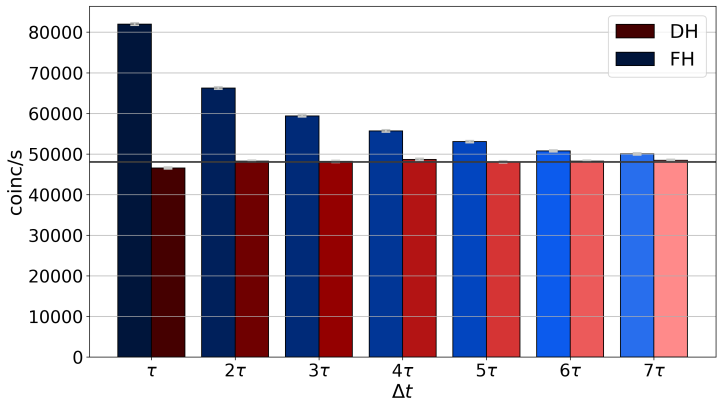

Figure D.3.: Result of the measurement for the enhancement: The coincidence rates for different time differences Δt for the FH (various shades of blue) and the DH (various shades of red) for an in-coupling pulse energy of 1.315^{-11}J. The gray line shows the mean of the coincidence rates within the DH at 48056.28 coincidences per second.

Table D.2.: Coincidence rates for the FH and DH case with the calculated enhancement E at an in-coupling pulse energy of $0.987 \cdot 10^{-11}$J.

Δt	FH [clicks]	DH [clicks]	E [%]
τ	39065 ± 195	20300 ± 140	92.42 ± 0.94
2τ	31205 ± 175	20635 ± 145	51.23 ± 0.61
3τ	27620 ± 165	20940 ± 145	31.88 ± 0.45
4τ	24780 ± 155	20835 ± 145	18.94 ± 0.33
5τ	23245 ± 150	21000 ± 145	10.70 ± 0.24
6τ	22305 ± 150	20630 ± 145	8.14 ± 0.21
7τ	21835 ± 150	20975 ± 145	4.10 ± 0.14

Table D.3.: Coincidence rates for the FH and DH case with the calculated enhancement E at an in-coupling pulse energy of 1.315^{-11}J.

Δt	FH [clicks]	DH [clicks]	E [%]
τ	81950 ± 285	46541 ± 215	76.14 ± 0.54
2τ	66255 ± 255	48236 ± 220	37.36 ± 0.33
3τ	59385 ± 245	48176 ± 220	23.26 ± 0.24
4τ	55670 ± 235	48674 ± 220	14.38 ± 0.18
5τ	53055 ± 230	48063 ± 220	10.39 ± 0.15
6τ	50755 ± 225	48252 ± 220	5.19 ± 0.11
7τ	50030 ± 225	48452 ± 220	3.25 ± 0.08

Chapter E

Additional data: Fock-state analysis

Table E.1.: Fidelities and success probabilities, including their uncertainties, for $n = 2$ and comparable squeezing parameters $|\zeta|$.

	$\lvert\zeta\rvert$	$\mathcal{F}$ [%]	$\mathcal{P}$ [‰]
FH	0.167	$96.10 \pm (7.48 \times 10^{-4})$	$0.191 \pm (2.60 \times 10^{-4})$
DH	0.173	$99.99 \pm (7.51 \times 10^{-4})$	$0.137 \pm (3.08 \times 10^{-4})$
FH	0.233	$95.88 \pm (6.09 \times 10^{-4})$	$0.706 \pm (4.02 \times 10^{-4})$
DH	0.254	$99.99 \pm (7.73 \times 10^{-4})$	$0.637 \pm (6.76 \times 10^{-4})$
FH	0.304	$95.17 \pm (7.89 \times 10^{-4})$	$1.999 \pm (8.59 \times 10^{-4})$
DH	0.298	$99.98 \pm (7.84 \times 10^{-4})$	$1.203 \pm (9.41 \times 10^{-4})$

Table E.2.: Fidelities and success probabilities, including their uncertainties, for $n = 3$ and comparable squeezing parameters $|\zeta|$.

	$\lvert\zeta\rvert$	$\mathcal{F}$ [%]	$\mathcal{P}$ [‰]
FH	0.196	$87.70 \pm (9.79 \times 10^{-4})$	$0.0177 \pm (6.79 \times 10^{-5})$
DH	0.173	$99.95 \pm (6.54 \times 10^{-4})$	$0.0011 \pm (2.81 \times 10^{-5})$
FH	0.244	$86.58 \pm (9.89 \times 10^{-4})$	$0.0443 \pm (1.34 \times 10^{-4})$
DH	0.254	$99.99 \pm (6.61 \times 10^{-4})$	$0.0119 \pm (9.24 \times 10^{-5})$
FH	0.298	$85.59 \pm (10.3 \times 10^{-4})$	$0.1509 \pm (2.59 \times 10^{-4})$
DH	0.298	$99.98 \pm (6.63 \times 10^{-4})$	$0.0316 \pm (1.53 \times 10^{-4})$

Table E.3.: Fidelities and success probabilities, including their uncertainties, for $n = 4$ and comparable squeezing parameters $|\zeta|$.

	$\lvert\zeta\rvert$	$\mathcal{F}$ [%]	$\mathcal{P}$ [‰]
FH	0.167	$74.59 \pm (14.1 \times 10^{-4})$	$(9.14 \pm 0.58) \times 10^{-5}$
DH	0.173	$97.78 \pm (4.89 \times 10^{-4})$	$(6.21 \pm 2.07) \times 10^{-6}$
FH	0.232	$77.03 \pm (13.4 \times 10^{-4})$	$(1.66 \pm 0.02) \times 10^{-3}$
DH	0.254	$99.70 \pm (5.49 \times 10^{-4})$	$(1.11 \pm 0.08) \times 10^{-4}$
FH	0.304	$73.32 \pm (19.8 \times 10^{-4})$	$(7.19 \pm 0.05) \times 10^{-3}$
DH	0.298	$99.95 \pm (5.38 \times 10^{-4})$	$(4.20 \pm 0.17) \times 10^{-4}$